THE UNIVERSITY *of* EDINBURGH

Characterisation of trabecular bone behaviour under impact

THE UNIVERSITY
of EDINBURGH

Adib Hamdani Bin Rosli

School of Engineering

The University of Edinburgh

This thesis is submitted for the degree of

Doctor of Philosophy

2019

Declaration

I declare that this thesis has been composed by myself and that it has not been submitted, either in whole or in part, in any previous application for a degree. Except where otherwise acknowledged, the work presented is entirely my own.

The instantaneous creep data in Chapter 6 was taken from Edinburgh datashare (Xie, Wallace and Pankaj, 2018) of twenty untreated (without any chemical treatment) bovine trabecular bone cylindrical samples. The analysis of the relevant data to this study was then performed by myself.

Adib Hamdani Bin Rosli

2019

Lay summary

Bone quality deteriorates as people get older; it is usually indicated by the reduction of its load-bearing ability. In an extreme case, elderly people may experience hip fracture when they accidentally fall down. The reasons for this phenomenon are twofold: low quality of the bone and different bone behaviour when it is subjected to faster loading, such as that due to falls. This study investigates the behaviour of spongy bone, which plays an important role in energy absorption due to impact. This behaviour is related to one of the determinants of bone quality, namely the bone volume fraction, BV/TV, which is an indicator of the porosity of the bone.

The above mentioned main objective is achieved by: mathematically formulating the response of bone in the form of uniform bar subjected to a rigid impactor; simulating it using a computational approach (finite element analysis); and conducting the experimental tests to obtain relationships between the response and bone characteristics under impact. The theoretical work involves the development of a mathematical code. A number of parameters in the code govern the load measured at the end struck of the bone specimen. The output variables of the response are investigated against these parameters to establish their relations. In the experimental work, similar load-time pulse is obtained and the output variables are related to the BV/TV. The relations obtained by these two methods

are used to derive the empirical mathematical relationships relating the material stiffness of bone (elastic modulus) with the BV/TV.

The study employs FE analysis and shows that the impact loading is performed faster (dynamic) than those reported in the literature, as well as tests conducted by using similar geometry and quality of the specimens. In other words, the empirical relations obtained in this work correspond to dynamic loading and they show stiffer response compared to tests conducted in slower manner in previous studies.

High BV/TV specimens show response which is comparable to the theoretical and finite element (FE) results obtained with elastic models. However, those with growth plates failed along that weak region. Elastic modulus for particular BV/TV is predicted by using FE analysis by capturing key output variables of the experimental pulse.

The low BV/TV bone specimens consistently produce a distinguishable failure pattern: sequence of rising to peak load, followed by drop to a certain value which is retained over particular duration before the loading ends. This pattern has not been previously demonstrated. FE numerical simulation is extended to simulate this failure pattern; it can be replicated by assigning an appropriate negative value to the tangent modulus parameter in the post-elastic material model.

Abstract

Increasing ageing population around the world implies deteriorated bone quality due to diseases such as osteoporosis. Osteoporosis results in reduced bone density and strength and increases the risk of bone fractures due to impact loads such as those caused by a fall. While numerous studies have been undertaken to evaluate the mechanical properties of bone using experimental or computational approaches most of these have focused on static or cyclic loads. Little is known about the behaviour of bone under dynamic loading, such as that caused by a fall. This study focuses on characterising the impact behaviour of spongy bone which is also known as trabecular or cancellous bone using drop tower tests.

A closed-form solution of drop test on an elastic material is developed in detail to serve as a benchmark. Sequential compressive stress wave equations are derived then coded in programming language to obtain desired number of equations, leading to the resulting force history at the end struck. The number of required intervals to obtain the whole pulse depends on the mass ratio; the developed code can be readily expanded to include a wide range of these ratios. A parametric analysis is undertaken to evaluate the influence of parameters such as elastic modulus and drop height. This evaluation defines the key outputs of the force response, namely peak load, pulse width, interval frequency, number of stress intervals and loading rate; hence it establishes the output variable-parameter relationships, e.g. peak load-elastic modulus relation.

The force response from the closed-form solution is used to verify the finite element (FE) models. The Poisson's ratio is found to have insignificant effect on the resulting peak load and pulse width. Stiffer response is indicated by an increase in peak load or a decrease in pulse width for the same impact. Fast Fourier transform (FFT) is applied to the pulses obtained from the closed-form solution and FE analysis; the returned frequency values reveal that the discrepancy observed in FE results can be attributed to its solver rather than the FFT technique. The time-independent elastic FE model is extended to include the time-dependent viscoelastic behaviour; the latter provides a stiffer response. The output variable-parameter relations from FE analysis are verified by similar expressions derived from the closed-form solution.

Drop tests are conducted in the lab on trabecular bone samples with varying bone volume fraction (bone volume to total volume ratio or BV/TV) to investigate the resulting force response. These responses are categorised on the basis of BV/TV of the tested samples. Samples with large BV/TV are shown to behave in an apparently elastic manner. Low BV/TV samples respond inelastically which the study attempts to simulate using plasticity. Behaviour of samples with growth plates shows inelastic behaviour even though they have large BV/TV.

Regression analysis is carried out on the outputs of pulses obtained from higher BV/TV samples to find the output variable-parameter relations, e.g. inverse relation of pulse width-BV/TV. Inverse modelling using FE analysis is also performed to estimate a representable elastic modulus by matching the peak load and pulse width of the resulting force response. The elastic moduli are found to be in the range of 650 to 1400 MPa for samples with BV/TV ranging between 35 to 53%. Elastic modulus is also evaluated using the initial load-response curve for both lower and higher BV/TV samples to establish linear and power-law loading rate versus BV/TV relationships.

The inelastic behaviour of low BV/TV samples consistently shows initial peak, followed by a drop to a finite non-zero value in the post-elastic regime which is maintained for a considerable prolonged time before the load returns to zero. This pattern has not been previously demonstrated. The duration of plasticity is found to be larger for lower BV/TV samples, while shorter drop time is observed exhibiting brittle breakage after the peak load is attained. The study also considers simulation of the post-yield inelastic response using strain-softening plasticity. It is shown that strain-softening is capable of approximately replicating the post-yield impact response pattern by assuming appropriate value of tangent modulus.

Four dynamic elastic modulus expressions as functions of BV/TV are derived by correlating the relationships regressed experimentally with their correspondences from the closed-form solution. The performance of these linear and power law equations are compared to several relations from the literature and the response from tests conducted at an apparent strain rate of 0.01 /sec on similar samples. It is found that the dynamic elastic moduli found in this study are higher than their quasi-static and monotonic loading counterparts; a conclusion showing the effect of strain rate magnitude on the stiffness of the trabecular bone. The study evaluates the strain rate experienced by bone due to impact loading considered in this study to be a maximum of 44.3 /sec at the initial stage with secant value of 30 /sec at the peak strain. Assuming the high BV/TV samples behave fully elastic, the apparent strain due to impact loads can be as high as 3% in compression.

Acknowledgements

My utmost gratitude to Almighty God who unboundly eases my journey and shows the light at the end of every tunnel. All this happens due to His mercy: showing the path by allowing me to meet these wonderful people (particularly) who directly and indirectly helped me throughout my years in this study.

Firstly to my principal supervisor, Prof Pankaj who has been outstanding in guiding me from the very beginning towards the completion of this thesis. His immense knowledge, wisdom, experience and idea are valuable treasures that assisted me for years especially during my turbulent times. To my second supervisor, Dr Teixeira-Dias from whom I learnt impact mechanics and consulted for the LS-DYNA simulation. My third supervisor, Dr Wallace who assisted me in the experimental work and shared his views on the related aspects. My colleagues: 1) Dr Shuqiao Xie who tought me CTAn, MATLAB and Latex, moreover solved some of my issues with these softwares (and many more which I can't even recall them); 2) Sofwan who always exchanged views with me and supported one another; 3) Dr Noel Conlisk who shared his ideas on the improvement of my thesis; and many more.

I would like to thank my sponsors: The Ministry of Education, Malaysia and International Islamic Univesity Malaysia for supporting my study financially. Without them, this research would not be possible.

Finally, to my family, who have been my backbone for the past four years: Shira (my right-hand iron lady), Ahmad and Nukman sharing my sweat and blood, been supportive and makes me smile (and grumpy sometimes) at the end of every long day in the office. My parents who unreservedly love me, support and pray for my success. My siblings, extended family and my fellow Malaysian friends who helped in their own ways. There is no space nor words to express my gratitude to everyone. Thank you.

Contents

List of Tables

List of Figures

Nomenclature

Symbols

A	Cross-sectional area
$A_{\mathbf{n}}$	Integral in s_{n} expression
α	Mass ratio
$\beta_{\mathbf{i}}$	Decay constants in Prony series
$C_{\mathbf{n}}$	Constant of integration of $(n+1)^{\mathrm{th}}$ interval
c	Elastic wave speed
$D_{\mathbf{p}}$	Penetration depth
$D_{\mathbf{ave}}$	Average sample diameter
E	Elastic modulus
$\sqrt{E\rho}$	Material impedance
$E_{\mathbf{d}}$	Dynamic elastic modulus
$E_{\mathbf{eqm}}$	Equilibrium elastic modulus
$E_{\mathbf{i}}$	Relaxation strengths in Prony series
$E_{\mathbf{tan}}$	Tangent modulus in plasticity
$\epsilon_{\mathbf{min}}$	Minimum principal strain
$\epsilon_{\mathbf{vert}}$	Vertical strain
$\dot{\epsilon}_{\mathbf{ave}}$	Average strain rate
$\dot{\epsilon}_{\mathbf{sct}}$	Secant strain rate
$\boldsymbol{F}_{\mathbf{contact}}$	Contact force on slave node in vector form
$F_{\mathbf{drop}}$	Drop force of failed sample response

$\boldsymbol{F}_{\mathbf{f}}$	Friction force in vector form
$F_{\mathbf{max}}$	Peak load of elastic response
$F_{\mathbf{max,pl}}$	Peak force in inelastic region of failed sample response
$\boldsymbol{F}_{\mathbf{N}}$	Normal force in vector form
$F_{\mathbf{p}}$	Peak force of failed sample response
$\dot{F}$	Loading rate
f	Interval frequency
$f_{\mathbf{n}}$	Maximum returned frequency by FFT method
$f_{\mathbf{si}}$	Penalty factor of k_{i}
$f_{\mathbf{theory}}$	Theoretical frequency
$G_{\mathbf{eqm}}$	Equilibrium shear modulus
$G_{\mathbf{i}}$	Isotropic shear relaxation moduli in Prony series
$g(t)$	Relaxation expression in LS-DYNA
h	Drop height
K	Bulk modulus
$K_{\mathbf{eqm}}$	Equilibrium bulk modulus
k	Structural stiffness
$k_{\mathbf{i}}$	Stiffness of master segment or contact stiffness
$L_{\mathbf{ave}}$	Average sample length
l	Length
$l_{\mathbf{c}}$	Characteristic length
M	Ratio of impactor's mass to the impacted area
$m_{\mathbf{impactor}}$	Impactor's mass
$m_{\mathbf{wet}}$	Wet mass of bone sample
N	Number of stress intervals
ρ	Density

$\rho_{\mathbf{app}}$	Apparent density
$\rho_{\mathbf{ash}}$	Ash density
$\rho_{\mathbf{i}}$	Relaxation times in Prony series
r	Radius
r^2	Coefficient of determination
$s_{\mathbf{n}}$	Compressive stress of $(n+1)^{\text{th}}$ interval
$\sigma_{\mathbf{max}}$	Maximum compressive stress
$\sigma_{\mathbf{p}}$	Peak stress of failed sample response
$\sigma_{\mathbf{Y}}$	Yield strength
σ_0	Initial compressive stress
$\sigma(t)$	Total compressive stress at end struck
T	Interval time
t	Real time
$t_{\mathbf{drop}}$	Drop time of failed sample response
$t_{\mathbf{normalised}}$	Normalised time in multiplication of two
$t_{\mathbf{pl}}$	Prolonged inelastic response of failed sample
$t_{\mathbf{pulse}}$	Pulse width or duration of elastic response
Δt	Time step
ν	Poisson's ratio
v_0	Initial velocity

Abbreviations

BFH Bovine femoral head

BGT Bovine greater trochanter

BV/TV Bone volume to total volume ratio

CDM Central difference method

CF Closed-form

CT Computerized tomography

DAQ Data acquisition

DoA Degree of anisotropy

DXA Dual-energy X-ray absorptiometry

dB Decibel

FE Finite element

FFT Fast Fourier transform

GP Growth plate

PBS Phosphate-buffered saline

QCT Quantitative computed tomography

SHPB Split Hopkinson pressure bar

Tb.Th Average trabecular thickness

TI-E Time-independent linear elasticity

VE Viscoelasticity

Chapter 1

Introduction

This Chapter provides the background of current research, starting from describing the anatomy of long bones, discussing the issues associated with ageing bones, e.g. osteoporosis then finally arguing that there is lack of research on fall mechanics that result in bone fractures, particularly hip fractures. In order to fill this gap, the scope of research is defined around the objective of characterising the mechanical properties of bone under impact.

1.1 Anatomy of long bone

The endoskeleton system of vertebrates consists of two main tissues, namely bone and cartilage. The bone is a multi-purpose organ which acts as a load-bearing structure and contributes to the protection of vital inner organs in addition to its structural purposes. Based on similarity of shape, composition and function, the bones can be classified into either long bone (e.g. femur), short bone (e.g. vertebra) and plate-like such as the skull.

Two distinct tissue types of long bone are apparent at macroscopic level, which

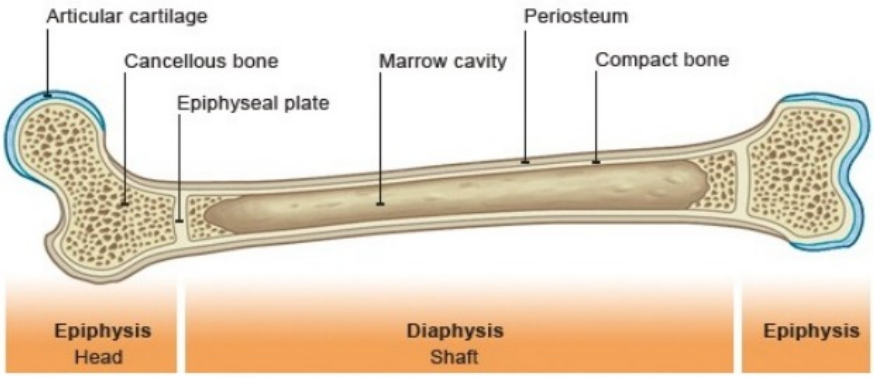

Figure 1.1: Macroscopic structure of femur anatomy. Image from Dean (2010)

are cortical and trabecular bones. The structure of cortical or compact bone encapsulates the whole surface area of long bone. Meanwhile, the spongy inner filling, called cancellous or trabecular bone, is packed at both ends, i.e. proximal and distal epiphyses. The middle shaft or diaphysis is partially hollow filled with soft yellow bone marrow. As an illustration, the anatomy of a human femur is shown in Fig. 1.1. The combination of both bony tissues has inspired the design of composite materials, which provides adequate level of strength while minimising the overall weight of the structure.

1.2 Osteoporosis and hip fracture

Metabolic bone disorders in the elderly are most commonly associated with depletion of bone tissue, e.g. osteoporosis; a phenomenon presenting a major challenge to the healthcare industry. Osteoporotic bone is diagnosed by the reduction in bone density and results in relatively easy fracture occurrence. Regular signs of this disease are increase in porosity and decrease in cross-sectional thickness of the cancellous and cortical bones respectively, while the tissues may be still fully mineralised. Among elderly people, generalised osteoporosis (as opposed to the localised one) is a more common type (Solomon et al., 2010) occurring

throughout the endoskeleton system, which presents even greater challenge to deal with the problem.

World Health Organization (2003) reported that significant number of people (more than 75 million) suffer from osteoporosis in developed countries and recorded 2.3 million osteoporotic fractures anually in Europe and the USA alone. Among these patients, women are three times more prone to the disease; a consequence of mainly post-menopausal effect and lower peak bone mass. Osteoporosis is associated with three common types of fractures, namely the hip, the vertebra and the distal forearm or wrist. Hip fractures are regarded as the most serious judging from the criteria of severe disability of the patients and recorded excess mortality (Sambrook and Cooper, 2006). The impact of hip fractures on medical costs has been estimated by Kanis and Pitt (1992) based on the number of orthopaedic bed allocations in England and Wales, which was one-fifth in 1985 and 1988.

The hip fractures are most commonly caused by fall incidences, although they can be spontaneous (occur without fall due to normal physiological activities) in rare circumstances (World Health Organization, 2003). National Osteoporosis Society (2018) published a consensus statement by the Expert Exercise Steering Group on recommended physical activities and exercises for different categories of osteoporotic patients with specific safety measures. The report is principally intended to promote general health of the osteoporotic patients and answer common questions regarding their well-being.

Based on a surveillance study conducted on elderly patients (mean age = 87 years; $n = 720$) of female-dominant samples of 3:1 ratio who reside in a long-term care facility, Hayes et al. (1993) highlighted the severity of traumatic risk of hip fracture posed by falling from standing height in the case of direct impact on the hip and inadequate protection to absorb the impulsive energy. This type of

finding which directly relates to hip fractures with the osteoporotic community prompts researchers to study various aspects of bone integrity while attempting to make them clinically relevant. One such aspect of this is the bone mechanics related to the behaviour of full bone or extracted samples from either cortical or trabecular regions.

1.3 Motivation of current study

This study is driven by the lack of understanding in the area of impact behaviour of bone. It is found that in spite of the existence of vast literature on the mechanical properties of bone, most tests have been conducted using monotonic or cyclic loading. Such mechanical properties under high strain rate need to be quantified. The key objective of the study is to relate bone properties to measures that can be readily obtained for real patients. In this respect, densitometric measures such as the attenuations from computerised tomography (CT) scans or dual-energy X-ray absorptiometry (DXA) can be utilised.

1.4 Scope of research

The main model of this impact mechanics research was a drop test of rigid hammer on bone sample. This problem was considered using three approaches: a closed-form solution in which the bone was assumed as elastic; finite element (FE) simulation; and lab experiments in which bone samples were subjected to impact.

The variation of the force experienced by the impacted bone was investigated against the parameters related to the impact and bone properties. The bone samples were subjected to X-ray microtomography to evaluate their micro-structural properties before they were tested. Relationships were first developed between a densitometric measure and range of different parameters and then compared with each other.

1.5 Structure of thesis

Chapter 2 reviews the literature which is relevant to this study. It first discusses the mechanical tests conducted on full bones either cadaveric or composite femurs. Then, the experimental tests performed to simulate sideways falls are reviewed, followed by the FE analysis performed in bone mechanics. The review also includes the mechanical properties reported for trabecular bones, which are elasticity-densitometric measures, post-elastic behaviour and time-dependent properties. The reviewed literature is summarised to highlight the main objective in the current study.

Chapter 3 considers development of a closed-form solution to serve as a benchmark for finite element simulations and experimental tests. Sequential compressive stress wave equations are derived, then coded in a symbolic mathematical code to obtain the equations required to express stress variation on impact. These stress equations are used to obtain force at end struck. A parametric analysis is undertaken to establish the influence of loading and impacted object parameters on the response. Finally, the parameter-output variable relations are summarised.

Chapter 4 discusses the development of finite element (FE) model which is validated using the closed-form solution. Main required FE inputs are discussed, e.g. geometry and impact load application. The FE method is employed to demonstrate the effect of several variables on the output response. The fast Fourier transform's approach to obtain interval stress frequency is discussed. Time-related material behaviours of bone are analysed.

Drop test procedure and results are discussed in **Chapter 5**. The experimental methods are elaborated starting from sample preparation to the obtained pulse response. These responses are categorised on the basis of porosity, which is determined by micro-CT scanning prior to testing. The outputs of pulses obtained

that are perceived to be elastic are fitted to find the output variable-parameter relations. Inverse modelling by FE method is also performed to estimate a representative elastic modulus. Nonlinear post-elastic response is presented and the output parameters are investigated. Strain softening in FE method is employed to simulate this pattern. Initial loading rate from most of tested samples is evaluated to obtain mathematical relations between properties. Dynamic elastic moduli expressions are derived by combining the fitted data from experimental results and closed-form solutions.

In **Chapter 6**, the strain rates of the impact system are estimated by FE technique serving as an indicator of the dynamic behaviour. The dynamic moduli are analysed against selected few mathematical expressions from the literature as well as a derived equation from the initial stage of cyclic tests considered as monotonic compression with similar procedures on samples preparation and their micro-structure evaluation.

Chapter 7 revisits important methods in each of the results chapters (Chapter 3-6) and summarises their main findings.

Chapter 2

Review of literature

2.1 Background

Bone experiences time-varying forces throughout its lifetime. It may be subjected to impact forces due to incidents such as falls and vehicle accidents. As discussed in the last Chapter, increasing ageing population implies that even simple falls can result in bone fractures. In fact, falls can cause serious injury in the form of hip fracture even to younger adults (age 15 to 49 years) as concluded by Kannus et al. (2006) in their survey on the patient records at two hospitals in Finland. Its severity emphasises the importance of studies on mechanical loading on the hip.

The mechanical tests in the lab have been conducted on either cadaveric femurs with known health condition prior to death or on composite-synthetic femurs. Often specific regions of the femur are selected for tests: proximal part (mostly selected due to it being directly related to hip fractures); distal (commonly for loading on knee, e.g. Completo et al. (2007)); or the whole femur.

2.1.1 Tests on cadaveric femurs

Cadaveric femurs have been subjected to extensive mechanical tests. Typical static load test on the proximal femur by Keyak et al. (1998) is shown in Fig. 2.1; it simulates stance-like loading on femoral head. In *in vivo* conditions, the load is applied to the femur via the contact between the femoral head and acetabulum in the pelvis. Similar tests have been conducted in several studies (Cody et al., 1999; Schileo et al., 2007). The aim of these tests has been to investigate the stress-strain environment in the femur, fracture loads and pattern due to varying subject-specific shapes and properties. Studies have shown that properties evaluated from CT scans (to be discussed) can be successfully used in computer models to predict mechanical behaviour (Taddei et al., 2006; Schileo et al., 2007; Grassi et al., 2012).

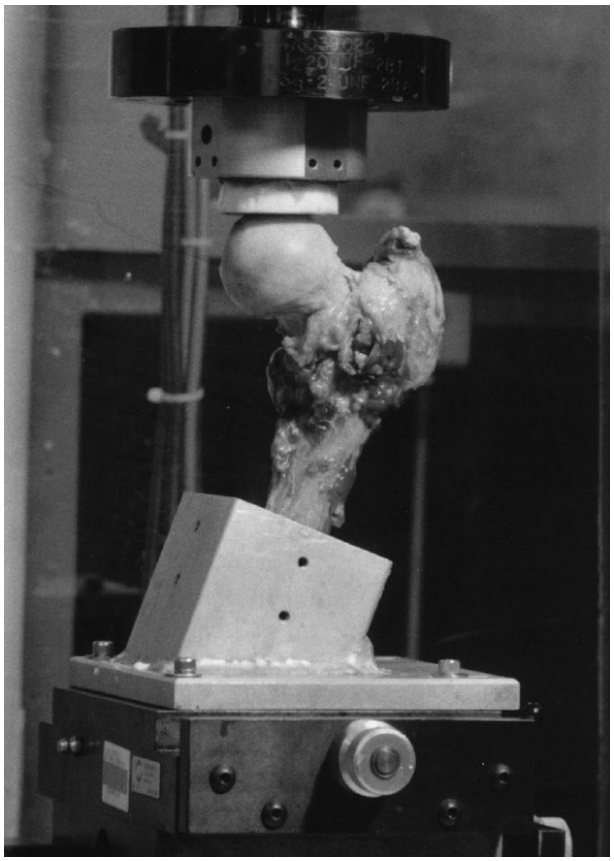

Figure 2.1: Static load on proximal femur (Keyak et al., 1998) simulating stance

2.1.2 Composite femur

Synthetic or composite femurs have been developed to provide a standard for comparison of the mechanical behaviour due to different loading scenarios and due to different implants. While they attempt to have properties similar to human bone, only some basic properties were found to be considered representative, e.g. bending stiffness (Cristofolini et al., 1996; Heiner and Brown, 2001) and axial stiffness (Heiner and Brown, 2001). These series of tests suggest that the latest versions of synthetic bones were developed into having more similar properties to the human bones (Heiner, 2008).

2.2 Experimental tests simulating a fall on the femur

Most tests conducted on the femur consider: a single static activity such as a single-legged stance (Cody et al., 1999); an instance from a cyclic activity such as maximum loading instant during walking (Taddei et al., 2006; Schileo et al., 2007); or cyclic loading e.g. walking (Heller, Bergmann, Deuretzbacher, Dürselen, Pohl, Claes, Haas and Duda, 2001; Heller, Bergmann, Deuretzbacher, Claes, Haas and Duda, 2001). *In vivo* experiments to evaluate the mechanical environment are very difficult experiments, thus the evaluation on bone structural integrity are commonly carried out *in vitro* on mechanical testing machines. It may be noted that there has been pioneering work to evaluate forces experienced by human joints *in vivo* (Rydell, 1966) which has provided input to lab experiments and numerical simulations. One of the main concerns while performing lab experiments is the level of resemblance it provides to the natural loading, so that the experimental results can answer the bone biomechanics problem whose solution is being sought.

The current review of mechanical loading is confined to the simulation of a sideways fall, which represents dynamic loading on the proximal femur. There are two common ways in simulating fall, namely the quasi-static method and a drop-tower impact test. Some researchers have applied a static force with a magnitude claimed to be derived from a fall onto greater trochanter, e.g. Mayhew et al. (2005) while others have applied opposing forces under displacement control to the femoral head and greater trochanter at different relative angles, e.g. Keyak et al. (1998). Some studies have considered quasi-static displacement control to simulate fall, however the rate appears to be too slow such as the cross-head speed of 0.5 mm/min (Bessho et al., 2007) and the strain rate of 0.005 /sec (Grassi et al., 2012).

2.2.1 Quasi-static tests

Quasi-static tests are typically conducted by including a speed aspect to the loading machine in the form of its rate of displacement or load control. Quasi-static loading is suitable in the understanding of normal physiological activities and to replicate spontaneous fractures, i.e. fractures caused by non-traumatic loading. For example, Cristofolini et al. (2007) found the risk of neck failure is the highest during one-leg stance configuration, in which the vertical load is directed at 8° from the diaphysis.

Various loading configurations designed to simulate sideways fall have been employed for various reasons. For instance to find out the sequential process of fracture initiation and progression as in de Bakker et al. (2009). In this experimental study, cadaveric femurs were fractured by simulating a fall under constant displacement of 100 mm/sec to the greater trochanters, where the images of fractures on the surface were sequentially captured by using two high-speed cameras. The experiment revealed that hip fracture due to sideways fall involved a two-stage process, where the failure initiated in superior femoral

neck in which the primary stresses were compressive, followed by failure in inferior neck where the primary stresses were tensile. Based on the results, the failure mechanism was suggested to be associated with large compressive stress in superior region, resulting in either material failure due to yielding resulting in shear failure or structural failure due to local buckling, a well-known failure mechanism for thin-walled structures subjected to high compressive stress. This conclusion on fracture initiation and consequent femoral failures are supported by the subsequent findings of Fliri et al. (2013) in their more accurate experimental drop tests.

Destructive quasi-static tests were performed to validate FE models by Nishiyama et al. (2013) who applied constant displacement control of 2 mm/sec on the greater trochanter. The femur's stiffness was determined from the linear slope of resulting force-displacement curve and failure load from the maximum load experienced by the fractured femur.

Instead of separate investigation on cortical and trabecular part's mechanical behaviour, the study can focus on integrating both bone constituents as a single entity, though analysis is conducted separately for each constituent. For instance, Nishiyama et al. (2013) performed sensitivity analysis of different boundary conditions and determined the individual contribution of cortical and trabecular bones on the overall bone stiffness.

In an attempt to simulate sideways fall via experimental setup, Zani et al. (2015) performed non-destructive and destructive quasi-static load-control tests on cadaveric femurs simulating sideways fall on the hip. Three-quarter of the body weight was applied over the loading duration of 200 msec on the femoral head in both protocols. This type of test protocol exhibits clear limitations as will be discussed in Section 2.5.

2.2.2 Drop-tower tests

A more realistic simulator of sideways fall on the femur employs a drop-tower. An example is shown schematically in Fig. 2.2 (Gilchrist et al., 2014) where the body mass was dropped on the greater trochanter. The configuration attempts to replicate the influence of body mass and stiffness of pelvis and soft tissue. This study was driven by the fact that prior research investigating hip fractures due to a fall by using constant displacement rate protocols might not be describing the fall mechanisms well. In their work, as the benchmark, the constant displacement rate tests were taken from literature which were categorised according to the speed of load application, i.e. slow and fast groups of Nishiyama et al. (2013) and de Bakker et al. (2009) respectively. They found that the femur's failure behaviour is affected by inertia-driven fall simulation which has different nature of loading than the benchmark results, highlighting the areas which quasi-static rate protocol failed to replicate. On the other hand, sub-failure mechanical behaviour appeared to be unaffected. The configuration of femur according to this group is upside down in comparison to the setting of Fliri et al. (2013) in which the dropped mass was on the femoral head, which probably uses the concept of equal action-reaction on both regions.

The previous experiment was refined in Ariza et al. (2015) with target speed before impact of 3 m/sec and a high speed video camera was used to measure the displacement of the greater trochanter. The experimental work was performed to validate the specimen-specific femoral FE models on several key aspects, e.g. bone stiffness, energy absorption and failure location. Moderate correlations were observed for stiffness and energy absorption, while no correlation was found for the derived force by the FE analysis at equivalent displacements with the experimental results. Successful prediction of bone failure by FE model was claimed as its locations of high principal strains corresponded well to the locations observed experimentally.

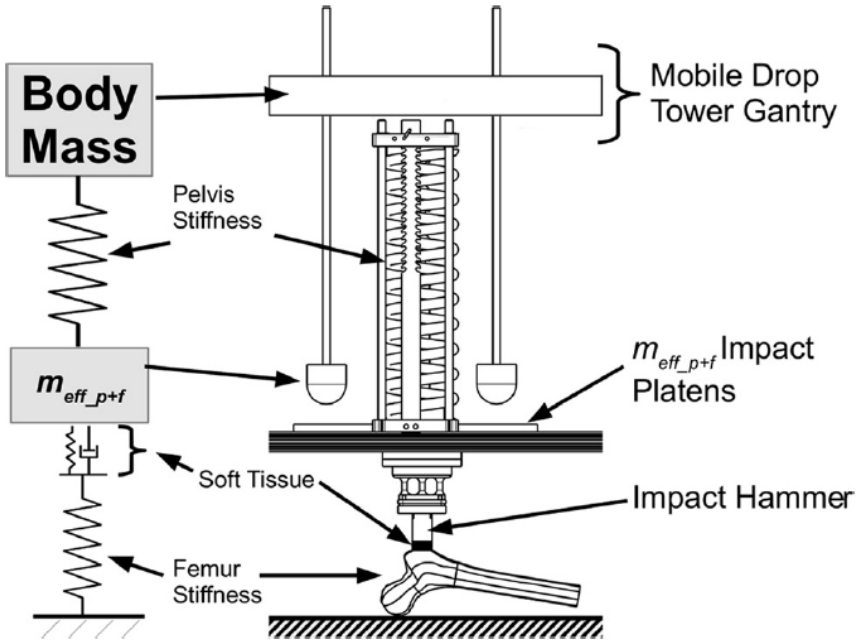

Figure 2.2: Drop-tower fall simulator experiment on femur designed by Gilchrist et al. (2013). Influence of pelvis and soft tissue stiffness is included

2.3 FE models

Microscopic FE models were first developed for trabecular bone (van Rietbergen et al., 1995; Ulrich et al., 1998; Bevill and Keaveny, 2009) and subsequently Donaldson et al. (2011) pioneered their use for cortical bone. These microscopic FE models have been used to relate the micro-structure to apparent level anisotropic stiffness components. This microscopic FE model of trabecular bone has also been used to predict the bone strength (Bevill and Keaveny, 2009). Recent studies utilised high performance computing facilities at Edinburgh to investigate the post-elastic behaviour of trabecular bone and showed that bone's yield criterion can be fairly accurately represented using an isotropic strain-based criterion (Levrero-Florencio et al., 2016); yield behaviour of trabecular bone is not affected by the yield criterion chosen for its solid phase (Levrero-Florencio

et al., 2017*b*); inclusion of damage with plasticity introduces additional anisotropy (Levrero-Florencio et al., 2017*a*; Levrero-Florencio and Pankaj, 2018).

Traditionally, FE models have been used to model whole bones (Huiskes et al., 1985) and to evaluate the behaviour of bone-implant systems (Donaldson et al., 2012*a*; MacLeod et al., 2012; Donaldson et al., 2012*b*; Conlisk et al., 2012). The development of FE model of the femur has been undertaken for various purposes related to the work being undertaken in these studies:

- To predict general outputs observed in the mechanical tests, e.g. strains in sideways fall (Schileo et al., 2007; Bessho et al., 2007; Schileo et al., 2008; Grassi et al., 2012). To predict femoral strength, Falcinelli et al. (2014) developed a FE model of the femur from dual-energy X-rays absorptiometry (DXA) imaging technique and simulated different sideways fall directions that span various accidental conditions. They showed that the mean strength can be as high as 2.995 kN (approximately 4 times body weight) in the unrotated femur configuration. The FE femur model developed using Quantitative Computed Tomography (QCT) method was found to be more accurate in predicting the fracture load than the non-invasive measurement methods viz. QCT and DXA (Cody et al., 1999). On the other hand, the FE femur model developed using DXA technique was found to be a better predictor of femoral strength compared to Quantitative Computed Tomography (QCT) in the case of femur loaded simulating fall onto the greater trochanter (Dall'Ara et al., 2016). Qasim et al. (2016) found that the variations in modelling protocol affect the accuracy of FE predictors based on the values of FE-strength obtained by simulation of fall loading conditions. The percentage errors in prediction of fracture load by FE models are between 10-20% in studies such as those by Koivumäki et al. (2012), where the accuracy depends on the details of modelling methods (van den Munckhof and Zadpoor, 2014).

- To evaluate the issue of uniform versus inhomogeneous material properties assignment to the bone in the femur in the accuracy of the results (Taddei et al., 2006). The study attempted to answer how much two-material model will compromise the accuracy of predicted results compared to density-based inhomogeneous models.
- To validate simulation results by performing non-bias (blinded) FE validation with two different institutions conducting similar tests either experimentally or computationally (Trabelsi et al., 2011).

2.4 Mechanical properties of trabecular bone

Trabecular bone under monotonic loading has a typical response as shown in Fig. 2.3; divided into elastic and plastic regions. Commonly, 0.2% strain offset method is used to determine the yield point separating the two regions and marking the corresponding yield stress and strain (Turner and Burr, 2001). The variation of elastic properties with density has also been extensively discussed (Helgason et al., 2008) -this will be further considered in this Chapter.

Nonlinearity in the stress-strain curve has been extensively reported in both tensile and compression tests (Kopperdahl and Keaveny, 1998; Charlebois, 2008). The two corresponding curves in Fig. 2.4a show initial linear response followed by the reducing gradients in a nonlinear manner. Nonlinear pattern of trabecular bone subjected to high compressive strain is shown in Fig. 2.4b which is akin to a response of elastoplastic cellular solid (Gibson and Ashby, 1997; Charlebois, 2008). The graph shows softening of bone after ultimate stress was achieved, then it rehardened; this sequence causes an observable minimum stress level (Charlebois, 2008).

Cyclic tests have been conducted on bone to evaluate its fatigue behaviour. This behaviour of trabecular bone was characterised by decreasing secant modulus and

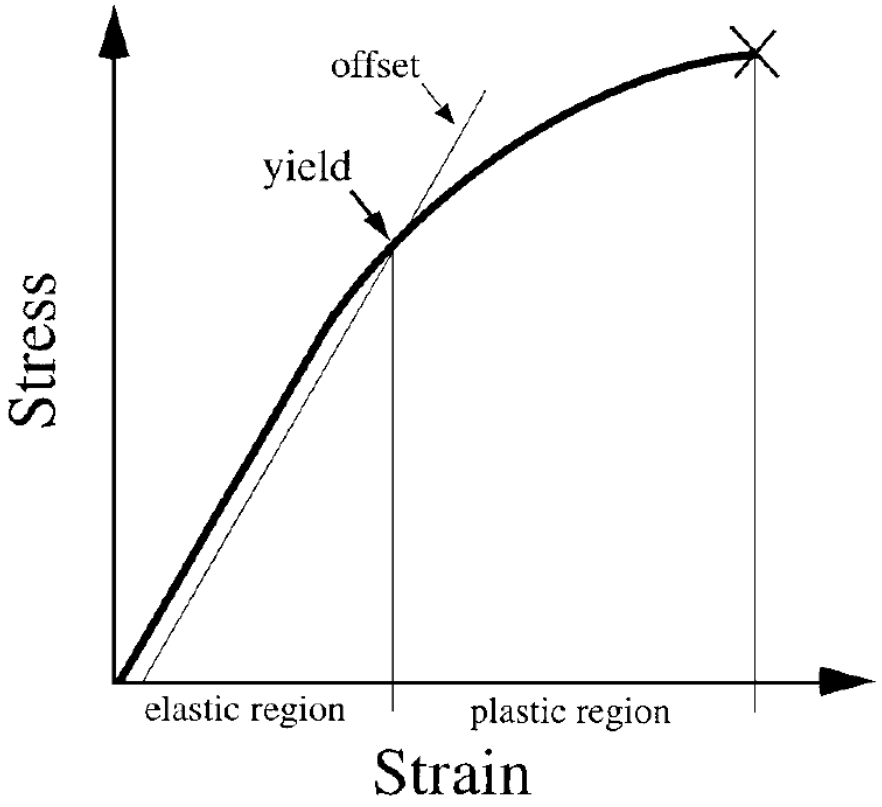

Figure 2.3: Typical response of trabecular bone under uniaxial monotonic tests. Elastic and plastic regions divided by yield point (Turner and Burr, 2001). This point is commonly estimated by using 0.2% strain offset method; marking the yield stress, yield strain and the slope as elastic modulus

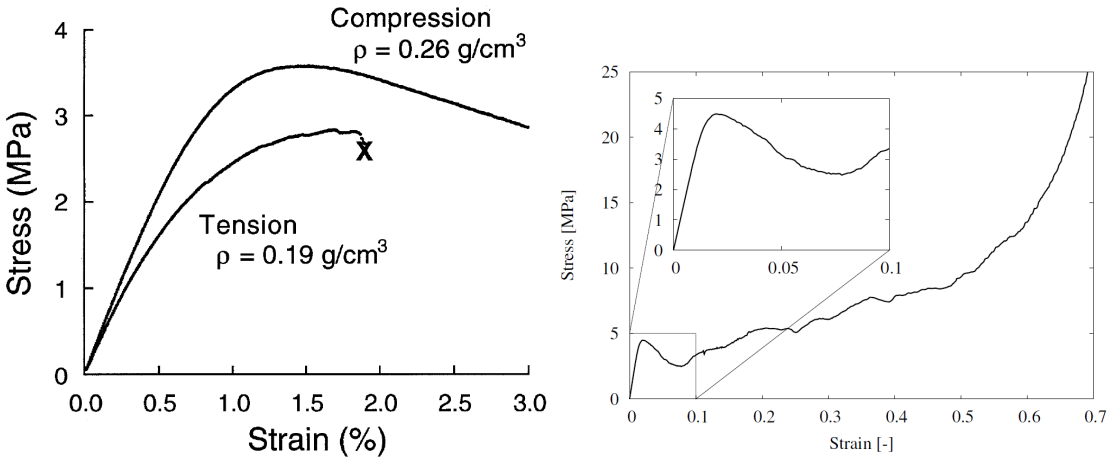

(a) Tension versus compression stress-strain curves of human vertebral samples (Kopperdahl and Keaveny, 1998)

(b) Typical bone response due to large compressive strain by Charlebois (2008)

Figure 2.4: Nonlinearity in monotonic test

increasing nonlinearity as well as hysteresis prior to failure (Bowman et al., 1998) as shown in Fig. 2.5. The extent of elastic response in this fatigue test was defined until either one of these criteria was achieved: 1) ten percent reduction in secant modulus against the initial value; or 2) visible sample fracture. To the best of the author's knowledge, fully reversible compression to tension cyclic tests have not been conducted on bone.

The mechanical tests conducted on trabecular bone samples depend on the type of required outputs desired from the test. Destructive tests are performed if elastic and post-elastic behaviour are required, e.g. (Linde et al., 1991; Shim et al., 2005). For evaluating elastic properties, the non-destructive tests may be adequate but it is now recognised that even small loads may result in irrecoverable strains (Xie et al., 2017). Most previous studies have focused on the determination of time-independent properties of bone, however, more recent studies have considered time-dependent behaviour (Manda et al., 2016; Xie et al., 2017).

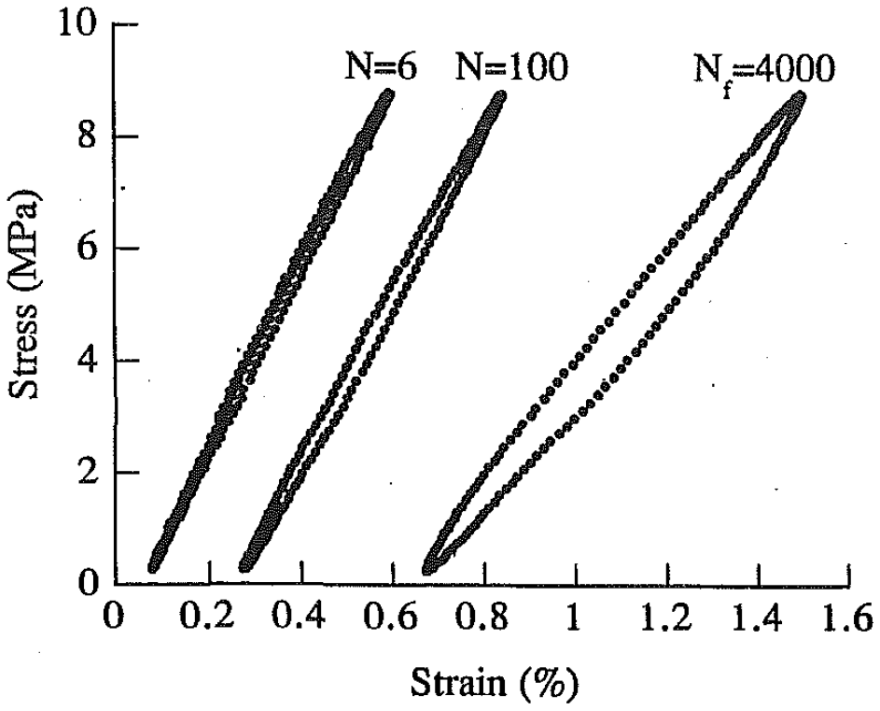

Figure 2.5: Fatigue behaviour of trabecular bone by Bowman et al. (1998). The secant modulus of bone was lowered by increasing number of cycles while the effect on hysteresis was reversed; the bone also became increasingly nonlinear. The elastic data was reported prior to failure (4000 cycles in the study)

This Section discusses relationships which were found for bone mechanical properties via various methods. The elastic modulus and yield strength are the two key properties that past studies have focused on. These properties have been related to bone morphology and in particular, densitometric measurements. The densitometric measures include various types of densities, e.g. apparent and ash as defined in Johanson et al. (1993), as well as the bone volume fraction, BV/TV which is obtained from micro-CT scans. The current review excludes bone properties reported by non-mechanical tests, such as those by Turner et al. (1999) who used acoustic and nanoindentation microscopy techniques to obtain the Young's moduli. In addition, the mechanical tests of particular interest are compressive in nature, since they closely resemble the impact mechanism in the current work.

2.4.1 Elasticity related to density and BV/TV

Various tests have been conducted to obtain the empirical relationships of elastic modulus versus bone density. These tests consider density as the measurement of bone, e.g. apparent (Lotz et al., 1990; Linde et al., 1992; Morgan et al., 2003) and ash (Keller, 1994; Kaneko et al., 2004) densities. Very few chose the densitometric property of BV/TV, e.g. Goulet et al. (1994); Ciarelli et al. (2000); Manda et al. (2016); Xie et al. (2017) most probably due to the need to undertake micro-CT, a facility not readily available for its analysis. The proposed mathematical relationships are substantially diverse as reviewed by Helgason et al. (2008). The resulting range of elastic moduli is shown in Table 2.1 for a few selected expressions available in the literature. It is now well-established that the elastic modulus is related to bone's density or bone volume ratio; it increases as these measures increase. However, it is also recognised that bone's strength and elastic modulus are not fully explained by density measures and bone's microstructure also has an important role to play (Zysset et al., 1998; Parkinson et al., 2012).

Some studies considered multiple anatomic sites such as Morgan et al. (2003). They found elasticity-density power-law relationships varying between the femoral neck and greater trochanter. The former results in stiffer moduli compared to the latter for the considered range of densities; supported by the denser state of the specimens from femoral neck. Meanwhile, most researchers chose a particular anatomic site to harvest the samples, such as Lotz et al. (1990) and Li and Aspden (1997) who tested samples from human femoral neck and head respectively.

Another dependency of elastic modulus was found based on the tested specimen geometry. It was found that the standard error of modulus for cylindrical sample is substantially lower than the cubic specimens (Keaveny et al., 1993); they recommended cylindrical samples with length to diameter ratio of 2:1.

Table 2.1: Elastic moduli range from reported density measurement and empirical relationships from literature. The coefficients of determination, r^2 are included

Reference	Densitometric measure	ρ-range [g/cm^3]	E [MPa]	Range of E [MPa]	r^2
Lotz et al. (1990)	ρ_{app}	0.18-0.95	$E = 1310\rho_{\text{app}}^{1.40}$	118.8-1219.2	0.91
Keller (1994)	ρ_{ash}	0.092-1.221	$E = 10500\rho_{\text{ash}}^{2.29}$	44.5-16587.0	0.85
Goulet et al. (1994)	BV/TV	0.06-0.36	$E = 6310(\text{BV/TV})^{2.10}$	17.1-738.4	0.88
Li and Aspden (1997)	ρ_{app}	0.14-1.40	$E = 573\rho_{\text{app}} - 9.4$	70.8-792.8	0.59
Ciarelli et al. (2000)	BV/TV	0.15-0.40	$E = 7541(\text{BV/TV}) - 637$	494.2-2379.4	0.88
Morgan et al. (2003)	ρ_{app}	0.26-0.75	$E = 6850\rho_{\text{app}}^{1.49}$	920.5-4462.0	0.85
Kaneko et al. (2004)	ρ_{ash}	0.102-0.331	$E = 10880\rho_{\text{ash}}^{1.61}$	275.7-1834.6	0.78

Table 2.2: Selected elastic modulus empirical equations as function of apparent density, ρ_{app} [g/cm^3]; and strain rate, $\dot{\epsilon}$ [1/sec] from literature. Insignificant effect of degree of anisotropy (DoA) is observed

	A	B	C	D
Carter and Hayes (1977)	3790	3.0	0.06	0
Ouyang et al. (1997)	2383	1.88	0.07	0
Enns-Bray et al. (2018)	20290	0.63	-0.05	0.0099
$E = \mathrm{A} \cdot \rho_{\text{app}}^{\mathrm{B}} \cdot \dot{\epsilon}^{\mathrm{C}} \cdot (\mathrm{DoA})^{\mathrm{D}}$ [MPa]				

The strain rate effect has been incorporated into the elastic modulus-apparent density relations in the form of direct power law regression (Carter and Hayes, 1977; Ouyang et al., 1997). This parameter was considered by Enns-Bray et al. (2018) to derive the modulus-strain rate relation which also included the degree of anisotropy (DoA). However, DoA was found to have an insignificant effect on the determination of elastic modulus of the samples as it had an exponent close to zero. It should be noted that the introduction of anisotropic parameter, i.e. DoA should be accompanied by the directional information where it is associated with the elastic modulus, *E*. General nonlinear regression model is presented in Table 2.2 for elastic modulus as function of apparent density and strain rate. The elastic modulus has been shown to increase with strain rate for materials such as concrete of different proportion of mixture (Wang et al., 2012) and porosity (Deng et al., 2016) in which the tests had been conducted at high strain rates of 40-300 /sec and 70-140 /sec respectively by using split Hopkinson pressure bar (SHPB). Similar modulus-strain rate trend has been demonstrated for bone as well (Carter and Hayes, 1977; Ouyang et al., 1997; Hansen et al., 2008). However, Enns-Bray et al. (2018) presented a contradictory inverse relation with no further clarification.

In FE analysis of the whole femur, varying elastic moduli values can be assigned to individual elements according to the density based on the CT scan data, e.g.

in Keyak et al. (1998); Bessho et al. (2007); Nishiyama et al. (2013) to create a heterogeneous femur model. The cadaveric femur is subjected to CT scan to obtain the grey-scale images which can define the density for each region. Thus, modulus-density equation such as those listed in Table 2.1 is chosen according to the judgement of the user.

The inhomogeneous femur FE model is constructed for various reasons. For instance, the material-mapping property assignment for a femur model considered by Schileo et al. (2007), which was used to compare strains from three density-elasticity relationships viz. Carter and Hayes (1977), Keller (1994) and Morgan et al. (2003). The cited study then examined the ability of principal strain failure criterion in identifying bones fracture patterns in subject-specific FE models compared to two stress-based failure criteria, i.e. von Mises and principal stress (Schileo et al., 2008). The verification process was performed by evaluating strain results from their former studies on strain predictor (Schileo et al., 2007) together with two stress-based failure criteria against their experimental procedures simulating spontaneous fracture (Cristofolini et al., 2007). Grassi et al. (2012) then further assessed the compatibility of that subject-specific FE model from CT data to accurately predict strains in sideways loading configurations as accurately as prediction in quasi-axial loading configurations by *in vitro* low magnitude loads.

2.4.2 Strength and post-elastic behaviour

The bone density is also related to its strength, such as in dynamic characterisation by Linde et al. (1991) and Shim et al. (2005). In these two studies, the ultimate strength is established as a function of bone apparent density as well as the strain rate applied. The authors considered strain rate in the range of 0.0001-10 /sec (Linde et al., 1991) and 100-1000 /sec (Shim et al., 2005). In the case of Shim et al. (2005), the strain rate is substantially high because the equipment

used was split Hopkinson pressure bar (SHPB), an apparatus used specifically for dynamic characterising of materials.

The determination of post-elastic behaviour of trabecular bone sometimes involves the FE analysis, for instance Hosseini et al. (2015) enhanced continuum damage-plastic bone model by reducing the influence of FE mesh size under large compression. They also improved and extended the current trabecular bones model by a gradient-enhanced formulation in order to minimise mesh sensitivity during softening and to stabilise damage formulation in the presence of strain softening.

In modelling the plastic behaviour of bone, Schwiedrzik et al. (2015) investigated the accuracy of nonlinear μFE models based on Drucker-Prager yield surface for predicting cancellous bones apparent elasticity as well as its yield strength in uniaxial tension and compression. The yield surface in this study was expected to be able to calculate the value of plastic compressibility of cancellous bone in the future by formulating quadric approximation. However, the Drucker-Prager solid phase yield criterion was found to have negligible difference with another criterion (eccentric-ellipsoid) in predicting the macroscopic yield strain in various loadings, with exception of those tests under dominantly compression (Levrero-Florencio et al., 2017*b*).

2.4.3 Time-dependent properties

The dynamic properties of trabecular bone were characterised by Shim et al. (2005): the time-dependent viscoelastic properties using one Maxwell element in parallel with a nonlinear Newtonian dashpot constructing a nonlinear viscoelasticity model. The one-dimensional model was extended to a 3D model by incorporating 3D strain tensor into 1D strain variable in the non-linear strain rate dependency constitutive model. The cited work on trabecular bone was attempted

to simulate strain rate dependent compression of cortical bone by including the viscous effect (conceptualised as damping) as a function of equivalent strain rate (Bekker et al., 2014).

Time-dependent properties of bovine trabecular bone samples were characterised in Manda et al. (2016) using uniaxial creep tests. The research utilised the creep compliance function, which is easily convertible to the relaxation modulus function, $E(t)$ by using numerical interconversion methods (Park and Schapery, 1999). As a result, three-term Prony series of compliance-relaxation functions were derived describing linear viscoelastic response of the bone specimens subjected to compressive creep load, which are related to their bone volume fraction (BV/TV). The developed constitutive model was extended to incorporate nonlinear viscoelastic (Manda et al., 2017) and nonlinear viscoelastic-viscoplastic (Xie, 2018) -subsequent models are more complex yet had improved accuracy.

In order to explore more on this time-dependent behaviour, Xie et al. (2017) conducted a multiple-load-creep-unload-recovery test (Fig. 2.6) for samples with varying BV/TV. The study reported that for a given trabecular bone sample, the creep compliance first decreases and then at a certain stress threshold increases with increasing stress levels. For samples with higher BV/TV e.g. 43%, the elastic degradation happens at relatively high stress levels, observed in that study when the magnitude exceeds 17 MPa. On the other hand, the elastic degradation for samples with lower BV/TV e.g. 0.19, occurs at lower stress level; both behaviours are shown in Fig. 2.7.

2.5 Summary of previous studies

Most of investigations simulating fall on femur utilise static test which is deemed to be representable of the impact situation in terms of the magnitude, as such a preference is exhibited by Falcinelli et al. (2014). However, the experimental

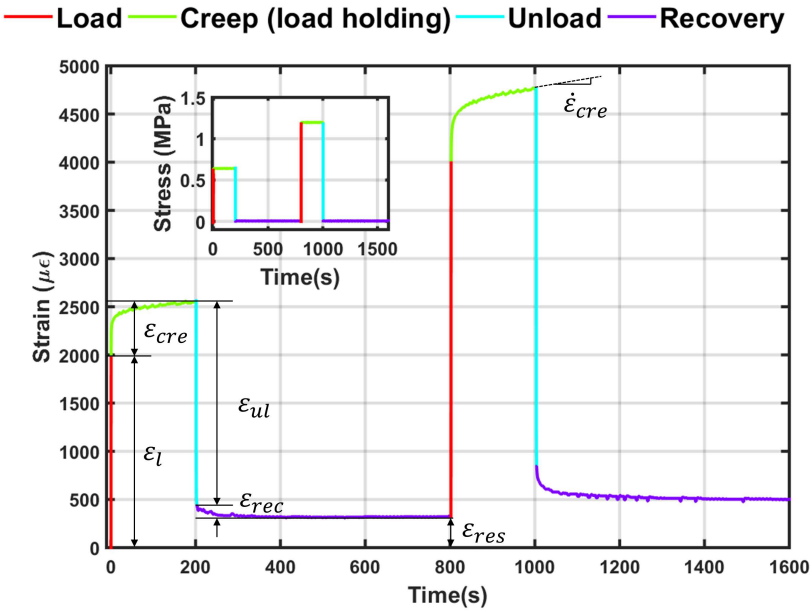

Figure 2.6: Strain response (showing only the first two stages) of trabecular bone tested under multiple load-creep-unload-recovery (MLCUR) experiment by Xie et al. (2017). The inset shows increasing magnitude of two-cycle compressive load application

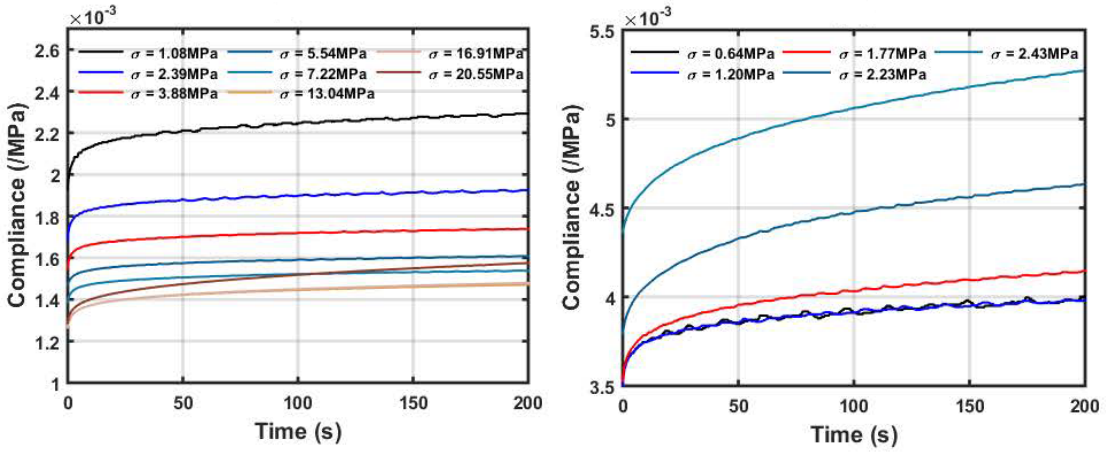

(a) BV/TV=42.8% **(b)** BV/TV=18.6%

Figure 2.7: Creep compliance (Xie et al., 2017)

results of quasi-static test simulating fall in Zani et al. (2015) highlight credible opposition on this method, as its range of actuator speed resulted in the fracture duration of 90 to 170 msec, which is much slower than the duration observed in drop-tower test of around 20 msec as shown by Gilchrist et al. (2014). Another discrepancy noticed in that study is on the loading rate which was set to be a constant, while in reality it varies as a function of nonlinear stiffness which is well-represented in the actual impact test.

Based on their fall simulator in the form of drop-tower test, Gilchrist et al. (2013) admitted the current confined understanding on parameters-body morphology relations, while making drastic change is not an option. The already-complex lower torso model consisted of body mass, soft tissue thickness, pelvis stiffness and effective mass of impact platen is difficult to be broken down into analysis of individual parametric effect on body morphology. This research gap highlights the necessity of dynamically testing bone in their simplest form, i.e. extracted samples, to establish the basic parameter-morphology relationships.

The elasticity-densitometry empirical relations of trabecular bone in Table 2.1 suggests that those tests were dependent on the individual experimental methods and it is impossible to propose an average elasticity-density relationship by statistically pooling the equations together (Helgason et al., 2008). Those tests are also considered as representing static behaviour of cancellous bone as conducted in the quasi-static range, i.e. less than 0.03 /sec. Therefore, the current work attempts to propose a dynamic elastic modulus which is conducted under actual impact tests and supported within theoretical framework to be analysed against a quasi-static relation with comparable methods of analysing the samples derived from Xie et al. (2017) as will be shown in the following Chapters.

Chapter 3

Response of a restrained elastic bar to impact

3.1 Introduction

This Chapter considers the behaviour of an elastic bar, restrained at one end and subjected to an impact force due to a moving rigid impactor at the other end. The treatment in this Chapter is analytical.

This problem was first considered by Timoshenko and Goodier (1951). However, they limited the analytical treatment to mass ratio, α (ratio of the impacted bar to the rigid moving impactor) values between 1 and 1/6. When an elastic bar is struck, it undergoes a compression followed by elastic recovery. For the mass ratios considered by Timoshenko and Goodier (1951), the duration in which this happens is $< 4T$, where T is time taken for the compressive stress wave to travel from the end struck to the restrained support and back. Determination of the contact duration, termed as pulse duration or pulse width (t_{pulse}), depends on the mass ratio; more compressive wave terms are required as the mass ratio decreases

(the striker is assumed to be always heavier than the bar struck). In other words, description of the compressive stress at end struck against normalised time, $2t/T$, where t is the real time, requires large number of intervals to obtain the complete pulse response, i.e. up to the time when total stress at the end struck drops back to zero.

In this Chapter, detailed derivation of a set of compressive stresses, $s_n, n = 0, 1, 2, 3 \ldots$ is considered and includes steps that were skipped by Timoshenko and Goodier (1951). The derived expressions of compressive stress at end struck in this study enables analytical evaluation of compressive impact load experienced by the bar's end struck to be evaluated.

The main objectives of this Chapter are to derive higher-order compressive stress terms. Expressions for up to the fourth term, s_3, are first derived to gain an insight into the analytical formulation. Further higher-order terms, which depend on the mass ratio, are then derived using a symbolic maths code developed in MATLAB (R2016a, 1994-2018 The MathWorks, Inc.). The ultimate output expected from this work is to obtain the analytical compressive load response history at the impacted end of the bar for smaller mass ratios, which are used in subsequent Chapters to verify the numerical finite element (FE) models. The influence of key parameters is examined in this Chapter and their effect on force history output is highlighted. This theoretical study acts as a benchmark closed-form solution for experimental and numerical simulation models of cancellous bone's impact response under investigation.

3.2 Problem definition

Consider a stationary elastic cylinder with radius, r, and length, l, subjected to impact due to a moving rigid impactor at one end (called the end struck), while the other end is fully-restrained as shown in Fig. 3.1a. The impactor has an initial

velocity, v_0, just prior to the first contact at time $t = 0$. Mechanical impedance of a medium is defined as a product of the medium's elastic wave velocity and its mass density. Therefore, based on impedance components of bar's material, i.e. mass density (ρ) and elastic modulus (E); the initial compressive stress at impact time $t = 0$ is given by

$$\sigma_0 = v_0\sqrt{\rho E}, \tag{3.1}$$

where $\sqrt{\rho E}$ is an alternative expression for the bar's impedance. Initial stress σ_0 for a particular material is determined by the impactor's velocity. This initial stress expression will be used repeatedly throughout the stress wave derivation process in the next section while applying the boundary condition between intervals. The first compressive stress wave, s_0, originates from the equation of motion of the body and is only applicable for the first stress wave interval duration,

$$T = 2l/c, \tag{3.2}$$

where l is the bar's length and c is the elastic wave speed. As discussed earlier, this interval, T is the time for the compression wave travelling along the bar with elastic speed, c outwards from the end struck to the fixed end and then returning to the impacted surface. It is worth noting that the speed of stress wave in the continuum is governed by the material's elastic properties, i.e.

$$c = \sqrt{E/\rho}, \tag{3.3}$$

for a simple one-dimensional problem.

Individual compressive wave terms required to evaluate the total stress at the end struck, $\sigma(t)$ are first derived for up to $t = 4T$. Timoshenko and Goodier (1951)

showed that a good estimate for time of contact or pulse duration is

$$t_{\text{pulse}} \approx \frac{\pi l}{c}\sqrt{\frac{1}{\alpha}}, \tag{3.4}$$

which works well for systems with very small mass ratio. Considering normalised time $2\frac{t}{T} = 2, 4, 6, 8, \ldots$ corresponding to the first, second, third, fourth, ... intervals respectively, the required number of intervals, N is estimated by using the normalised time of pulse width, i.e.

$$2N = 2\frac{t_{\text{pulse}}}{T}. \tag{3.5}$$

For example, if the above equation gives $N = 9.2$, then, in view of the doubling of normalised time, the number of intervals required is five to obtain the full response of contact duration, t_{pulse}.

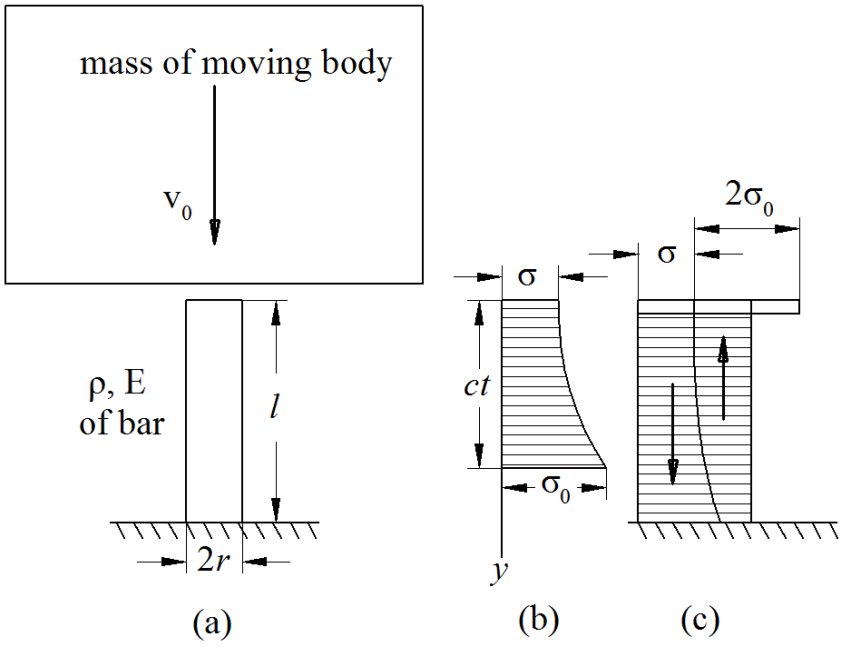

Figure 3.1: (a) The system; (b) stress wave at $t < T/2$; and (c) stresses at $t = T$

Successful derivation of these sequential compressive stress waves, s_n, leads to total compressive stress history, $\sigma(t)$, at the contacted surface of the bar. The total

compressive stress at end struck is calculated as the summation of compressive wave moving towards fixed end at current time, $s_n(t)$ and delayed moving wave at the previous time interval, $s_{n-1}(t-T)$ expressed as

$$\sigma_n(t) = s_n(t) + s_{n-1}(t-T). \tag{3.6}$$

Apart from summing up stress waves at end struck, Eqn. 3.6 also provides boundary condition in the derivation of each stress wave equation, with a slight variation discussed later. The total compressive stress in the history of the end struck is converted to force history by multiplying the stress values with cross-sectional area (A) of the bar, thus establishing direct comparison with FE analysis and experimental measurement of drop test on cancellous bone discussed in the following Chapters.

In the drop test, from a drop height, h, the velocity of the impactor just prior to the impact is given by

$$v_0 = \sqrt{2gh}; \tag{3.7}$$

where g is acceleration due to gravity. This Chapter considers the effect of mass ratio (α), drop height or initial velocity (h or v_0) of the impactor, as well as material properties (elastic modulus, E and mass density, ρ) and geometry (length, l and area, A) of the elastic bar on the resulting outputs, viz. peak load ($F_{\max}$), pulse width (t_{pulse}), interval frequency (f), number of intervals (N) and finally loading rate ($\dot{F}$) specifically by the elastic modulus (Section 3.5.3) in the form of total compressive stress and force histories at the end struck.

3.3 First compressive stress and derivation of subsequent intervals

In this section, a set of first four compressive stress responses, $s_n, n = 0, 1, 2, 3$; are derived for stress wave history traversing to the base (fixed end) then returning back to the end struck for every sequential time interval. These resulting equations are cross-checked with final-form expressions in the referenced original work of Timoshenko and Goodier (1951).

The first compressive stress wave term, s_0, is obtained by using

$$s_0 = \sigma = \sigma_0 e^{-\frac{t\sqrt{E\rho}}{M}}, \tag{3.8}$$

where M is the ratio of impactor's mass, m_{impactor} to the bar's impacted area, A (Timoshenko and Goodier, 1951), given by

$$M = \frac{m_{\text{impactor}}}{A}. \tag{3.9}$$

Replacing

$$\frac{\sqrt{E\rho}}{M} = \frac{2\alpha}{T}, \tag{3.10}$$

the expression for the first stress response becomes

$$s_0 = \sigma_0 e^{-\frac{2\alpha t}{T}}; \qquad 0 \leq t \leq T. \tag{3.11}$$

Note that this expression is only valid for the first time interval, i.e. $t \in [0 : T]$. It is also important to note that the system's mass ratio, α can be expressed as

$$\alpha = \frac{\rho l}{M}, \tag{3.12}$$

representing a dimensionless quantity with the rigid impactor's mass in the

denominator and the mass of the bar in the numerator. The bar's mass in this ratio is presented by its dimensional properties (length, l and cross-sectional area, A) and material property (mass density, ρ).

3.3.1 Compressive stress wave for second interval, s_1

Timoshenko and Goodier (1951) have shown that for the $(n+1)^{\text{th}}$; $n > 0$ interval, the compressive stress, $s_n(t)$, is given by

$$s_n(t) = s_{n-1}(t-T) - \frac{4\alpha}{T} e^{-\frac{2\alpha t}{T}} \left[\int e^{\frac{2\alpha t}{T}} s_{n-1}(t-T)dt + C_n \right], \tag{3.13}$$

where C_n is the constant of integration in the $(n+1)^{\text{th}}$ expression. For $n = 1$, substituting Eqn. 3.11 in Eqn. 3.13, the second stress term is expressed as

$$s_1 = \sigma_0 e^{-\frac{2\alpha(t-T)}{T}} - \frac{4\alpha}{T} e^{-\frac{2\alpha t}{T}} \left[\int e^{\frac{2\alpha t}{T}} \sigma_0 e^{-\frac{2\alpha(t-T)}{T}} dt + C_1 \right]. \tag{3.14}$$

Working on integral terms and simplifying further to distinguish constant of integration, C_1 from the rest of terms in the equation:

$$\begin{aligned}
s_1 &= \sigma_0 e^{-\frac{2\alpha(t-T)}{T}} - \frac{4\alpha}{T} e^{-\frac{2\alpha t}{T}} \left[\int \sigma_0 e^{2\alpha} dt + C_1 \right] \\
&= \sigma_0 e^{-2\alpha(\frac{t}{T}-1)} - \frac{4\alpha}{T} e^{-\frac{2\alpha t}{T}} \left(t\sigma_0 e^{2\alpha} + C_1 \right) \\
&= \sigma_0 e^{-2\alpha(\frac{t}{T}-1)} - \frac{4\alpha}{T} e^{-\frac{2\alpha t}{T}} \sigma_0 t e^{2\alpha} - C_1 \frac{4\alpha}{T} e^{-\frac{2\alpha t}{T}} \\
&= \sigma_0 e^{-2\alpha(\frac{t}{T}-1)} - \frac{4\alpha}{T} t\sigma_0 e^{-2\alpha(\frac{t}{T}-1)} - C_1 \frac{4\alpha}{T} e^{-\frac{2\alpha t}{T}}. \\
\therefore s_1 &= \sigma_0 e^{-2\alpha(\frac{t}{T}-1)} \left(1 - \frac{4\alpha t}{T}\right) - C_1 \frac{4\alpha}{T} e^{-\frac{2\alpha t}{T}}.
\end{aligned} \tag{3.15}$$

Constant C_1 in Eqn. 3.15 is obtained by applying a stress boundary condition at the end of first interval, $t = T$, at which the compressive stress at the end struck,

σ suddenly increases by $2\sigma_0$ as shown in Fig. 3.1c. The condition is expressed as

$$\Big[\sigma_{n-1}(t)\Big]_{t=nT} + 2\sigma_0 = \Big[\sigma_n(t)\Big]_{t=nT}, n = 1, 2, 3, \ldots; \tag{3.16}$$

where $\sigma_{n-1}(t)$ and $\sigma_n(t)$ are total stresses at instantaneous end of previous and start of next intervals respectively.

Hence, Eqn. 3.16 for instantaneous starting time of second interval is written as

$$s_0(T) + 2\sigma_0 = \Big[s_1(t) + s_0(t-T)\Big]_{t=T}. \tag{3.17}$$

Substituting Eqns. 3.11 and 3.15 in 3.17, gives

$$\Big[\sigma_0 e^{-\frac{2\alpha t}{T}}\Big]_{t=T} + 2\sigma_0 = \Big[\sigma_0 e^{-2\alpha(\frac{t}{T}-1)}(1-\frac{4\alpha t}{T}) - C_1\frac{4\alpha}{T}e^{-\frac{2\alpha t}{T}}\Big]_{t=T} + \Big[\sigma_0 e^{-2\alpha(\frac{t}{T}-1)}\Big]_{t=T}. \tag{3.18}$$

Constant C_1 is obtained as

$$\begin{aligned}
\sigma_0 e^{-2\alpha} + 2\sigma_0 &= \sigma_0 + \sigma_0(1-4\alpha) - C_1\frac{4\alpha}{T}e^{-2\alpha};\\
\sigma_0 e^{-2\alpha} &= -4\alpha\sigma_0 - C_1\frac{4\alpha}{T}e^{-2\alpha};\\
C_1\frac{4\alpha}{T}e^{-2\alpha} &= -\sigma_0(e^{-2\alpha} + 4\alpha);\\
\therefore C_1 &= -\frac{\sigma_0 T}{4\alpha}(1 + 4\alpha e^{2\alpha}).
\end{aligned} \tag{3.19}$$

Substituting Eqn. 3.19 in 3.15, then regrouping, the expression for s_1 becomes

$$\begin{aligned}
s_1(t) &= \sigma_0 e^{-2\alpha(\frac{t}{T}-1)} - \frac{4\alpha t}{T}\sigma_0 e^{-2\alpha(\frac{t}{T}-1)} + \sigma_0 e^{-\frac{2\alpha t}{T}} + 4\alpha\sigma_0 e^{-2\alpha(\frac{t}{T}-1)}\\
&= \sigma_0 e^{-\frac{2\alpha t}{T}} + \sigma_0 e^{-2\alpha(\frac{t}{T}-1)}\left(1 + 4\alpha - \frac{4\alpha t}{T}\right),
\end{aligned} \tag{3.20}$$

where the first term of Eqn. 3.20 is s_0, giving

$$s_1(t) = s_0 + \sigma_0 e^{-2\alpha(\frac{t}{T}-1)}\Big[1 + 4\alpha\big(1 - \frac{t}{T}\big)\Big]; \qquad T \leq t \leq 2T. \tag{3.21}$$

The terms inside the square brackets are grouped as such because $4\alpha^n$ term appears in every stress term for subsequent intervals.

3.3.2 Compressive stress for third interval, s_2

Next, similar steps as in previous subsection are repeated to derive the compressive stress wave expression for third interval, s_2. Starting with Eqn. 3.13, previously derived expressions of s_1 and s_0 in Eqns. 3.21 and 3.11 are inserted with substitution of time variable t to $(t - T)$ as follows

$$\begin{aligned} s_2(t) \;=\; & \sigma_0 e^{-2\alpha(\frac{t}{T}-1)} + \sigma_0 e^{-2\alpha(\frac{t}{T}-2)}\Big[1 + 4\alpha(2 - \frac{t}{T})\Big] \\ & -\frac{4\alpha}{T} e^{-\frac{2\alpha t}{T}}\Bigg[\int e^{\frac{2\alpha t}{T}}\Big\{\sigma_0 e^{-2\alpha(\frac{t}{T}-1)} + \sigma_0 e^{-2\alpha(\frac{t}{T}-2)}\Big[1 + 4\alpha\big(2 - \frac{t}{T}\big)\Big]\Big\}dt \\ & + C_2\Bigg]. \end{aligned} \tag{3.22}$$

It is noted the most difficult part in this incomplete s_2 expression (Eqn. 3.22), as well as subsequent higher intervals is the integration procedure. In the previous interval, the number of terms to be integrated were few. However, as the number of terms in higher-order stress intervals grows, so do the number of terms to be integrated. So the latter part of Eqn. 3.22 designated as '$A_n, n = 2$' is evaluated

as

$$\begin{aligned} A_2 &= -\frac{4\alpha}{T}e^{-\frac{2\alpha t}{T}}\left[\int e^{\frac{2\alpha t}{T}}\left\{\sigma_0 e^{-2\alpha(\frac{t}{T}-1)}+\sigma_0 e^{-2\alpha(\frac{t}{T}-2)}\Big[1+4\alpha\big(2-\frac{t}{T}\big)\Big]\right\}dt+C_2\right] \\ &= -\frac{4\alpha}{T}e^{-\frac{2\alpha t}{T}}\left[\int\Big(\sigma_0 e^{2\alpha}+\sigma_0 e^{4\alpha}+8\alpha\sigma_0 e^{4\alpha}-\frac{4\alpha t}{T}\sigma_0 e^{4\alpha}\Big)dt+C_2\right] \\ &= -\frac{4\alpha}{T}e^{-\frac{2\alpha t}{T}}\left(t\sigma_0 e^{2\alpha}+t\sigma_0 e^{4\alpha}+8\alpha t\sigma_0 e^{4\alpha}-\frac{2\alpha t^2}{T}\sigma_0 e^{4\alpha}+C_2\right) \\ &= -\frac{4\alpha}{T}e^{-\frac{2\alpha t}{T}}\left\{t\sigma_0 e^{2\alpha}\Big[1+e^{2\alpha}\Big(1+8\alpha-\frac{2\alpha t}{T}\Big)\Big]+C_2\right\}. \end{aligned} \tag{3.23}$$

Similar to the constant of integration, integral term is also subscripted to ease derivation of the code discussed later. Using Eqn. 3.23, the previous 3.22 can be written as

$$\begin{aligned} s_2(t) &= \sigma_0 e^{-2\alpha(\frac{t}{T}-1)}+\sigma_0 e^{-2\alpha(\frac{t}{T}-2)}\Big[1+4\alpha\Big(2-\frac{t}{T}\Big)\Big] \\ &\quad -\frac{4\alpha t\sigma_0}{T}e^{-2\alpha(\frac{t}{T}-1)}\Big[1+e^{2\alpha}\Big(1+8\alpha-\frac{2\alpha t}{T}\Big)\Big]-C_2\frac{4\alpha}{T}e^{-\frac{2\alpha t}{T}}. \end{aligned} \tag{3.24}$$

In order to find constant C_2, the condition at time between second and third intervals, i.e. $t = 2T$ is applied, where the stress suddenly increases by $2\sigma_0$ at the end struck, similar to the condition applied at the end of the previous interval (Eqn. 3.16), i.e.

$$\big[s_1(t)+s_0(t-T)\big]_{t=2T}+2\sigma_0=\big[s_2(t)+s_1(t-T)\big]_{t=nT}. \tag{3.25}$$

Constant C_2 is then obtained as

$$\begin{aligned} C_2\frac{4\alpha}{T}e^{-4\alpha} &= -\sigma_0\Big(e^{-4\alpha}+4\alpha e^{-2\alpha}+8\alpha+32\alpha^2\Big); \\ C_2 &= -\frac{\sigma_0 T}{4\alpha}\Big[1+4\alpha e^{2\alpha}+\big(8\alpha+32\alpha^2\big)e^{4\alpha}\Big]. \end{aligned} \tag{3.26}$$

This gives

$$\begin{aligned} s_2(t) &= \sigma_0 e^{-\frac{2\alpha t}{T}} + \sigma_0 e^{-2\alpha(\frac{t}{T}-1)}\Big[1+4\alpha\big(1-\frac{t}{T}\big)\Big] \\ &\quad +\sigma_0 e^{-2\alpha(\frac{t}{T}-2)}\Big[1+4\alpha\Big(2-\frac{t}{T}\Big)-\frac{4\alpha t}{T}\Big(1+8\alpha-\frac{2\alpha t}{T}\Big) \\ &\quad +8\alpha+32\alpha^2\Big]. \end{aligned} \tag{3.27}$$

It is noted from Eqns. 3.11 and 3.21, the first two terms of Eqn. 3.27 are in fact s_0 and s_1 respectively. The individual terms in Eqn. 3.27 are again factorised based on exponential terms

$$e^{-2\alpha(\frac{t}{T}-n)}, n = 0, 1, 2.$$

The pattern of compressive stress expression, s_2 has $\alpha^n (n = 0, 1, 2)$ terms in multiplier of $\sigma_0 e^{-2\alpha(\frac{t}{T}-2)}$ (Eqn. 3.27) which are factorised individually, such that

$$\sigma_0 e^{-2\alpha(\frac{t}{T}-2)}\Big[1+4\alpha\Big(2-\frac{t}{T}\Big)+4\alpha\Big(2-\frac{t}{T}\Big)+8\alpha^2\Big(4-\frac{4t}{T}+\frac{t^2}{T^2}\Big)\Big]. \tag{3.28}$$

Therefore, the final expression for the third compressive stress, s_2 is

$$s_2(t) = s_1 + \sigma_0 e^{-2\alpha(\frac{t}{T}-2)}\Big[1+2\cdot 4\alpha\Big(2-\frac{t}{T}\Big)+2\cdot 4\alpha^2\Big(2-\frac{t}{T}\Big)^2\Big]; \quad 2T \le t \le 3T. \tag{3.29}$$

3.3.3 Compressive stress for fourth interval, s_3

Following the now established process, the fourth-interval stress wave expression, s_3, is derived from Eqn. 3.13, in which delayed time variable, $t-T$, is substituted in s_2, s_1 and s_0, as in Eqns. 3.29, 3.21 and 3.11 respectively, hence the full expression compressive stress for fourth interval with unknown constant, C_3 is

written as

$$\begin{aligned} s_3(t) &= \sigma_0 e^{-2\alpha(\frac{t}{T}-1)} + \sigma_0 e^{-2\alpha(\frac{t}{T}-2)}\Big[1+4\alpha\Big(2-\frac{t}{T}\Big)\Big] \\ &\quad +\sigma_0 e^{-2\alpha(\frac{t}{T}-3)}\Big[1+8\alpha\Big(3-\frac{t}{T}\Big)+8\alpha^2\Big(3-\frac{t}{T}\Big)^2\Big] \\ &\quad -\frac{4\alpha}{T}e^{-\frac{2\alpha t}{T}}\Bigg[\int e^{\frac{2\alpha t}{T}}\Big\{\sigma_0 e^{-2\alpha(\frac{t}{T}-1)} + \sigma_0 e^{-2\alpha(\frac{t}{T}-2)}\Big[1+4\alpha\Big(2-\frac{t}{T}\Big)\Big] \\ &\quad +\sigma_0 e^{-2\alpha(\frac{t}{T}-3)}\Big[1+8\alpha\Big(3-\frac{t}{T}\Big)+8\alpha^2\Big(3-\frac{t}{T}\Big)^2\Big]\Big\}dt + C_3\Bigg]. \end{aligned} \tag{3.30}$$

Next, the most laborious work of integrating the integral term, A_3 is expanded into distinguished terms, then integrated individually and regrouped according to exponential terms which gives

$$\begin{aligned} A_3 &= -\frac{4\alpha}{T}e^{-\frac{2\alpha t}{T}}\Bigg[\sigma_0 t e^{2\alpha} + \sigma_0 t e^{4\alpha}\Big(1+8\alpha-2\alpha\frac{t}{T}\Big) \\ &\quad +\sigma_0 t e^{6\alpha}\Big(1+24\alpha+72\alpha^2-\frac{4\alpha t}{T}-\frac{24\alpha^2 t}{T}+\frac{8\alpha^2 t^2}{3T^2}\Big)\Bigg] \\ &\quad -C_3\cdot\frac{4\alpha}{T}e^{-\frac{2\alpha t}{T}}. \end{aligned} \tag{3.31}$$

Integral constant, C_3 is obtained by applying the end struck's boundary condition at the end of third interval, $t = 3T$ into Eqn. 3.16, such that

$$\Big[s_2(t)+s_1(t-T)\Big]_{t=3T} + 2\sigma_0 = \Big[s_3(t)+s_2(t-T)\Big]_{t=3T}. \tag{3.32}$$

Constant C_3 in Eqn. 3.32 is obtained as

$$C_3 = -\frac{\sigma_0 T}{4\alpha}\Big[1+4\alpha e^{2\alpha}+e^{4\alpha}\big(8\alpha+32\alpha^2\big)+e^{6\alpha}\big(12\alpha+144\alpha^2+288\alpha^3\big)\Big]. \tag{3.33}$$

Finally, C_3 is re-inserted into Eqn. 3.31 and solving Eqn. 3.30, and grouping the

expression on the basis of the exponential form,

$$\sigma_0 e^{-2\alpha(\frac{t}{T}-n)}, n = 0, 1, 2, 3;$$

s_3 is expressed as

$$\begin{aligned} s_3(t) &= \sigma_0 e^{-\frac{2\alpha t}{T}} + \sigma_0 e^{-2\alpha(\frac{t}{T}-1)}\Big[1 + 4\alpha\Big(1 - \frac{t}{T}\Big)\Big] \\ &\quad + \sigma_0 e^{-2\alpha(\frac{t}{T}-2)}\Big[1 + 2\cdot 4\alpha\Big(2 - \frac{t}{T}\Big) + 2\cdot 4\alpha^2\Big(2 - \frac{t}{T}\Big)^2\Big] \\ &\quad + \sigma_0 e^{-2\alpha(\frac{t}{T}-3)}\Big\{1 + 4\alpha\Big(9 - 3\frac{t}{T}\Big) + 4\alpha^2\Big[54 - 36\frac{t}{T} + 6\Big(\frac{t}{T}\Big)^2\Big] \\ &\quad + 4\alpha^3\Big[72 - 72\frac{t}{T} + 24\Big(\frac{t}{T}\Big)^2 - \frac{8}{3}\Big(\frac{t}{T}\Big)^3\Big]\Big\}. \end{aligned} \tag{3.34}$$

The first three terms of Eqn. 3.34 express the previous compressive stress wave, s_2, as in Eqns. 3.11, 3.21 and 3.29. Considering the term within curly brackets in Eqn. 3.34, which is

$$1 + 3\cdot 4\alpha\Big(3 - \frac{t}{T}\Big) + 6\cdot 4\alpha^2\Big[9 - 6\frac{t}{T} + 6\Big(\frac{t}{T}\Big)^2\Big] + \frac{8}{3}\cdot 4\alpha^3\Big[27 - 27\frac{t}{T} + 9\Big(\frac{t}{T}\Big)^2 - \Big(\frac{t}{T}\Big)^3\Big].$$

The terms inside $4\alpha^n$ multipliers are simplified as $(3 - \frac{t}{T})^n; n = 0, 1, 2, 3$. Therefore, the compressive stress for fourth interval is expressed as

$$\begin{aligned} s_3(t) &= s_2 + \sigma_0 e^{-2\alpha(\frac{t}{T}-3)}\Big[1 + 3\cdot 4\alpha\Big(3 - \frac{t}{T}\Big) + 6\cdot 4\alpha^2\Big(3 - \frac{t}{T}\Big)^2 \\ &\quad + \frac{8}{3}\cdot 4\alpha^3\Big(3 - \frac{t}{T}\Big)^3\Big]; \qquad 3T \le t \le 4T. \end{aligned} \tag{3.35}$$

The above derivations are up to the fourth stress interval, s_3 as in Eqn. 3.35. Expressions represented by Eqns. 3.11, 3.21, 3.29 and 3.35 show some patterns for $\alpha^n; n = 0, 1, 2, 3$ terms, however, the full pattern is not apparent. As has been discussed earlier, smaller mass ratios require larger number of terms to obtain

the full pulse response. In the following section, an approach to develop code for obtaining higher stress intervals is discussed.

3.4 Generalisation problem process in a programming language

At the end of last section, it becomes apparent the sequential stress wave expressions, s_n become significantly long with increasing number of terms being introduced. Tedious and meticulous work is necessary to derive for higher intervals. Therefore, the manually-driven derivation is shifted to symbolic programming to derive arbitrary number of intervals depending on system under investigation.

All derivation steps are based on the understanding developed in the above discussed formulation procedure. The objective of the derivation code is to obtain and write stress wave equations for arbitrary number of high intervals, which are used primarily in calculating compressive stress response for the entire pulse duration, t_{pulse}.

In this section, two subsequent final stress terms, i.e the fifth and sixth are simply expressed as s_4 and s_5, simplified from the outputs derived by programming code. Then, the general summation form of stress terms is developed with a unique multiplier for each interval.

3.4.1 Development of a symbolic code for arbitrary number of higher-order stress intervals

The main tool used for these derivations was '*symbolic math computation*' in MATLAB, in which variables and functions are defined as symbols without any numerical values. Costly operation of manual derivation is assisted by symbolic

math particularly for two important functions in the code, namely 'integration' for solving consistently expanding integral terms in each subsequent interval and 'simplification' for factorising terms with identical exponential functions in the resulting stress wave equations.

One of the changes made to the symbols employed in the code was that in place of employing $n = 0, 1, 2, 3, \ldots$; the code used $n = 1, 2, 3, 4, \ldots$; i.e. the first stress wave is $s(1)$ instead of s_0. The initial lines in the code involve the process of defining identified variables σ_0, t, T, α as symbolic variables which will be operated on mathematically. Similarly, symbolic dimensioned functions, e.g. s, A_n, C_n are initialised before been operated in any mathematical calculation, in addition of more specific functions such as s_n.

The first stress wave expression, $s(1)$ is manually defined as in Eqn. 3.11 (where it is defined as s_0), while the rest of stress waves are derived from the expression, $s_n(t)$ following Eqn. 3.13. As previous stress expression, $s_{n-1}(t - T)$ is required in Eqn. 3.13, therefore previous stress interval function is defined by means of a 'substitution' function, replacing variable 't' with '$t - T$'. Another term required in the equation is integral term A_n, which is the most expensive operation in which the exponential terms are integrated with respect to time variable, t. In the developed procedure, the integration constant C_n term is excluded initially, but will be soon evaluated.

Next, two different functions for stress boundary condition in Eqn. 3.16 are required, as the derivation for second stress wave, s_1 does not have s_{n-2} term, as opposed to the rest of derived wave equations. In the case of third stress, s_2 onwards, 'substitution' function is used to replace time variable with corresponding interval number $nT, n = 2, 3, 4, \ldots$; whereas the condition of previous interval is kept as zero for s_1.

The process reaches the stage of applying boundary condition, in which time variable is replaced with starting time of the current interval, $t = nT, n = 1, 2, 3, \ldots$ (Eqns. 3.6 and 3.16); in stress terms $s_n(t)$, $s_{n-1}(t)$, $s_{n-1}(t-T)$ and $s_{n-2}(t-T)$. The integration constant, C_n is then solved with all boundary conditions been applied together with the term $2\sigma_0$ as sudden increase in stress reading at the starting time of each interval.

Finally, the final expression for current stress interval, s_n is obtained by including previous stress (s_{n-1}), A_n and C_n in simple algebraic solution and then simplified mainly to group exponential terms together. Although the simplification procedure is optional, it is helpful in reducing the computation cost. Table 3.1 summarises the symbolic functions used to derive higher-interval stress waves through the programming code, in which individual name of function is arbitrary corresponding to represented specific term in manual derivation. The functions in Table 3.1 are grouped into four categories for clarity, i.e. stresses and integration constant.

All sequential processes are repeated in a 'for' loop up to the required number of intervals, *N*, depending upon the system under investigation. The derived stress wave interval formulae are written into simple text editor in every current loop until the final stage in 'string' format. In the following procedure, these formulae are imported back into graph-plotting code to be utilised for calculating compressive stress at the end struck, followed by its corresponding force history.

3.4.2 Code verification with higher order terms

After ensuring that the developed code provided the correct expressions for the first four stress intervals, two more subsequent stress wave intervals ($n = 4, 5$) were expressed in their final simplified form, primarily to verify the general pattern

Table 3.1: Main functions employed in MATLAB code to assist stress derivation

Symbolic in code		Mathematical term	Summary
General	Function (Arbitrary name)		
Stress	s_delT	$s_{n-1}(t-T)$	Defining previous stress interval, e.g. see Eqn. 3.6 and 3.16
	s_delT_cond	$s_{n-1}(t-T)$ $-s_{n-2}(t-T)$	Condition without previous term, e.g. see Eqn. 3.6 and 3.16
	s_exeA	$s_{n-1}(t-T)+A$	Current stress term without C, e.g. see Eqn. 3.13
	s	s_n	Current stress formula obtained by simple algebraic solutions
Integration	A	A_n	Integral term
Boundary condition	s_exeA_nT	$[s_{n-1}+A_n]_{t=nT}$	Applying boundary conditions to stress, s, e.g. see Eqn. 3.16
	s_delT_nT	$[s_{n-1}(t-T)]_{t=nT}$	
	s_nT	$[s_{n-1}(t)]_{t=nT}$	
Integration constant	C	C_n	Calculated with applied boundary condition, e.g. see Eqn. 3.19

of derived compressive wave. These two expressions are not available in the literature.

The expression for the compressive stress for the fifth interval, s_4 is

$$s_4(t) = s_3 + \sigma_0 e^{-2\alpha(\frac{t}{T}-4)}\Big[1 + 4\cdot 4\alpha\Big(4-\frac{t}{T}\Big) + 12\cdot 4\alpha^2\Big(4-\frac{t}{T}\Big)^2 + \frac{32}{3}\cdot 4\alpha^3\Big(4-\frac{t}{T}\Big)^3 + \frac{8}{3}\cdot 4\alpha^4\Big(4-\frac{t}{T}\Big)^4\Big]; \quad 4T \le t \le 5T, \quad (3.36)$$

and the sixth term, s_5 is expressed as

$$s_5(t) = s_4 + \sigma_0 e^{-2\alpha(\frac{t}{T}-5)}\Big[1 + 5\cdot 4\alpha\Big(5-\frac{t}{T}\Big) + 20\cdot 4\alpha^2\Big(5-\frac{t}{T}\Big)^2 + \frac{80}{3}\cdot 4\alpha^3\Big(5-\frac{t}{T}\Big)^3 + \frac{40}{3}\cdot 4\alpha^4\Big(5-\frac{t}{T}\Big)^4 + \frac{32}{5\cdot 3}\cdot 4\alpha^5\Big(5-\frac{t}{T}\Big)^5\Big]; \quad 5T \le t \le 6T. \quad (3.37)$$

A comparison of Eqns. 3.21, 3.29, 3.35, 3.36 and 3.37, i.e. $s_1 - s_5$, a pattern can be observed. A general form of stress wave expression for each interval is given by

$$s_n(t) = s_{n-1} + \sigma_0 e^{-2\alpha(\frac{t}{T}-n)}\Big[\sum_{m=0}^{n} k_m \cdot 4\alpha^m\big(n-\frac{t}{T}\big)^m\Big]; \quad n = 0, 1, 2, 3, \ldots \quad (3.38)$$

An exception to Eqn. 3.38 is for the first compressive stress interval, i.e. s_0 which does not have previous stress interval expression, s_{n-1}. Constant k_m needs to be found for each stress interval; it does not appear to have a discernible form.

3.4.3 Determining compressive stress and load at the end struck

Consider a system with a mass ratio $\alpha = 1/8$. Assume that the values are assigned to the bar's density and its Young's modulus, ρ and E, as well as the initial velocity of the rigid mass, v_0, such that the initial stress is unity, i.e. $\sigma_0 = 1$ as in Eqn. 3.1. For this simple example, compressive stress waves for the five intervals, $s_n, n = 0, 1, 2, 3, 4$; are plotted in Fig. 3.2 alongside their corresponding total stress, $\sigma(t)$ at the end struck. Both curves are plotted against normalised time for better illustration of the number of intervals. In the graph-plotting code, fifty equally-spaced datapoints are employed to obtain values within each interval.

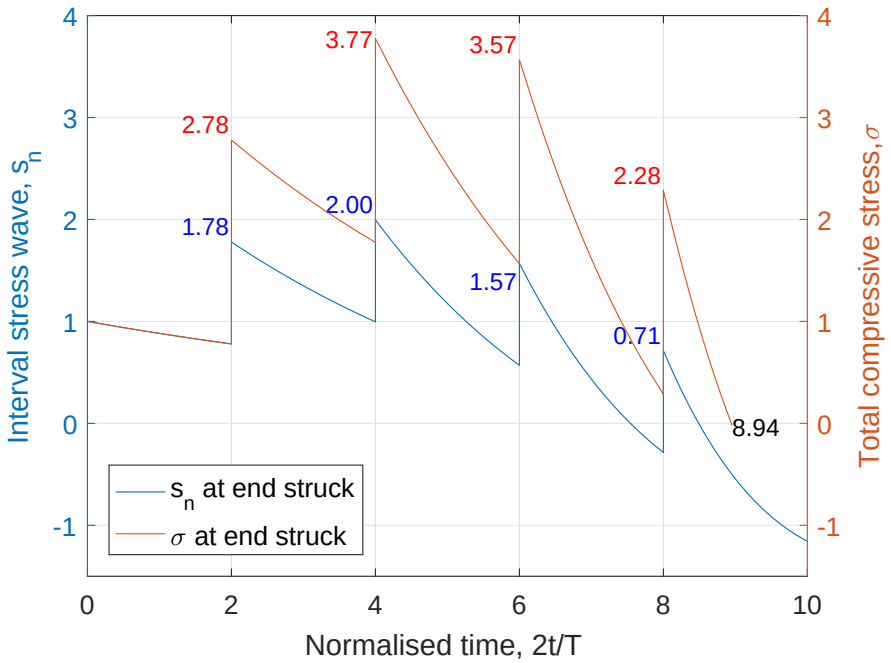

Figure 3.2: Interval and total compressive stress for a system with $\alpha = 1/8$. Stress unit is unnecessary

The total compressive stress, $\sigma(t)$ at end struck is defined as in Eqn. 3.6, in which for any given interval, is the summation of current compressive stress wave, s_n and previous wave, s_{n-1} at delayed interval time, $t - T$. In the first interval, both

σ and s_0 start with σ_0 value then decay following the exponential function in Eqn. 3.11 towards the end of first time interval, $T = 2l/c$. At the starting instant of the next interval, there is a sudden rise as the next compressive wave suddenly increases by double initial stress, i.e. $2\sigma_0$ (Eqn. 3.16). Starting from this second interval, difference between interval stress wave and total stress becomes apparent as the total stress now has effects from both current stress wave as well as delayed wave from the previous time interval.

As the output is plotted against normalised time ($2t/T$), every interval has total normalised value of two. The end of contact is indicated by the corresponding time when total stress at the end struck reaches zero. In this example of one-eighth mass ratio system, the end of normalised time of 8.94 falls between eight-and-ten indicating that the contact ends in the middle of fifth interval. This normalised time can be simply replaced with time, t which is used in most of the following study.

The resulting total stress pulse is unsymmetrical bell shaped curve overall, which becomes almost symmetrical if it is constituted by a significant number of intervals (as will be shown later), i.e. in cases which have small mass ratio values. The peak stress is observed almost in the middle of the graph, which occurs at the starting instants of one of middle intervals. The exponential decay patterns of both graphs have different shape in the initial stress intervals (e.g. in the first two intervals in Fig. 3.2) in comparison to the later intervals (e.g. intervals 3 to 5 in Fig. 3.2) when the peak total compression starts decreasing as the rigid impactor loses its inertial effect and reverses its direction.

Summary of key results in one-eighth mass ratio system are shown in Table 3.2 for the five intervals involved in the whole contact duration. The stress waves, s_n and total stress, $\sigma(t)$ are values calculated at the instantaneous starting time for these two outputs in every stress interval. Examples of force history measured are shown

in the next section on parametric study in which more detailed investigations are considered.

Table 3.2: Compressive stress values at the end struck at the starting time of every interval for the system with $\alpha = 1/8$. Stress unit is unnecessary

Interval	s_n		$\sigma(t)$	
	Symbol	Example	Formula	Example
First	s_0	1.00	s_0	1.00
Second	s_1	1.7788	$s_1 + s_0$	2.7788
Third	s_2	1.9959	$s_2 + s_1$	3.7747
Fourth	s_3	1.5697	$s_3 + s_2$	3.5656
Fifth	s_4	0.71486	$s_4 + s_3$	2.2846

The compressive force at end struck is obtained by multiplying total stress history, $\sigma(t)$ with cross-sectional area, A of the bar. Since the system is pre-defined as one-dimensional, there is no Poisson's ratio effect changing the original cross-sectional dimension of the elastic bar. The final output from this closed-form work is to obtain compressive load history at the end struck as this output is the main output variable under cross-methodology investigations throughout this study.

3.5 Parametric study

First stress wave, s_0 (Eqn. 3.11) provides the parameters governing the impulsive response, namely system's mass ratio (α), rigid impactor's initial velocity (v_0), as well as the bar's material properties (E, ρ) and structural dimensions (included in α and T). This Section investigates how each of these parameters effects the four main response outputs: contact duration or pulse width (t_{pulse}), number of stress intervals (N) within the pulse width, maximum total stress, σ or load (peak load, F_{max}) and interval frequency, f which is associated with T ($f = 1/T$). Some

parameters are considered as 'primary' in this respect such as bar's materials (elasticity and density) as well as dimensions (cross-sectional area and length) and influence the outputs directly, whereas other parameters influence the outputs indirectly (e.g. wave propagation speed, c is influenced by material properties; mass ratio is influenced by mass of rigid impactor as well as bar's density and dimensional properties).

A range of input parameters are considered in this study. This section considers in detail the effect of: system's mass ratio, drop height, bar's stiffness and length. The investigation focuses significantly on the bar's modulus of elasticity, since trabecular bone's elastic modulus (both static and dynamic) presents significant variation with its microstructure as will be shown in Chapter 5. The effects of other parameters, i.e. density, cross-sectional area and impactor's mass are only briefly examined.

3.5.1 Mass ratio, α of the system

As discussed earlier, the mass ratio for this impulsive system is the ratio of bar's mass to moving rigid impactor's mass and is given by Eqn. 3.12. Assuming impactor is always heavier than the bar, this ratio is always less than unity.

Five ratios are considered in this parametric study, which are $\alpha = 1$, 1/2, 1/4, 1/6 and 1/8, requiring only a few stress intervals to plot the complete pulse response. Input parameters, E, ρ and v_0 are given the following values $E = 0.531$ GPa; $\rho = 1.9197$ kg/mm^3; $v_0 = 0.99$ mm/msec; giving $\sigma_0 = v_0\sqrt{E \cdot \rho} = 1$. The reason for this choice is to replicate stress waves and total compressive stress graphs plotted by Timoshenko and Goodier (1951). The first four ratios in Fig. 3.3 reproduce resulting stresses of Timoshenko and Goodier (1951) with highlight on crucial stress values at the starting instants as well as the normalised end time. They act as a tool to double-check the derived stress equations ensuring

all expressions in previous sections were correctly derived and properly coded in MATLAB, henceforth producing validated responses. Meanwhile, the fifth value of $\alpha = 1/8$ is in addition to results plotted in the original work.

Figure 3.3 shows the effect of system's mass ratio on number of intervals, with additional information of the obtained stress values at the starting instant of every interval. The first figure (Fig. 3.3a) is a plot of interval stress waves, s_n for variation of five mass ratio values. Following Timoshenko and Goodier (1951) in which the stresses are plotted against normalised time given by

$$t_{\text{normalised}} = 2\frac{t}{T}. \tag{3.39}$$

The number of intervals is presented in multiplication of two, i.e. 0-2 refers to first interval, 2-4 the second and so forth. Thus, it can be seen from Fig. 3.3b that the required number of intervals ranging between two to five for the range of mass ratio between unity to one-eighth. It is important to note that the pulse end is defined as the instantaneous time when the total stress, $\sigma(t)$ reaches zero. The normalised end times for mass ratios of 1, 1/2, 1/4, 1/6 and 1/8 are 3.072, 4.719, 5.884, 7.410 and 8.936 respectively (Fig. 3.3a).

The values obtained from the developed code are almost identical to those of Timoshenko and Goodier (1951) for $\alpha = 1, 1/2, 1/4, 1/6$. These values show the reliability of the developed code in producing accurate interval stress waves and total compressive stress at the end struck, which consequently resulting in compressive force history at end struck which is the main investigated output.

Figure 3.4 shows the effect of mass ratio on pulse width in real time, in which lower mass ratio results in larger number of intervals and longer pulse duration (the selected parameters result in identical T for all mass ratios). In the code, linear interpolation is employed to determine the end time of impact duration,

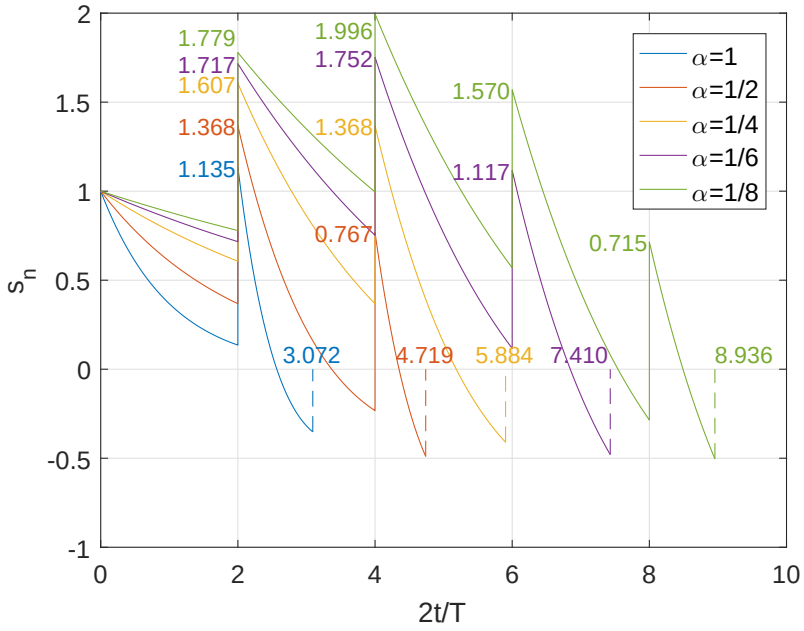

(a) Interval stress wave

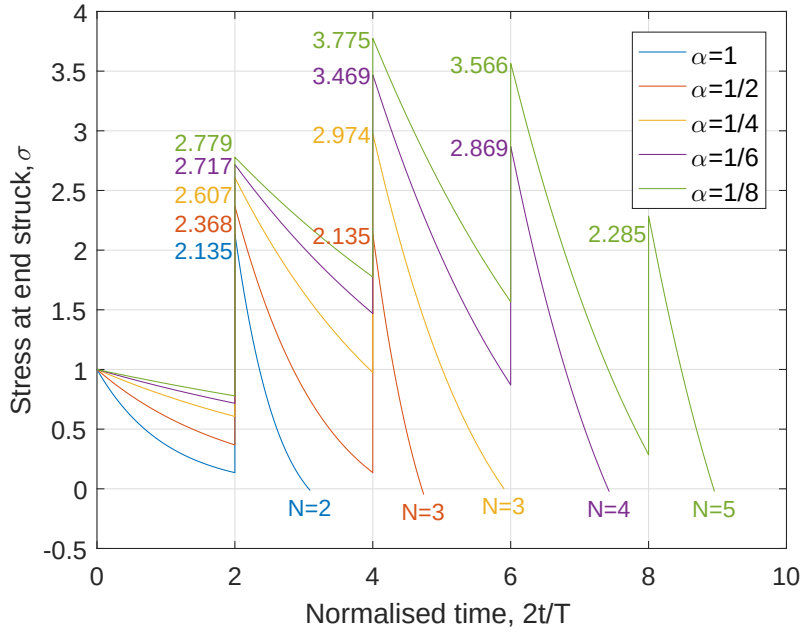

(b) Total compressive stress

Figure 3.3: Effect of mass ratio on stresses and number of intervals. Units are consistent

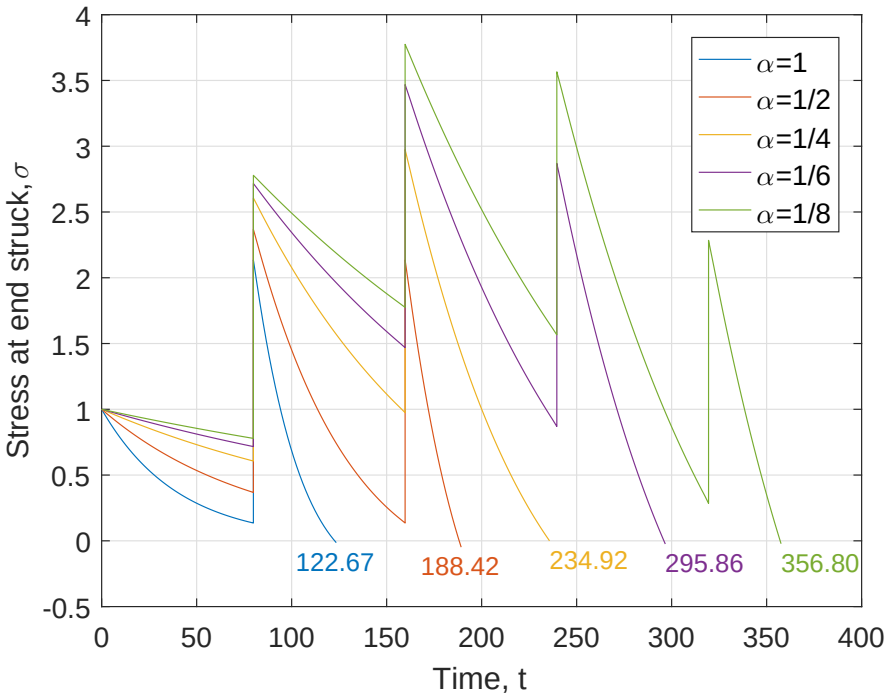

Figure 3.4: Effect of mass ratio on pulse width. Units are consistent

which is the time when total stress or force at the end struck becomes zero, i.e. the impactor starts to lose contact with the compressed end struck of the bar. The accuracy of interpolation depends on number of datapoints defined for every plotted interval, for which fifty is considered to be sufficient.

Timoshenko and Goodier (1951) provided a formula for approximately estimating the pulse width, given in Eqn. 3.4 especially for small mass ratio values. The equation shows that the pulse width depends on the wave propagation speed, c (a function of bar's material properties), length of the bar, l and mass ratio, α of the system. By dividing the estimated pulse duration of Eqn. 3.4 by T, the number of intervals can be estimated as

$$N \approx \frac{\pi}{2}\sqrt{\frac{1}{\alpha}}. \tag{3.40}$$

Table 3.3 compares the number of intervals as in Fig. 3.3a for different mass

Table 3.3: Number of intervals by mass ratio in Fig. 3.3a compared to estimator $N \approx \frac{\pi}{2}\sqrt{\frac{1}{\alpha}}$. Units are consistent

α	$N \approx \frac{\pi}{2}\sqrt{\frac{1}{\alpha}}$ (Eqn. 3.40)	Halved end time in Fig. 3.3a (following Eqn. 3.5)
1	1.57	1.536
1/2	2.22	2.359
1/4	3.14	2.940
1/6	3.85	3.705
1/8	4.44	4.468

ratios to the values estimated by the approximation provided by Eqn. 3.40. It is apparent that there is some difference in the two values primarily because the mass ratios are not sufficiently small. The estimator, however, is a useful tool for predicting the number of required stress intervals.

As a conclusion for mass ratio (α), it affects the number of intervals (N), pulse width (t_{pulse}) and peak load ($F_{\max}$) of the resulting stress at the end struck. As mass ratio decreases, i.e. the impactor becomes increasingly heavier than the bar, more intervals are required to obtain the response for the entire pulse duration. Also smaller mass ratio increases the peak load as heavier mass imparts more energy to the contacted surface, thus resulting in higher stresses at the end struck. On the other hand, this parameter does not alter the interval frequency, f of the resulting pulse as each interval has similar time duration, T regardless of variation in the system's mass ratio.

3.5.2 Drop height, h of the moving impactor

The initial compressive stress, σ_0 has been shown to be a function of initial velocity of moving impactor and bar's impedance (Eqn. 3.1). The initial velocity, v_0 is the axial velocity of the moving rigid impactor at the instant before contact with the struck end surface occurs. The general expression for stress wave in Eqn. 3.38 shows direct proportionality between v_0 and the resulting stress terms, s_n via σ_0 which is ubiquitous in each of the terms in that equation. Meanwhile, σ_0 does not influence the other output variables: pulse width (Eqn. 3.4) and required number of intervals (Eqn. 3.40). Based on the above mentioned equations, the square-root of initial velocity is inferred to proportionally affect the resulting peak load ($F_{\max}$) via the interval stress wave equations, while the rest of output variables are independent of v_0.

The drop height does not affect the number of stress intervals or the time location of the peak stress (since the peak load is directly proportional to initial velocity). It is interesting to note that the time location of peak load cannot be predicted *a priori* though it will occur in one of the middle intervals.

The experimental work undertaken in this thesis (discussed in subsequent chapters) is based on a hammer falling on top of the cylindrical trabecular bone sample, for which v_0 is obtained using Eqn. 3.7. In order to illustrate the previous inference on the effect of drop height (via initial stress), four drop heights; 100, 50, 25 and 10 mm, are considered in this parametric study. Corresponding initial velocities, v_0 and other input parameters are given in Table 3.4. Typical bovine trabecular bone's material properties are assigned to the cylindrical impacted sample, which has a diameter of 10.6 and a length of 12 mm.

The effect of drop height on the resulting pulse is shown in Fig. 3.5 for four variations of models, affecting the peak load ($F_{\max}$), consistently from the starting

Table 3.4: Summary on the effect of drop height parameter; Units: length [mm], mass [g], time [msec], pressure [MPa], load [kN], frequency [kHz]

h [mm]	Inputs				Outputs			
	v_0	m_{impactor}	E	ρ	$F_{\max}$	N	t_{pulse}	f
100	1.40	26.6229	531	1.31×10^{-3}	0.545	7	0.253	26.53
50	0.99				0.385			
25	0.70				0.272			
10	0.44				0.172			

instant, i.e $t = 0$, via initial stress (σ_0) or load response. The difference in load history between the four models is always proportional at any time. Based on this graph and revisiting the governing equations (Eqns. 3.6 and 3.38), the peak load for this system, which comprises of seven stress intervals ($N = 7$), occurs at the starting instant of the fifth interval, such that

$$F_{\max,N=7} = \sigma(4T) \cdot A = \left[s_4(4T) + s_3(3T)\right] \cdot A \tag{3.41}$$

in these particular systems, which give the time-based location of peak load from Fig. 3.5. All relevant equations: including Eqns. 3.1 and 3.7, suggest direct linear proportionality between the peak load and square-root of drop height, e.g. $F_{\max} \propto \sqrt{h}$, as the drop height parameter only appears in the initial stress term, σ_0. As an alternative physical explanation, higher drop height corresponds to faster initial velocity, v_0 which first magnifies the initial stress (σ_0), and subsequently the rest of stress and force values history at the end struck, in particular the peak load as the main output under investigation.

By adopting 'linear fit model' in MATLAB to these data, these particular systems' relationship is established as

$$F_{\max} = 0.05447\sqrt{h} \quad [\text{kN}], \tag{3.42}$$

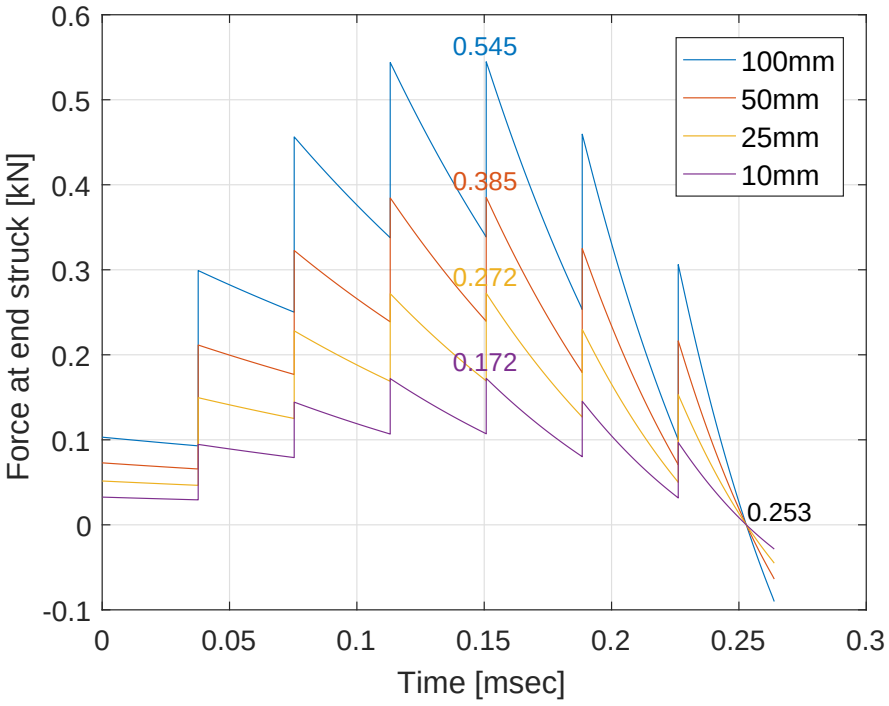

Figure 3.5: Drop height effect on the peak load

which confirms the direct linear correlation between $F_{\max}$ and $\sqrt{h}$ as shown in Fig. 3.6. The peak load-drop height relation in Eqn. 3.42 supports the peak load-hip impact velocity linear regression model ($r^2 = 0.995$) in Majumder et al. (2008) who simulated sideways fall by 3D FE simulations consisted mainly the pelvis, proximal part of femur and soft tissue models.

On the other hand, as both the pulse width and interval time are independent of the drop height predicted by Eqns. 3.4 and 3.2 respectively, Fig. 3.5 confirms that both contact time, t_{pulse} and interval time, T, hence its inverse, namely the frequency, f are unchanged by this parameter variation. More specific data is presented in Table 3.4 on the affected ($F_{\max}$) and unaffected (N, t_{pulse} and f) outputs in this parametric study.

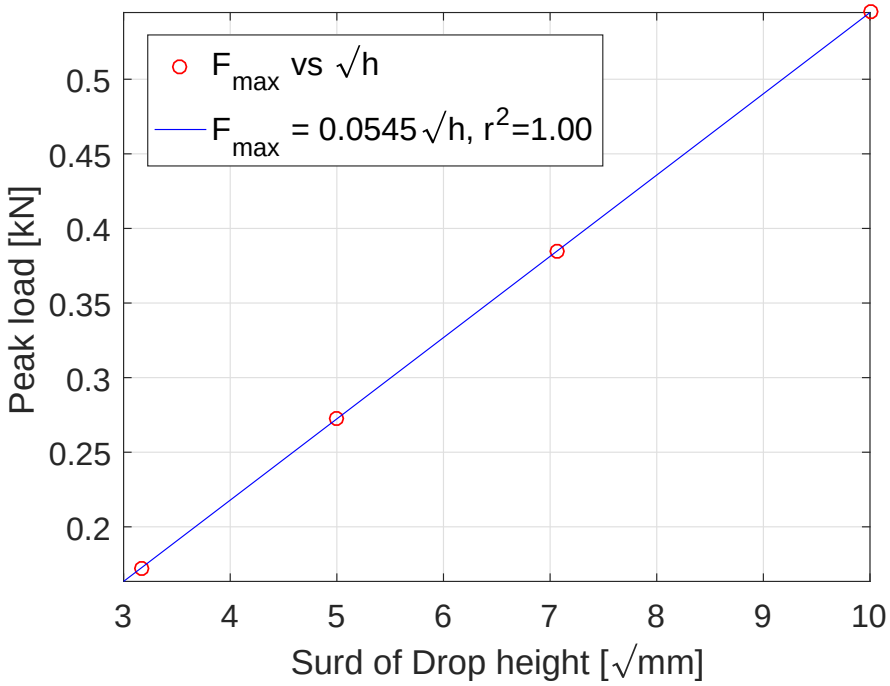

Figure 3.6: Linear regression model relating F_{max} and $\sqrt{h}$

3.5.3 Elastic modulus, E of the bar's material

Bar's modulus of elasticity, E or material stiffness has direct as well as indirect effect on the pulse response of the impacted bar's dynamic behaviour. In the calculation for peak load, the impedance-initial stress relation, $\sigma_0 = v_0\sqrt{E \cdot \rho}$ (Eqn. 3.1) shows direct relation between square-root of elastic modulus as a component of mechanical impedance with the resulting initial stress experienced by the bar's end struck. Additionally, parameter E also influences interval time, T in the exponential and polynomial terms in Eqn. 3.38, which is eradicated if time t is expressed in terms of fraction of T. Higher initial stress due to stiffer response by impacted bar increases the subsequent stresses, s_n and load response histories until the end of contact; this is a similar effect as the one described in the influence of drop height on peak load previously.

On the other hand, time-based outputs are influenced by the wave propagation

speed factor, c which depends on the elastic modulus, E to be considered as having indirect influence on these kind of outputs, similar to the impedance on peak load previously. The elastic wave speed is directly proportional to the square-root of material's elastic modulus as expressed in well-known one-dimensional wave propagation Eqn. 3.3. Two outputs are categorised as time-based, namely pulse width, t_{pulse} and interval time, T or its inverse, the interval frequency, f. As the interval frequency is the primary product when Fourier transformation is performed the emanating force response, f better represents the latter output variable; this will be discussed extensively in the next Chapter (Section 4.6).

In the case of pulse duration, its width is inversely proportional to the wave speed given by Eqn. 3.4, leading to $t_{\text{pulse}} \propto \frac{1}{\sqrt{E}}$. Another time-based output, which is interval frequency has direct proportionality with elastic modulus of the impacted bar, i.e. $f \propto \sqrt{E}$ as expressed in the interval time equation (Eqn. 3.2).

In the experiments of impact on bone sample considered in Chapter 5, a 2.5-kg impactor was used to impact on 21-mm high cylindrical bone samples with a diameter of 10.6 mm, in which the values are average measurements. This system results in a significantly low mass ratio of around 9.71×10^{-4}, requiring significantly large number of intervals, N to evaluate and plot the complete pulse response, which also leads to higher computational cost. Therefore, in this parametric study on the elastic modulus, significantly higher number of intervals, N is predicted for the five models of Table 3.5. The current study is based on actual 50-mm drop tests of 2.5-kg rigid hammer impacting the trabecular bone samples with varying Young's modulus of elasticity, E. Typical material density of cancellous bone is used ($\rho = 1.31 \times 10^{-6}$ kg/mm^3), as tabulated in the 'Input' column. Equation 3.40 estimates the number of intervals, N required to obtain the complete pulse response. The apparent change of N is due to very low mass ratio considered in these systems, i.e. 9.717×10^{-4}, as the mass of impactor is

now almost 100 times than the one used in previous models (approximately 26 gram).

For better illustration of the above mentioned inferences of outputs, this parametric study on elastic modulus considers 50 mm drop height (see Table 3.4) as the reference model with similar cylindrical bar dimension, i.e. 10.6 mm diameter and 21 mm length. Four additional elastic moduli are considered (Table 3.5) while keeping the rest of parameters identical.

Table 3.5: Summary on the effect of elastic modulus parameter; Units: length [mm], mass [kg], time [msec], load [kN], frequency [kHz]

E [MPa]	Input			Output			
	h	m_{impactor}	ρ	$F_{\max}$	t_{pulse}	f	N
531				2.41	3.30	15.19	
400				2.09	3.80	13.19	
300	50	2.5	1.31×10^{-6}	1.81	4.39	11.40	50
200				1.48	5.37	9.30	
100				1.05	7.60	6.59	

In the analysis of a column design under simple compressive or tensile load in static test, structural stiffness, k is expressed as

$$k = \frac{AE}{l}. \tag{3.43}$$

There are two groups contributing to this overall structural stiffness, namely material stiffness (E) which is the analysed parameter in this section as well as structural dimensions of loaded column consisting its area (A) and axial length (l). Equation 3.43 shows direct proportionality between material and structural stiffness, which is intuitively correct, i.e. stiffer material leads to higher stiffness of overall structural response. The pulses in Fig. 3.7a show consistent stiffer

response with increase in peak load and decrease in pulse width with increasing elastic modulus values (only three models are shown for clarity).

Figure 3.7a depicts stiffer bars experience greater peak load, $F_{\max}$. In fact the initial load value, $F_{t=0}$ is also based on the elastic modulus with bars with higher E experiencing a higher initial load. For the cases considered the relationship can be expressed as

$$F_{\max} = 3.3101\sqrt{E} \quad [\text{kN}], \tag{3.44}$$

which confirms the direct linear correlation between $F_{\max}$ and $\sqrt{E}$ as shown in Fig. 3.8.

In the designed models, it is elucidated in Fig. 3.7a that by lowering the elastic modulus of the bar, pulse width prolongs if all other parameters remain unmodified. These data are fitted in 'nonlinear power model' as

$$t_{\text{pulse}} = 2.4021\frac{1}{\sqrt{E}} \quad [\text{msec}], \tag{3.45}$$

which confirms the nonlinear inverse correlation between t_{pulse} and $\sqrt{E}$ as shown in Fig. 3.9, marked as 'analytical' in blue colour. This shows that the approximate equation (Eqn. 3.4) works well for this mass ratio.

However, if Eqn. 3.4 is simplified using input parameters considered, it gives

$$t_{\text{pulse}} = 2.4231\frac{1}{\sqrt{E}} \quad [\text{msec}]. \tag{3.46}$$

This slight difference suggests that Eqn. 3.4 works well in estimating pulse width in the case of significantly high number of stress intervals, i.e. $N = 50$. Residuals of the regressions from both sources are again extremely small, showing the proposed equations with power law coefficient as excellent representatives.

The impulsive responses shown in this Section are in the form of a single

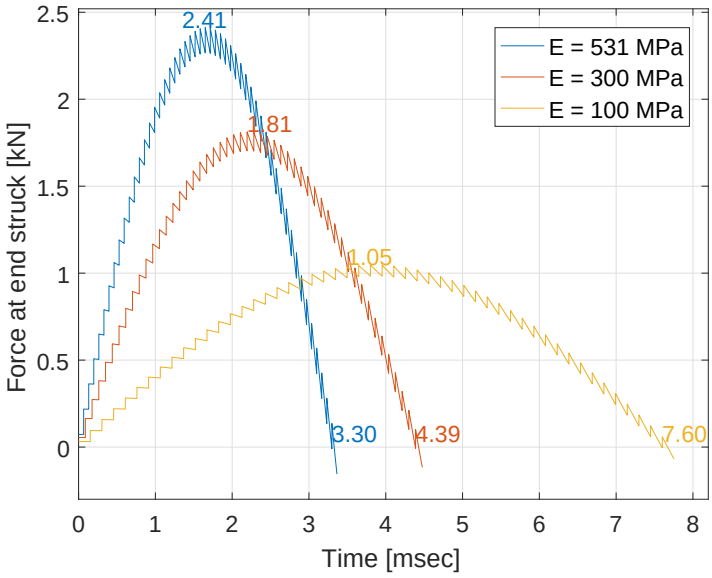

(a) On peak load and pulse width

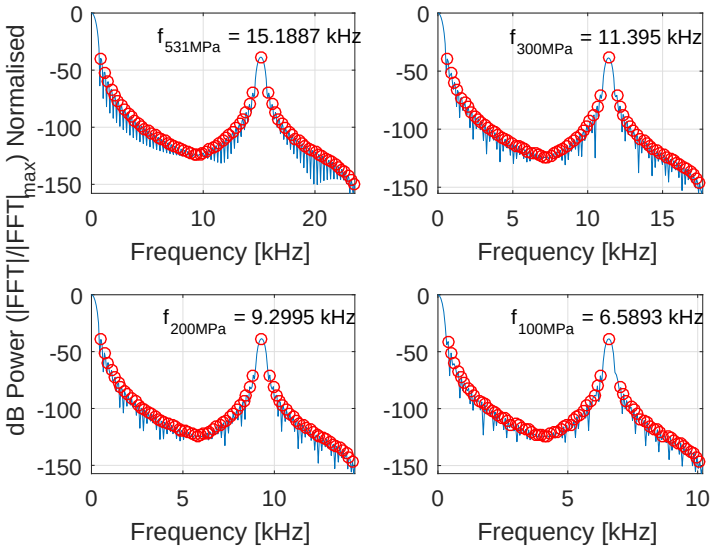

(b) On interval frequency

Figure 3.7: Bar's elastic modulus effect

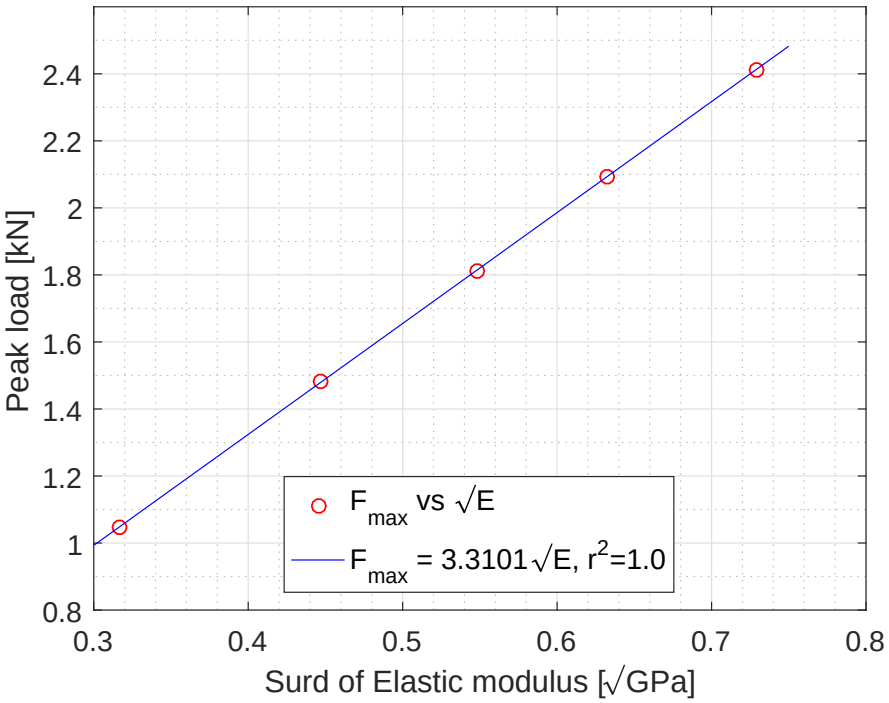

Figure 3.8: Linear regression model relating F_{max} and $\sqrt{E}$

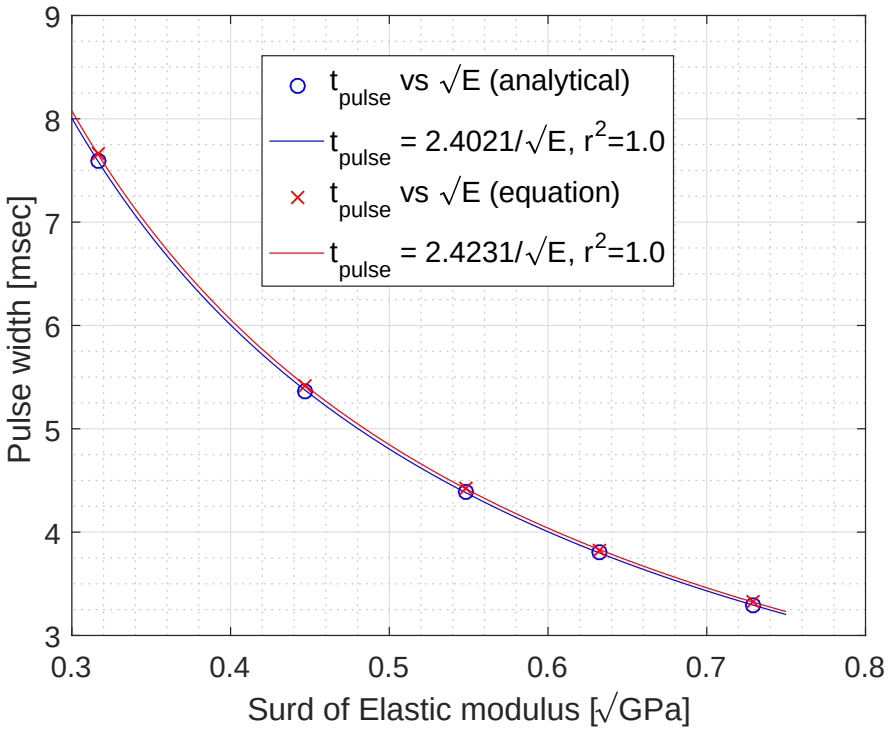

Figure 3.9: Power law regression model relating t_{pulse} and $\sqrt{E}$ (Nonlinear inverse relation)

pulse excitation, which is distinguishable from harmonic and quasi-static step behaviours. Elementary dynamics show that the response due to dynamic pulse loading often magnifies the response which will be obtained if the same load were applied in a static manner. The drop-tower loading in this study is perhaps akin to application of a half-sine pulse. For simple undamped single degree of freedom systems, it has been shown that amplification of response varies with the ratio of pulse duration to the natural period of the system (Chopra, 2001).

In order to analyse the frequency response, which is important especially in the evaluation of linear behaviour in the time-based material model presented in the FE Chapter later (Section 4.7), Fourier transform; which is a frequency analysis method of transforming time-to-frequency domain, is utilised to return significant frequencies detected in the investigated pulse. The mirrored-transformed signals are returned for both impulsive responses in this parametric study as shown in Fig. 3.7b side-by-side for four different moduli. The returned frequency of 531-MPa model (highest E) is shown to be the highest among the models, depicting the inverse relation between elastic modulus and interval time, T, i.e. higher E leads to lower T. Meanwhile, it is shown in the frequency-domain graphs that the transformation does not only return a unique frequency value but additional frequencies as well. Detailed concept, procedure and results of Fourier transformation is discussed in the next Chapter (Section 4.6).

Linear regression model is fitted by the interval frequency and square-root of elastic modulus data from both methods, i.e. analytical via Fourier transform and inverse of time interval governing equation (Eqn. 3.2), establishing full straight line relationships as

$$f = 20.8672\sqrt{E} - 0.021 \quad [\text{kHz}] \tag{3.47}$$

and

$$f = 20.8025\sqrt{E} \quad [\text{kHz}] \tag{3.48}$$

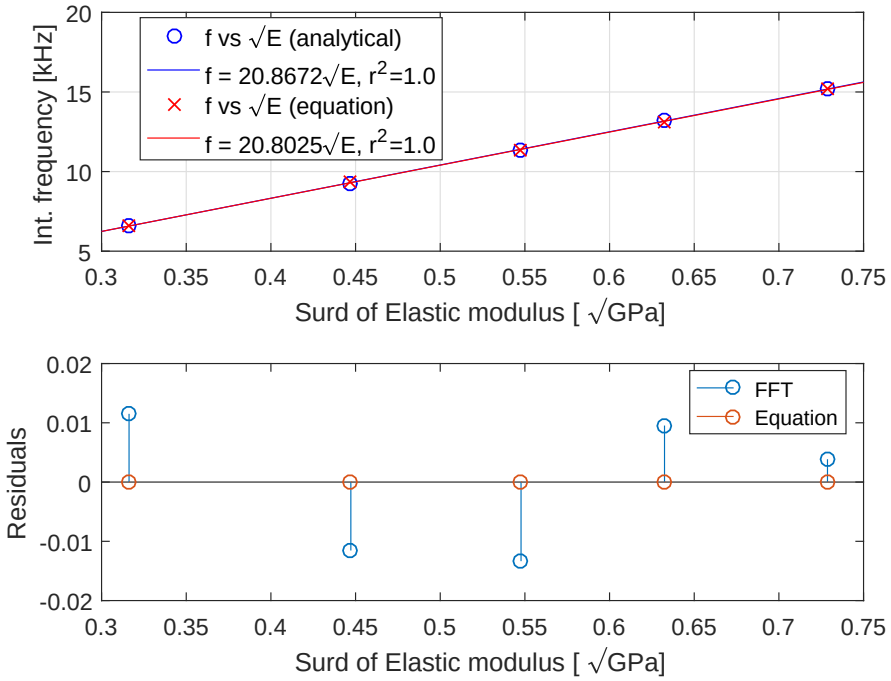

Figure 3.10: Linear regression model relating f and $\sqrt{E}$

respectively, as illustrated in Fig. 3.10 showing both regressed models. Equation 3.47 implies the capability of FFT in detecting the frequencies when it is compared to the theoretical relation in Eqn. 3.48. It is noted that the best fit line for interval frequency by Fourier transform (Eqn. 3.47) has quite apparent non-zero ordinate axis intercept, suggesting some random numerical discrepancy arises in the Fourier transform's returned frequencies, thus preventing the line from intersecting the origin. The gradient of straight line of Fourier transform data is slightly higher than the theoretical value by 0.31%. This slight difference suggests that the current transformation method has excellent capability to return the stress interval frequency from the pulse signal input, in which the confirmation will be useful in the numerical analysis in the next Chapter.

As an additional output variable in this parametric study, the gradient of rising impulsive load, or loading rate, $\dot{F}$ is investigated. It is apparent that the initial phase will have a higher gradient which reduces gradually to zero. Here, linear

regression is used in the initial phase in order to be compared approximately with the experimental results while deriving the dynamic elastic modulus expressions in Sections 5.4.2 and 5.6. It is also apparent that materials with higher elastic modulus will have higher initial loading rate. The first half of the rising pulse is selected and linear regression for this region provides the coefficient of determination $r^2 = 0.99$ as shown in Fig. 3.11a. It is important to note that the force-time pulse is not smooth and for the input parameters considered, the first half of rising pulse approximates the best as a straight line. One-fourth and one-eighth of the rise heights were also considered but due to jaggedness of the curve, they provided slightly poorer fits, viz. $r^2 = 0.97$ and $r^2 = 0.89$ respectively.

The individual loading rates are shown in the legend of Fig. 3.11a for all models, e.g. 2.0078 kN/msec for E-531 MPa model. These rates are fitted linearly against the model's elastic modulus, E shown in Fig. 3.11b, which results in a near perfect fit, i.e. $r^2 = 1$. The resulting linear equation of loading rate-elastic modulus is expressed as

$$\dot{F} = 3.7811E \quad [\text{kN/msec}]. \tag{3.49}$$

This Eqn. 3.49 will be employed later as one of several methods to derive dynamic elastic modulus, E_d as a function of bone volume fraction, BV/TV. The direct proportionality found between loading rate and stiffness is consistent with the experimental finding of drop test on the proximal human cadaveric femur simulating sideways fall in Gilchrist et al. (2014).

Meanwhile, it is apparent from Fig. 3.7a that varying elastic modulus does not affect the number of intervals ($N = 50$), a result which is consistent with Eqn. 3.40, showing the number of intervals are dependent on the mass ratio only. Modulus change, however, changes in the pulse shape, i.e lower-assigned E value causes the graph to stretch horizontally. Effect of elastic modulus is summarised in Table 3.5.

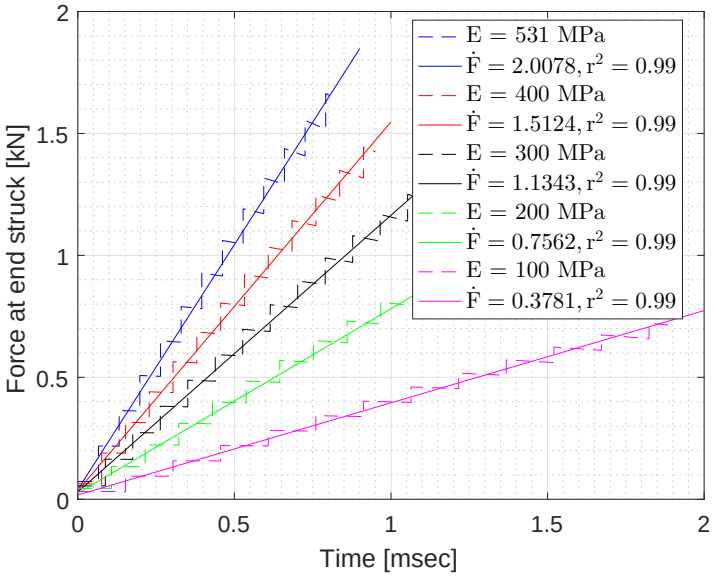

(a) Linear regression on half of the curve's initial data

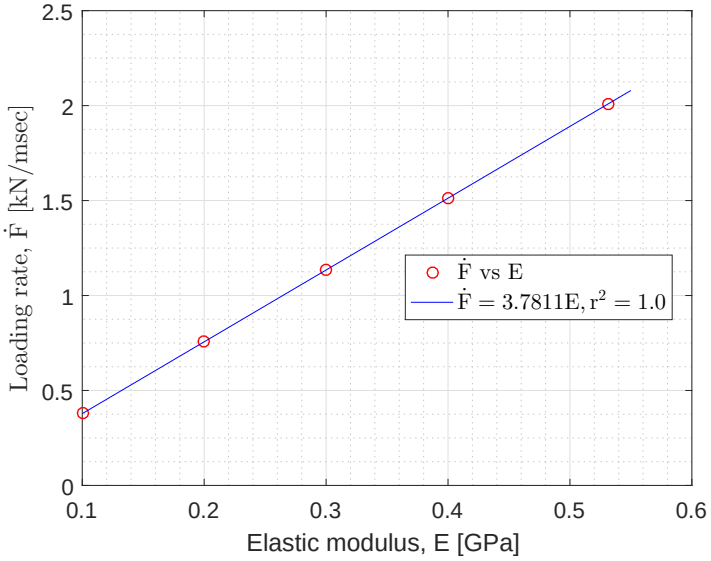

(b) $\dot{F}-$E relation

Figure 3.11: Bar's elastic modulus effect on loading rate

In this parametric study on elastic modulus of impacted bar, the variation is performed only on the material stiffness values, while the rest of parameters are kept constant. However, in the light of vast mathematical relationship study proposed for bone's density and its corresponding mechanical properties, it is well-known that the elastic modulus of bone is a function of its densitometry, which generally in the form of linear proportionality or increasing power law. Some of these relationships are summarised and provided by Helgason et al. (2008), where the densitometry properties are either bone volume fraction (BV/TV) or one of the bone's density measures, e.g. apparent (ρ_{app}) and wet (ρ_{ash}) densities. Thus, this closed-form solution should be used cautiously when analysing response of impacted bone, which means requiring the densitometry to be considered alongside the dynamic elastic property of the bone sample.

3.5.4 Length of the bar, l

Similar to the previous explanation on E, the effect of l on interval time, T is nullified by the substitution of real time expression in the calculation for $F_{\max}$. In spite of that, l indirectly affects $F_{\max}$ via mass ratio terms, α, which appear in both exponential and polynomial terms in general compressive stress expression (Eqn. 3.38), which can be simplified in the form of

$$s_n(l) = \sum \left[ae^{-bl} \cdot \sum \left\{ c \cdot l^d \right\} \right], \tag{3.50}$$

where a, b, c and d are constants. In addition, the peak load expressions for systems with different number of intervals due to varying α, may be dissimilar expressed as

$$F_{\max,l} = \Big[s_{m+1}\big(t = mT\big) + s_m\big(t = (m-1)T\big) \Big] \cdot A; \tag{3.51}$$

where m+1 is one of the middle intervals for a system with N number of intervals. The calculation for $F_{\max}$ appears to be complex, yet exponential terms such as in Eqn. 3.50 are expected to be dominant and should show decaying pattern.

The pulse width (t_{pulse}) has a direct proportionality with l in the pulse width estimator (Eqn. 3.4), while the time duration has inverse proportionality with square-root of mass ratio, i.e. $\alpha \propto l$ instead. Thus, the process of simplifying further the relevant terms leads to direct proportionality between the pulse width and square-root of l, i.e. $t_{\text{pulse}} \propto \sqrt{l}$. For another time-based output which is the interval frequency (f), as the length is related to interval time directly, hence its relationship with interval frequency is reversed, i.e. $f \propto \frac{1}{l}$.

Similar to the study on the effect of elastic modulus (Section 3.5.3), significantly higher number of intervals, N is predicted in the case of varying length of five models (Table 3.6). The current study is based on actual 50-mm drop tests of 2.5-kg rigid hammer hitting the trabecular bone samples with different axial lengths, l. Typical material values of cancellous bone are used (E = 531 MPa and $\rho = 1.31 \times 10^{-6}$ kg/mm^3), as tabulated in the 'Input' column.

Table 3.6: Summary on the effect of length parameter. m+1 is the interval in which the peak load is located; Basic units: length [mm], mass [kg], time [msec]

l [mm]	Inputs				Outputs			
	h	E	m_{impactor}	ρ	$F_{\max}$	t_{pulse}	f	$N(m+1)$
21					2.412	3.296	15.19	50(26$^{\text{th}}$)
32					1.967	4.088	9.91	41(21$^{\text{st}}$)
35	50	0.531	2.5	1.31×10^{-6}	1.884	4.264	9.10	39(21$^{\text{st}}$)
40					1.768	4.588	7.98	37(19$^{\text{th}}$)
50					1.588	5.119	6.39	33(17$^{\text{th}}$)

Equation 3.40 provides the number of intervals, N required to obtain the whole

pulse. The apparent high number of intervals N is understandably due to very small mass ratio in these systems, in the range of $9.717 \times 10^{-4} \leq \alpha \leq 2.31 \times 10^{-3}$ for five different lengths between 21 and 50 mm. The estimator, $N \approx \frac{\pi}{2}\sqrt{\alpha^{-1}}$ in Eqn. 3.40 shows inverse relation between N and the length, l via mass ratio. Therefore, as the five varying-length models are arranged in ascending order, the resulting approximated number of intervals are in descending pattern, i.e. $N = 50.40, 40.84, 39.05, 36.05$ and 32.67.

Figure 3.12a illustrates the exact number of intervals required to obtain the whole pulse duration of three selected models, for which the number of intervals (in integers) are recorded in Table 3.6. In evaluation of exact required number of intervals, pulse of l=21mm model ($N = 50.40$) ends at the very end of 50^{th} interval, which means the estimator slightly over-predicts the required N. Meanwhile, the load response of l=32mm model ($N = 40.84$) drops back to zero at around the middle of 41^{th} interval, which shows under-prediction. Therefore, as a matter of practicality, having at least one more higher interval stress term in the code is recommended to cater the possibility of insufficiently-defined N, since the actual end time can only be determined once whole pulse is plotted, as the α value acts only as an initial estimator. Meanwhile, Eqn. 3.40 has shown its capability to perform good estimation on N for systems with small mass ratio.

Higher N which has inverse proportionality with l leads to higher measured peak load, $F_{\max}$ as shown in the previous overall structural stiffness contributors (Eqn. 3.43). As in the governing equations, varying length parameter does not affect initial stress, σ_0, subsequently $F(t = 0)$, which is demonstrated at the instantaneous rise time in Fig. 3.12a. The determination of $F_{\max}$ in this parametric study is dissimilar to the previous parameters of drop height and elastic modulus due to its effect on the number of intervals, N. For instance, $l = 21$mm has the highest N, consequently its middle interval, m which locates the peak load, hence it has the most expanded peak load expressions of $F_{\max} =$

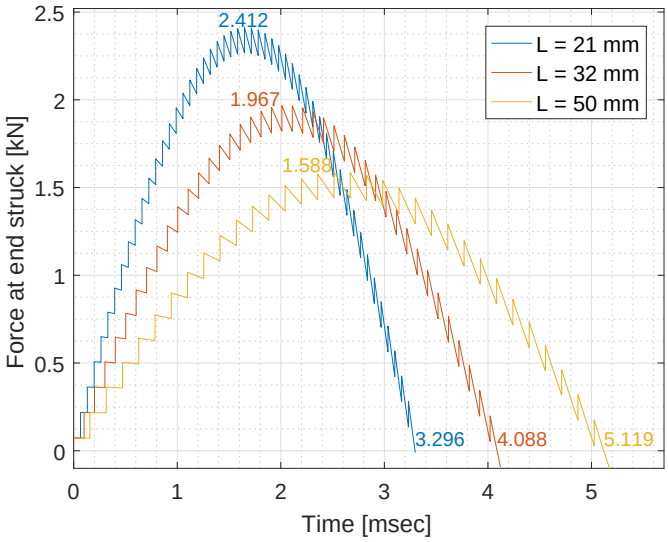

(a) On peak load and pulse width

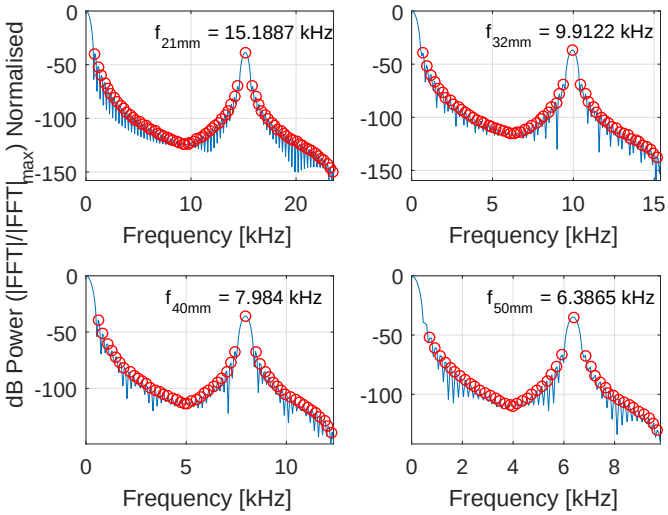

(b) On interval frequency

Figure 3.12: Bar's length effect

($t = 25T$) causing its value to be the highest. In comparison, the lowest peak load is recorded by the longest bar, $l = 50$mm, which is expressed as $F_{\max}(t = 16T)$ which has the least terms in peak load expression due to its lowest N. The integer m values are shown in Table 3.6 for each respective model and N.

Overall structural stiffness, k as mentioned in the previous section (Eqn. 3.43) shows the effect of material stiffness, E, in which both variables have direct proportionality. In this Section, the influence of length (l) of the bar is considered. Figure 3.12a illustrates the effect of varying length of the bar towards the structural stiffness of loaded column, in which stiffer pulse is observed for shorter bar, consisting higher peak load and decreasing pulse width showing inverse proportionality relation, $k \propto \frac{1}{l}$ between the two variables.

As previously discussed, Eqn. 3.50 shows that the stress expressions in term of length, l, which constitute the peak load calculation consisting sequential multiplications of exponential and polynomial terms, which are basically not available in the MATLAB's list of library models for curve fittings, leaving the choice to be with no exact regression(s). In spite of that, nonlinear exponential decay is expected as the exponents contain decay constant, although the exponential and polynomial terms may have the opposite effect due to the mass ratio. Therefore, two power law and two-term exponential models available in the library are employed to fit the peak load-length data, based on their individual attributes. As for the power law, it can basically fit most inverse relations, including the current $F_{\max} - l$ relationship. On the other hand, the two-term exponential regression is the closest one as depicted in Eqn. 3.50, such that the relationship in Eqn. 3.51 needs up to m-term for this fit. The three regression models that work well are

$$F_{\max} = \frac{10.47}{l^{0.48}} \quad [\text{kN}], \tag{3.52}$$

$$F_{\max} = \frac{10.81}{l^{0.51}} + 0.09 \quad [\text{kN}], \tag{3.53}$$

and

$$F_{\max} = 2.71e^{-0.08l} + 2.23e^{-0.007l} \quad [\text{kN}], \tag{3.54}$$

for one- and two-term power series as well as two-term exponential models respectively as shown in Fig. 3.13. Under close scrutiny, the l variable in Eqns. 3.52 and 3.53 appear to be almost under the surd, i.e. $F_{\max} \propto 1/\sqrt{l}$.

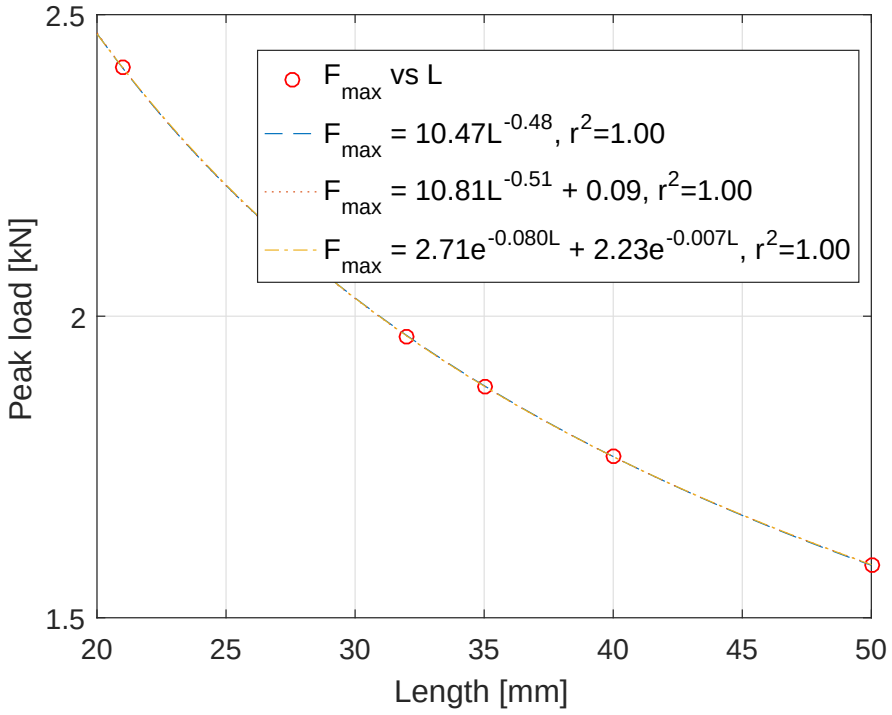

Figure 3.13: Nonlinear regression models relating $F_{\max}$ and l (Power laws and exponential)

Comparing the residual distribution between models, both two-term power and exponential models exhibit the best regressions, while the one-term power series is slightly off the mark. It is worth mentioning that residuals from one-term exponential model, which has general form of $y = ae^{bx}$; which is not presented in this work, are significant; and therefore not demonstrated here.

The effect of length on pulse width is demonstrated in Fig. 3.12a. Longer pulse

duration allows more time (as well as intervals) for elastic wave propagating inside the bar's length, thus increasing N as well as more additional initial stresses (σ_0) are induced at the instantaneous start of every time interval.

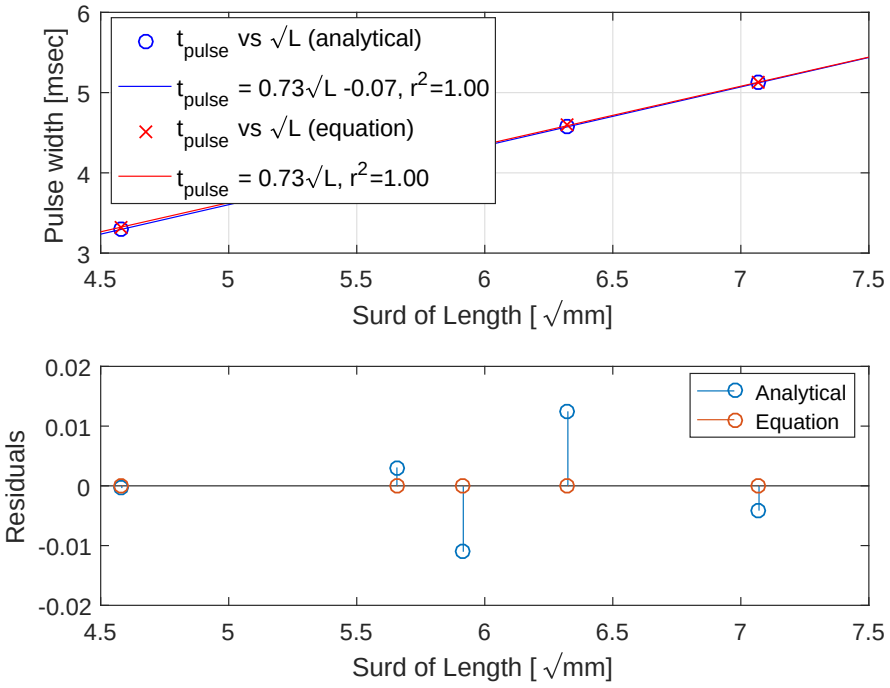

Figure 3.14: Linear regression models relating t_{pulse} and $\sqrt{l}$

Following the predicted relation of $t_{\text{pulse}} - \sqrt{l}$, linear regression model is fitted by the pulse width and square-root of length data from both methods, i.e. the actual end time from plotted response and the estimator given in Eqn. 3.4, establishing straight line relationships as

$$t_{\text{pulse}} = 0.7338\sqrt{l} - 0.0661 \quad [\text{msec}] \tag{3.55}$$

and

$$t_{\text{pulse}} = 0.7256\sqrt{l} \quad [\text{msec}] \tag{3.56}$$

for the obtained pulse and predictor equation respectively.

Figure 3.14 illustrates both fits, i.e. Eqn. 3.55 and 3.56 confirm direct linear

correlation between t_{pulse} and $\sqrt{l}$. It is observed that the regression line for pulse width obtained from the plotted pulse has non-zero ordinate intercept, suggesting the pulse width-length relation does not have exact linear correlation, as opposed to the ideal scenario as in the predictor (Eqn. 3.4). Comparing their gradients, the estimator records 1.09% lower than the real value, generally implicating its capability in estimating the contact duration of pulse for number of intervals in the range of $33 \leq N \leq 40$. The residuals from estimator are basically zero, showing exact regression was obtained as in Eqn. 3.56, while from the real pulse plot (analytical) are considerably low. This non-zero residual for analytical pulse width raises uncertainty, as it is previously presented in the parametric study on E to have zero residuals. It is mentioned by Timoshenko and Goodier (1951) that the pulse width's estimator (Eqn. 3.4) works well in the case of more number of intervals, N, due to small mass ratio. Therefore, a plausible explanation on the issue of residuals perhaps due to the entire omission of the bar's mass in the derivation of the estimator, which consists of its length, l.

Physically, a simple understanding on lower mass ratio (consequently high impactor's mass) shows how this phenomenon affects the peak load and pulse width. When heavier impactor is employed dynamically on a struck bar, longer contact time is intuitively expected, with more deformation under compression leading to significantly higher pressure level been built-up at struck end. This logical explanation is in fact agreeable with the explanations by the governing equations for the whole dynamic behaviour of the impacted bar.

As the length is related to interval time directly, hence the relationship with interval frequency is reversed, i.e. $f \propto 1/l$. Fourier transformation on the five pulses returns frequency-domain transformed signals as some are depicted in Fig. 3.12b. The figure shows returned frequency value of shorter bar to be higher, corresponds to shorter interval time for every intervals as illustrated in Fig. 3.12a. As a physical explanation, elastic wave propagating through longer bar has lower

frequency, in which more time is required to complete each covered distance, given similarly-defined material properties. It is also observed that the pulses have steeper gradient of rising load for shorter bar models, e.g. $l = 21$ mm, which is caused by shorter interval time (higher frequency value). Higher interval frequency also results in more N getting involved in a given time period, leading to higher load value within shorter pulse duration.

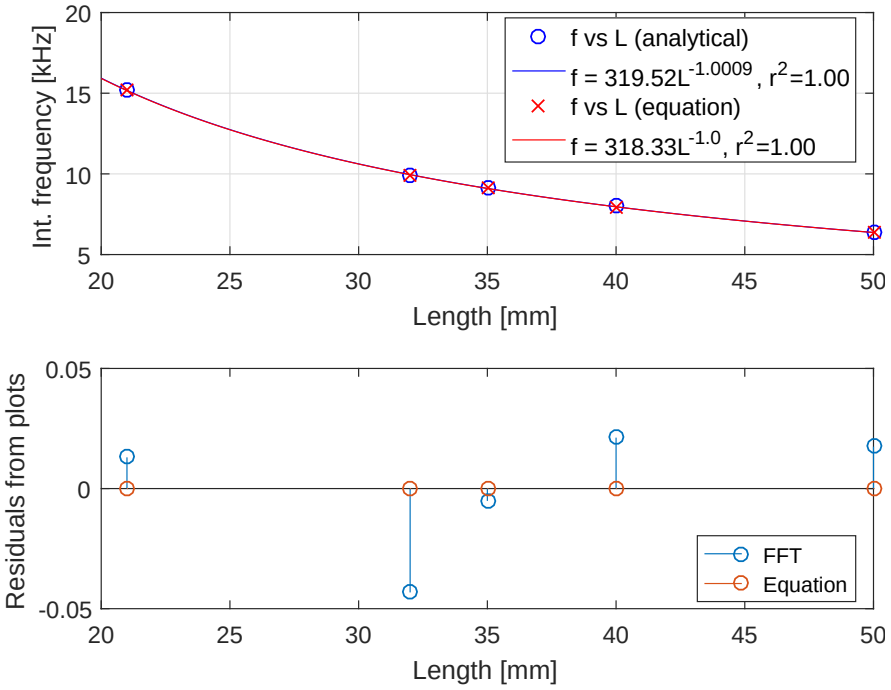

Figure 3.15: Power law regression model relating f and l (Nonlinear inverse)

One-term power series is fitted by the interval frequency and length data from both methods, i.e. analytical via Fourier transform and inverse of time interval governing equation (Eqn. 3.2), establishing inverse relationships as

$$f = 319.52\frac{1}{l^{1.0009}} \quad [\text{kHz}] \tag{3.57}$$

and

$$f = 318.333\frac{1}{l} \quad [\text{kHz}] \tag{3.58}$$

respectively, as illustrated in Fig. 3.15. Both regressions show nonlinear inverse

correlation between f and l, as expressed in Eqns. 3.57 and 3.58. It is noted that the power index for interval frequency by Fourier transform (Eqn. 3.57) is very close yet not exactly -1, suggesting slight discrepancy by this numerical method.

3.5.5 Other parameters

In addition to the investigated parameters, there are other contributors have effects similar to those in the discussed parameters. These parameters relate to material property (mass density, ρ), structural dimension (cross-sectional area, A) and system properties (mass of impactor, m_{impactor}), which are comparable with the already presented elastic modulus (E), length (l) and mass ratio (α) effects respectively.

Density (ρ)

The effect of mass density, ρ is via material impedance ($\sqrt{E\rho}$), mass ratio (α) and wave speed (c). In the form of impedance, it has a similar effect as elastic modulus to initial stress and exponential term in individual stress wave (s_n) definitions. Meanwhile, ρ has direct proportionality with α, similar to the effect of l in which denser bar's mass increases the value of mass ratio, thus reducing the number of intervals. On the other hand, its effect on elastic wave propagation, c is opposite to elastic modulus, which means denser mass of a material slows down the wave speed. This effect effectively prolongs the interval time, T for complete wave traversing through the bar's length. Meanwhile, the estimator relation for pulse width (Eqn. 3.4) shows the effect of ρ is nullified by c and α parameters.

In term of the peak load, the effect of ρ is similar to that of E in the initial stress, σ_0 (impedance in Eqn. 3.1) while comparable to the effect of l via mass ratio, α in the exponential and polynomial series in Eqn. 3.38, as well as the required number of intervals, N. Meanwhile, the overall structural stiffness, k is not influenced by material density of the bar, which physically means if a pulse

response has higher $F_{\max}$, it does not necessarily mean t_{pulse} will be shorter as normally exhibited by the behaviour of stiff pulse response.

In the defined models, density parameter is not extensively studied because cancellous bone samples from experiments (which are presented in Chapter 5) do not have significant variation of apparent density values among them when compared to the impactor's mass. Depending upon individual bone volume fraction, BV/TV of bone samples in comparison with their wet mass, the apparent density values vary between $1.04 - 1.53 \times 10^{-6}$ kg/mm^3, in which the defined density parameter in these closed-form models is a middle value within this range, e.g. 1.31×10^{-6} kg/mm^3.

Area (A)

Cross-sectional area of the bar is a function of radius, r for this cylindrical bar model. Direct proportionality relation of $\alpha \propto A$ shows similar effect as in l and ρ to the pulse width, i.e. $t_{\text{pulse}} \propto 1/\sqrt{A}$, and peak stress, in which larger area results in lower peak stress. However, the determination of compressive force from total stress at end struck will have opposite influences from $\sigma(t)$, exhibiting an exponential decay when multiplied with the area itself, which is directly proportional. On the other hand, this parameter does not have any influence on interval frequency, f. The analysis on this parameter is performed in the next Chapter by FE method (Section 4.5.2).

Impactor's mass, m_{impactor}

Mass of moving rigid impactor has direct effect on the mass ratio, α as per definition itself, so as all of the impactor's mass effects on the pulse outcomes are through this ratio parameter. As defined, this mass has an inverse relation with α, which in return will have opposite effect to ρ and A on the peak load and pulse width. Similar to the area, no effect is expected on the interval frequency.

The analysis on this parameter is performed in the next Chapter by FE method (Section 4.5.1).

In the light of physical and logical explanation, impact from a heavier mass will produce higher $F_{\max}$. Regarding pulse width, their direct proportionality clearly shows heavier moving mass causes longer contact time between the impacting bodies as the bar gets more compressed, which in return prolonging the duration which is a sound physical illustration of this phenomenon.

3.6 Summary on the parametric analysis

Based on the interval stress wave, s_n (Eqn. 3.38), pulse width, t_{pulse} (Eqn. 3.4), number of intervals, N (Eqn. 3.40), interval time-frequency, $T - f$ (Eqn. 3.2) and peak load, $F_{\max}$ (e.g. Eqn. 3.51) which are the main outputs of an impulsive response, a number of parameters present in these expressions affecting the outcomes. These parameters are listed in Table 3.7 for factors which have direct influence to the pulse and obvious presence in the governing equations.

Another not-so-obvious observation is the effect of impacted area, A on the resulting peak load, $F_{\max}$ as presented in Table 3.8. As discussed in Section 3.5.5, parameter A has direct proportionality with mass ratio, α, thus its relation with compressive stress at end struck, i.e. both s_n and $\sigma(t)$ is in the form of inverse proportionality. However, the corresponding force is measured as a product of $\sigma(t)$ and A, which implicates direct proportionality between A and $F(t)$. This contradiction is not extensively analysed, yet logically, mass ratio α should have more influence on the load response, as it represents the ratio of impacted bar's mass to its counterpart of moving impactor.

Meanwhile, there are also parameters which have non-apparent effects on the outcomes as shown in Table 3.8, related to the effect of mass ratio. This parameter

Table 3.7: Proportional relation of output variable-input parameters

Entity	Primary parameter	Proportionality	
		Intermediary parameters(s)	Output
System	Mass ratio, α	-	$N \propto \frac{1}{\sqrt{\alpha}}$
			$t_{\text{pulse}} \propto \frac{1}{\sqrt{\alpha}}$
	Drop height, h	v_0	$\sigma_0 \propto \sqrt{h}$
		σ_0	$F_{\max} \propto \sqrt{h}$
	m_{impactor}	α	Inverse to α effect
Bar-material	Elastic modulus, E	c	$t_{\text{pulse}} \propto \frac{1}{\sqrt{E}}$
			$f \propto \sqrt{E}$
		-	$\sigma_0 \propto \sqrt{E}$
			$\dot{F} \propto E$
		σ_0, c	$s_n \propto \sqrt{E}$
		σ_0, s_n	$F_{\max} \propto \sqrt{E}$
	Mass density, ρ	-	$\sigma_0 \propto \sqrt{\rho}$
		c	$f \propto \frac{1}{\sqrt{\rho}}$
Bar-dimension	Length, l	α	$N \propto \frac{1}{\sqrt{l}}$
		c	$f \propto \frac{1}{l}$
		c, α	$t_{\text{pulse}} \propto \sqrt{l}$
		α	$F_{\max} \propto ae^{-bl}$
			or $F_{\max} \propto \frac{1}{\sqrt{l}}$
	Area, A	α	Similar to α effect

has contradicting effect on exponential and power terms in s_n expressions, however Fig. 3.3 shows that inverse relation is established, i.e. $\alpha \propto \frac{1}{s_n}$. This conclusion is supported as well by observation on the effect of length on maximum load via mass ratio (Fig. 3.12a), as well as intuitive logical explanation on the factor of heavier mass been impacted on the struck end. The fact that mass ratio has inverse relation with number of intervals also contributes significantly to higher peak load of resulting pulse in the case of either having heavier impactor or lighter bar.

Table 3.8: Contradiction of parameters related to $\alpha - s_n$ directly affecting peak load (F_{max}) and $A - F_{\mathsf{max}}$

Parameter	Proportionality with α	Relevant terms		Observation
Contradictory factors in s_n				
Density	$\rho \propto \alpha$			Exponential
Length	$l \propto \alpha$	In exponential:	In polynomial:	factor
Area	$A \propto \alpha$	$\alpha \propto \frac{1}{e^{-b\alpha}} \propto \frac{1}{s_n}$	$\alpha \propto \alpha^m \propto s_n$	is more
Mass	$m_{\text{impactor}} \propto 1/\alpha$			influential
Compressive stress to force				
Area	$A \propto \alpha$	In s_n: $\alpha \propto \frac{1}{s_n}$	In F_{max}: $F \propto A$	Logically, α has more influence on load response

Chapter 4

Numerical simulation of impacted bar

4.1 Introduction

This Chapter considers the numerical simulation of the restrained elastic bar subjected to rigid mass impact. The numerical simulation is undertaken using a finite element (FE) commercial package, LS-DYNA (smp d R7.1.1, LSTC, Livermore, California). It considers the elastic scenario for which a closed-form solution is available and extends the problem to the more complex time-dependent elastic behaviour (post-elastic response is considered in the following Chapter). This Chapter also considers the methodology of conducting fast Fourier transformations.

4.2 Problem definition

Consider the similar problem as in the last chapter (see Section 3.2), i.e. a cylindrical bar impacted by a rigid hammer at free end and fixed at the other

end. Numerical solutions are essential as not all problems are elastic, have a simple one-dimensional geometry and boundary conditions; consequently closed-form solutions are not possible. The closed-form solutions, however, help in evaluating and benchmarking the accuracy of numerical methods.

Explicit code of LS-DYNA is utilised to modelling. The code uses explicit time integration based on central difference method (CDM) to obtain nodal displacements from their velocities and accelerations in every time step, Δt. The bar is assumed to be a cylinder (cylindrical specimens are used in subsequent experimental tests) and modelled as an axisymmetric solid with 4-noded axisymmetric elements. The wave speed and characteristic element length are defined as

$$c_{2D} = \sqrt{\frac{E}{\rho(1-\nu^2)}} \tag{4.1}$$

and

$$l_c = \frac{A}{\max(L_1, L_2, L_3, L_4)} \tag{4.2}$$

respectively. ν is the Poisson's ratio, while $L_{1,2,3,4}$ are the four lengths of the 4-node plane element. According to the Courant condition, the time step employed in simulations must satisfy

$$\Delta t \leq \frac{l_c}{c_{2D}}, \tag{4.3}$$

which restricts the time step to be less than the time required for sound wave to traverse the smallest element in the model. This condition is important to ensure progressive transfer of information between adjoining elements and allowing the programme to update the current deformed geometry in every time step. In LS-DYNA, the time step in Eqn. 4.3 is reduced by the factor of 0.9 as a default value and can be further lowered depending upon the stability of the simulation (Livermore Software Technology Corporation, 2017*b*).

The following sections discuss FE model development in LS-PrePost programme.

The development of the geometry, the boundary conditions involved, the load application in the impact problem as well as the material models used to describe the constitutive behaviour are discussed. The resulting output is then verified and compared with the closed-form solution discussed in the last chapter. The effects of drop height and material stiffness on the response are revisited (refer to Sections 3.5.2 and 3.5.3 respectively) while the unpresented effects of the impactor's mass and dimension of bar on the structural stiffness are discussed. The procedure of Fourier transform employed to obtain interval frequency of stress wave is explained in which the results were preliminarily shown in the previous Sections 3.5.3 and 3.5.4. Finally, the effect of time-dependent viscoelastic material model is also discussed.

4.3 Numerical model

FE analysis requires four important main inputs: the geometry and the related FE mesh; boundary conditions defined for the models; load application and the material behaviour of the models. This Section discusses the definitions for each of these required inputs in the current study.

4.3.1 Discretisation of the axisymmetric system

Impact mechanics involves more than one body in the collision, which implies the necessity of defining a minimum of two geometrical models. The planar symmetry of the cylindrical shape in the defined problem as shown in Fig. 3.1 is exploited. Two-dimensional (2D) solid models in LS-DYNA are based on integral difference scheme, which defines the geometries in global XY plane. In axisymmetric case, radial direction corresponds to X-axis, while the axis of symmetry lies on the Y-axis. LS-DYNA offers two options of axisymmetric elements, namely Petrov-Galerkin and Galerkin finite element approaches, generally referred as 'area-weighted' and 'volume-weighted' methods respectively. The former is designed

suitably for a situation where the developed pressures in the model constitute a large fraction of the elastic modulus, i.e. a hydrodynamic case (Livermore Software Technology Corporation, 2017*b*).

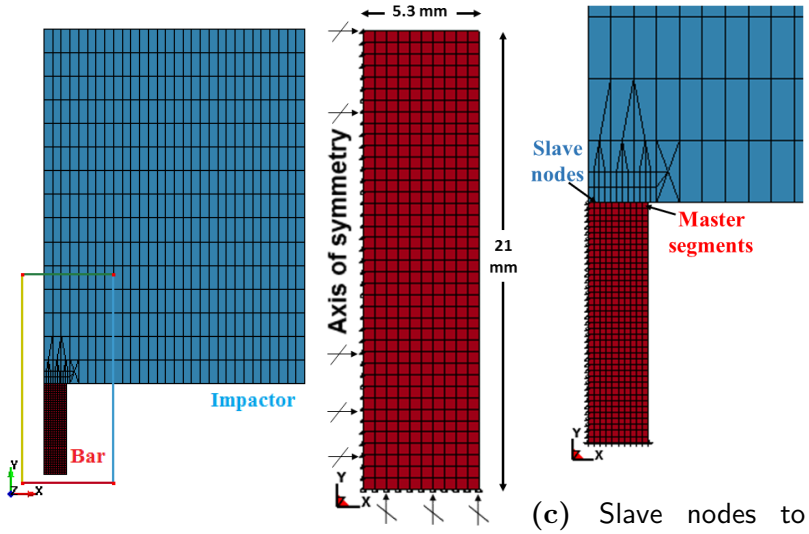

(a) Axisymmetric elements

(b) Dimensions and constraints

(c) Slave nodes to master surfaces contact

Figure 4.1: FE models. The box in (a) focuses on the region of interest

The volume-weighted Galerkin method is chosen in this work since there is no possibility of a hydrodynamic scenario arising in the problems being considered. The bar is discretised into 4-noded axisymmetric 10×40 elements to provide almost square 2D elements, with similar 1:2 diameter-to-length ratio (Fig. 4.1b). The rest of this primitive geometry are theoretically revolved 2π radians around the axis of symmetry to create a virtual cylindrical model of the bar as shown in Fig. 4.1.

Accordingly, the impactor is also assumed to have axisymmetric shape (which is not the case in real experiment as described in Section 5.2.3) with arbitrary radius-length dimension, while ensuring the impactor's mass is 2.5 kg simulating the experimental drop test or around 26.6 g for a light-weight dropped hammer. Figure 4.1a shows the impactor as coarsely meshed in order to reduce the

computational cost, while refinement is applied at the bottom elements that impact on the bar. This mesh refinement is required to ensure each slave node (on the impactor) can be projected to its master segment (the bar struck), which will be discussed in detail in Section 4.3.3.

4.3.2 Boundary conditions

By the definition of axisymmetry in LS-DYNA, the global Y-axis represents the axis of symmetry, which for the problem considered automatically constrains the nodes on this axis in the global X-translation. In addition, all bottom nodes are manually restrained in vertical direction as shown in Fig. 4.1b which is consistent with the closed-form model in Fig. 3.1.

4.3.3 Loading conditions: Contact definition and initial velocity-drop height

Contact definition is required to establish interaction between the contacting surfaces of impactor and bar. The contact definition allows the incoming slave nodes of the impactor to recognize the top of the bar (which contains master segments) as shown in Fig. 4.1c. The mesh refinement size between the two contacting models is comparable. Standard penalty-based contact is employed for this purpose, which uses numerical springs to prevent penetration of each slave nodes through master segments as well as to transfer loads between contacting parts.

Only normal forces, F_{N} are applied since the surfaces are mutually orthogonal. Thus, both static and dynamic coefficients of friction are set to be zero to rule out friction forces, F_{f} since there is no tangential component of slave node's force with respect to the master segment. Hence, the force acting on slave node (and equivalently on respective master segment represented by its connecting nodes)

is calculated from

$$|\boldsymbol{F}_{\text{contact}}| = |\boldsymbol{F}_{\text{N}} + \cancelto{0}{\boldsymbol{F}_{\text{f}}}| = k_i D_{\text{p}}, \tag{4.4}$$

where D_{p} is penetration depth of the slave node(s) into the master segment, which is calculated by the programme at every time step and k_i is the stiffness of a master segment. For 2D solid element, this stiffness is expressed as

$$k_i = \frac{f_{si} \times A_i \times K_i}{\max(\text{diagonal length})}, \tag{4.5}$$

where f_{si} is penalty factor defaulted at 1.0, A_i is the face area of element that contains master segment and K_i is the bulk modulus of contacted element expressed as

$$K_i = \frac{E}{3(1-2\nu)}, \tag{4.6}$$

as a function of elastic modulus, E and Poisson's ratio, ν (Livermore Software Technology Corporation, 2017*b*).

The *2D_Automatic_Surface_to_Surface* contact type is employed which uses penalty forces to prevent penetration between external faces of 2D continuum elements. In addition, *Force_Transducer* option is used in conjunction with the previous contact card to measure forces generated by that contact definition. In the current axisymmetric model, the force output is per unit radian. Normal direction of both slave and master surfaces are determined automatically by the programme, in which the initial model set up already has orthogonal contact surfaces prior to the impact (Livermore Software Technology Corporation, 2017*a*).

In the case of drastically different elastic moduli between contacting materials, the penalty stiffness value is chosen as the minimum of the master segment and slave node stiffness. This decision is crucial since the current impactor is made of relatively stiff metal, while the bar is a porous trabecular bone which has

significantly low elastic modulus with respect to the metal. Hence, the stiffness of the bar (with master segments) is used to define the stiffness in contact algorithm.

The previously discussed closed-form solution involves assigning initial velocity to the impactor with a known mass to create a loading scenario. This method of simulating a drop test can be replicated in FE simulation as well. Moreover, the FE method can simulate the original problem by releasing a static hammer from a certain height under gravitational influence. Hence, there are two methods of simulating impact from a relatively rigid hammer: by assigning equivalent initial velocity to the impactor just before the contact in its direction of drop or by modelling the actual drop due to gravitational forces. The former approach is commonly adopted in the literature. Preliminary tests conducted in this study showed that both methods produce identical results, while the latter is expensive as it requires substantially longer simulation time due to the build-up of kinetic energy of the falling impactor.

In the approach of assigning initial velocity to the impactor, a small gap is introduced between contacting surfaces of the two models in order to avoid initial penetration leading to instability in the calculation of the contact forces (Livermore Software Technology Corporation, 2017*b*). The gap size is generally balanced between minimising initial computational cost (caused by a large gap) and avoiding initial penetration (due to gap being too small) between contacting solids. The best decision depends on the pre-calculation of the defined time step of the smallest element as in Eqn. 4.3, the initial distance between the first expected contacting elements and the assigned nodal velocity.

4.3.4 Material models

The bar's material is defined as elastic (or alternatively viscoelastic as in Section 4.7) or elasto-plastic as in the next Chapter (Section 5.5.4). The pure elastic

model is similar to the previous closed-form solution. The impactor is defined as rigid material which matches the problem definition in the previous closed-form solution (Section 3.2). In addition, this material model is a cost effective option because its model does not store history variables due to its undeformed body restriction.

Even though the rigid definition itself implies infinite stiffness, values of both Young's modulus, E and Poisson's ratio, ν need to be assigned to determine the bulk modulus, K for calculating the contact stiffness, k_i (Eqns. 4.5 and 4.6). In addition, the explicit time integration requires the mass density of the impactor in order to construct mass matrix in the CDM solution for the nodal displacements, even though the wave propagation (Eqn. 4.1) is not calculated for the rigid material.

4.4 Comparison with the closed-form solution

The load response of a cylindrical FE model (10.6 mm diameter and 12 mm length) impacted by 26.6 g hammer is first compared with the closed-form (CF) solution in terms of the resulting peak load and pulse width. The solid axisymmetric bar is converted to a one-dimensional model by assuming the Poisson's ratio to be zero, i.e. there is no transverse response in the 2D solid element. The light hammer is chosen to increase the mass ratio, which in turn would result in only seven stress intervals in the pulse response, allowing easy comparison to be made.

Figure 4.2 compares the FE response (zero Poisson's ratio) to that from the closed-form solution. It can be seen that there are seven force intervals in both FE and closed-form responses, which they are similar in the form of bell-like shape. The sharp peak-and-trough of vertical shape in every interval due to the instantaneous rise of force by CF solution is not recreated by the numerical simulation.

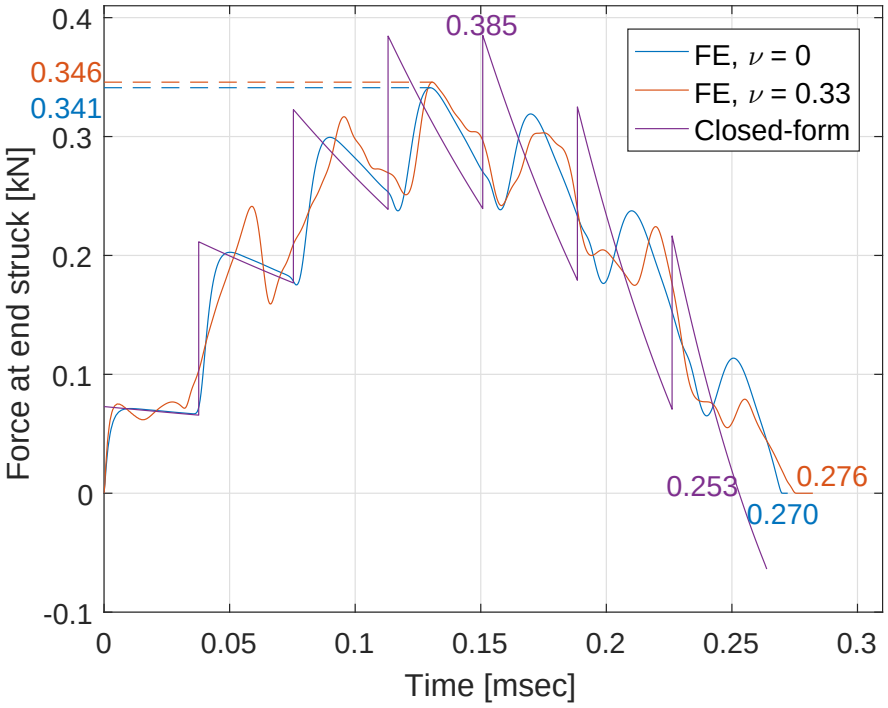

Figure 4.2: Verifying force response from FE of zero Poisson's ratio ($\nu = 0$) with the closed-form solution. The effect of non-zero ν is also shown

It is apparent that the closed-form solution returns consistent time interval, following strictly the expression of $T = 2l/c$ (Eqn. 3.2), whereas the time interval from FE solution gradually increases in every sequential intervals. This discrepancy is explainable by understanding the ideal scenario in the closed-form solution in which the supposed deformation of bar is neglected in the analysis. On the other hand, the FE model experiences numerical damping which is a default setting for all contact options in the LS-DYNA (Livermore Software Technology Corporation, 2017*b*) causing longer time for the travelling stress wave. Table 4.1 shows comparison of the two main outputs under investigation, namely peak load and pulse width between the two solutions. The FE method records 11.43% lower peak load, while its pulse width is 6.72% larger in comparison to its benchmark results by the CF solution.

The effect of Poisson's ratio ($\nu = 0.33$) is shown in Fig. 4.2, in which more higher

Table 4.1: Comparing one-dimensional FE model ($\nu = 0$) with the closed-form solution

Peak load [kN]			Pulse width [msec]		
FE	CF	% diff.	FE	CF	% diff.
0.341	0.385	-11.43	0.270	0.253	6.72

*Dimension of 10.6 mm diameter and 12 mm length impacted by 26.6 gram impactor

frequency distortion in its overall resulting pulse pattern is observed causing slightly unclear pattern of seven intervals. This happens perhaps due to the effect of wave bouncing from the sides. Nonetheless, the following peak load and pulse width values are not significantly affected, such that only 1.5% and 2.2% differences with the one-dimensional FE model. It can be concluded that assigning a reasonable value of Poisson's ratio does not drastically alter the response, in particular the output variables under interest, which are $F_{\max}$ and t_{pulse}.

4.5 Effect of different parameters on the resulting elastic pulse

This Section considers the effect of varying several parameters: mass of impactor; drop height; and structural stiffness; towards the resulting force at end struck by using numerical simulation. In this elastic study, some of the parameters are not varied, i.e. density: $\rho = 1.31 \times 10^{-6}$ kg/mm^3; bar's length, $l = 21$ mm; and Poisson's ratio, $\nu = 0.33$. The axisymmetric model is discretised using 10×40 elements in x (radial) and y (axial) directions respectively, which is almost 1:1 of bar's diameter-to-length ratio or even less for models with smaller radius.

The analysed output is the summation of eleven (11) nodal forces histories of the nodes at the top of axisymmetric bar model, multiplied by 2π to obtain the

total force acting on the surface of end struck. The focus of this investigation is on the peak load obtained from the pulse, as well as the pulse width showing the duration of impact. The effects of drop height and elastic modulus were considered in the closed-form solution (Sections 3.5.2 and 3.5.3 respectively); these will be evaluated numerically here. While discussing the closed-form solution, the influence of impactor's mass and bar's cross-sectional area was not illustrated graphically. This is considered here.

4.5.1 Impactor's mass and drop height

Two values of impactor's mass are chosen, which are 1.807 and 2.5 kg, while the two drop heights are 100 and 200 mm, making up four (4) FE models for this analysis. The models have geometry of 10.6 mm of diameter and 21 mm of length, with elastic modulus is assigned to be 531 MPa. It was shown in the closed-form solution that drop height (equivalently the initial velocity) parameter only affects the peak load, while the pulse width remains similar (Fig. 3.5); here the very same effect is demonstrated graphically in Fig. 4.3 by employing FE analysis. The peak load was shown in Eqn. 3.42 to have direct proportionality to the square-root of drop height, h. As can be seen from Fig. 4.3, this is satisfied by the numerical solution. The pulse width is also almost identical for impactors of the same mass dropped from different heights. Figure 4.3 shows that a higher drop results in a fractionally smaller pulse width.

A larger mass of the impactor leads to larger peak loads and also pulse width, which is consistent to the analysis of the closed-form solution. In addition, it is observed in Fig. 4.3 that with the increase in the impactor's mass, the force responses appear to be almost similar initially, then the load for higher mass increases at a substantially higher rate and comprises of larger number of stress intervals as expected. The effect of mass ratio (α) which is influenced by the mass of impactor (m_{impactor}) on the number of intervals (N) was examined in Table 3.3.

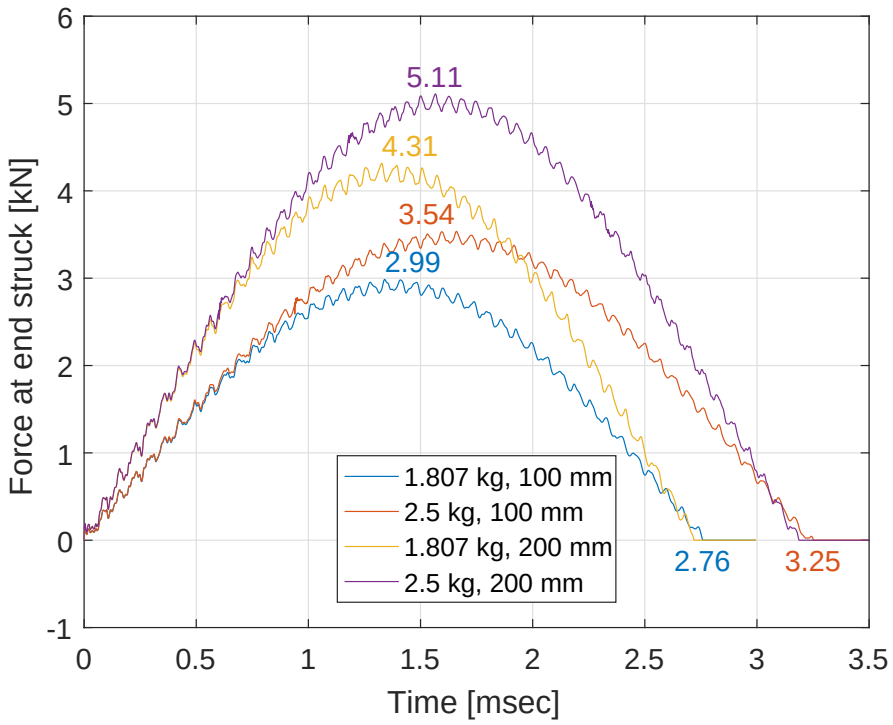

Figure 4.3: The effect of drop height, h and impactor's mass, m_{impactor} on the resulting force at end struck

4.5.2 Structural stiffness

The structural stiffness of a simple column is a function of its material (Young's modulus) and dimensions (cross-sectional area and length) as shown in Eqn. 3.43. The pulse shows stiffer response when the combination of higher peak load and lower pulse width is obtained, e.g. Figs. 3.7a and 3.12a as discussed in Sections 3.5.3-3.5.4.

In this parametric study, the 2.5 kg impactor is dropped from 100 mm height. The parametric study with respect to length was examined in the closed-form solution (Section 3.5.4), therefore only elastic modulus and diameter (representing area) are varied in this analysis. Similar elastic modulus of 531 MPa is chosen, with addition of materially-stiffer models of 1 GPa. The diameters are either 10.6 mm (from the previous model) or 8.6 mm, in which a smaller area is expected to exhibit less stiff behaviour.

The resulting force responses at the end struck are shown in Fig. 4.4 for four varying-stiffness models. The stiffest response is shown by the model with highest elastic modulus and cross-sectional area, i.e $E = 1$ GPa, radius $= 5.3$ mm; followed by models with lower structural stiffness contributors. These demonstrate the influence of elastic modulus and cross-sectional diameter on the peak load and the pulse width. The peak load is seen to be directly proportional to the elastic modulus as would be expected in Eqn. 3.44. The peak load is also directly proportional to the cross-sectional area. The effect on pulse width is simply the opposite to that for the peak load, i.e. pulse width decreases with increase in elastic modulus and radius.

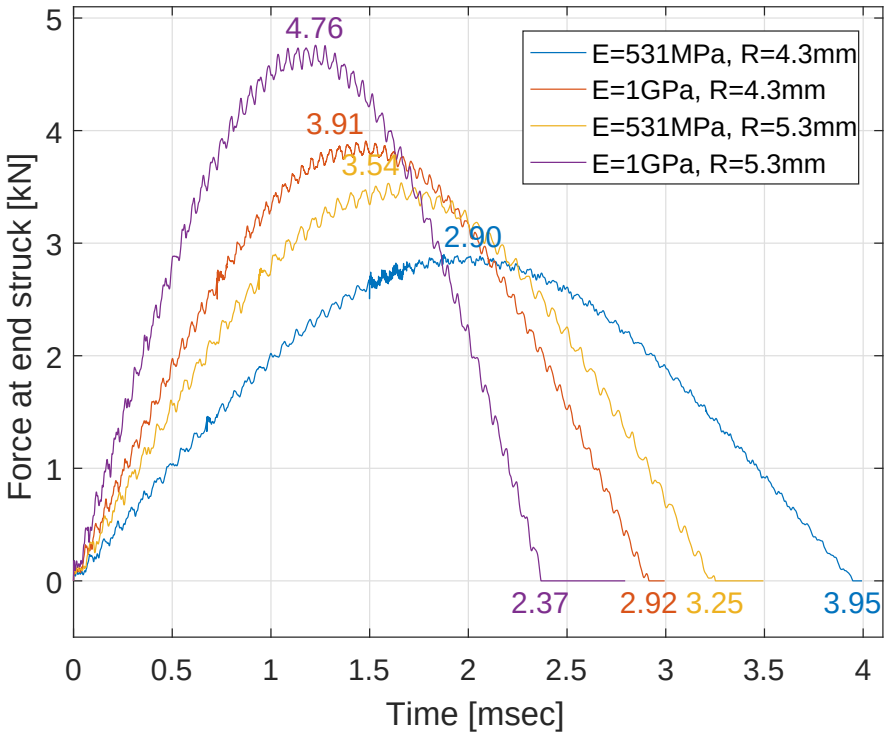

Figure 4.4: The effect of structural stiffness (elastic modulus, E and radius, R representing material and geometry components respectively) on the resulting force at end struck

4.6 Fourier transform returning the frequency of travelling wave

Transformation of time-to-frequency domain signal (Fourier transform) results were shown for the closed-form solutions, e.g. Fig. 3.7b. The method is discussed in greater detail in this Section. Three FE models are employed in this study, namely original light-hammer mass (M: 26.6 gram), half of the mass (M/2) and five-times of the mass (5M); all models are defined with zero Poisson's ratio. In addition, closed-form (CF) solution is included for which mass M is employed for 'original' and 'Hanning-windowed signals'. The input details for these five models are shown in Table 4.2.

The objective in this transformation into frequency domain is to determine the frequency of stress wave propagation inside one full pulse duration via Fast Fourier transform (FFT) in MATLAB. The method is employed with two additional techniques, namely multiplication with 'Hanning' function and introduction of 'zero-padding' in which the additional data is introduced beyond the original simulation time. The details of these techniques are discussed in the following section.

Table 4.2: FE and CF models evaluating FFT method; Units: Length [mm], mass [g], modulus [MPa]

Method	Model	Mass of hammer	Dimension		E	ρ	ν
			d	L			
FE	M	26.6					
	M/2	13.3					
	5M	133.0	10.6	12	100	1.31×10^{-3}	0
CF	Original	26.6					
	Hanning						

4.6.1 Methodology

In order to improve the frequency analysis, Hanning function is applied to the original signal, followed by zero-padding, which implies addition of zeros following the data available. The Hanning function is expressed as

$$w(n) = 0.5\Big[1 - \cos\big(2\pi\frac{n}{N}\big)\Big]; \quad 0 \leq n \leq N, \tag{4.7}$$

where window length, $L = N + 1$ and n is the sample number. The application of Hanning function implies time-wise multiplication of the signal being transformed by the function expressed in Eqn. 4.7. In addition, the purpose of zero-padding is to create smooth mainlobe(s) at detected frequency with sidelobes surrounding it. If zero-padding is not applied, then the frequencies are represented by spikes which are not helpful in identifying significant frequency(s). The Hanning window is applied to minimise the magnitude of sidelobes in order to enhance the visual detection of mainlobe(s). This time-domain signal transformation is known as 'convulation' which has effect in frequency domain after a discrete Fourier transformation is performed.

As mentioned in Table 4.2, three (3) force histories at the end struck obtained from FE analysis are considered and depending on the hammer mass, the windowed FFT results are presented either normally, i.e. $0 < \mathrm{f} < f_{\mathrm{n}}$ or mirrored/shifted, i.e. $-f_{\mathrm{n}}/2 < \mathrm{f} < f_{\mathrm{n}}/2$, where f_{n} is the highest returned frequency. In addition, the ordinate axis is also presented in the decibel (dB) scale which is either power-based ($20\log_{10}$) or magnitude-based ($10\log_{10}$) which are normalised to the maximum of transformed magnitude in the logarithmic scale.

4.6.2 Windowed pulses

It is observed in Fig. 4.5 that the variation in the hammer's mass affects the peak force response and pulse width of the impacted bar as well as the number of intervals, which has been previously discussed in the parametric analysis. As a recall, higher hammer's mass results in higher peak load being achieved with longer pulse duration. The number of intervals also increases when the bar is subjected to heavier hammer.

The original pulse is transformed into windowed version of signal by applying Hanning window as shown in Fig. 4.5 for models of M, M/2 and 5M. Hanning is chosen after rough test compared to another popular function, called 'Hamming' which both give identical result, at least in term of the detected frequency which is the sole output under investigation.

The application of Hanning window causes reduction in the original pulse magnitudes except in the middle of pulse where magnitudes almost match up. It is understood by the definition of Hanning function itself which is a symmetrical bell-like curve starting from zero to unity halfway the duration as expressed in Eqn. 4.7. The number of intervals in the Hanned pulse in Fig. 4.5 can still be roughly observed and are comparable to those in the original signal, even though now the signal becomes smoother after been windowed.

The size of zero-padding here is ten-times the length of the original pulse, in order to increase the number of samples from the signal to return more accurate frequency value at the point of interest. However, introduction of zero-padding is known to produce sidelobes around the bell-like mainlobe(s) at the analysed frequency which might interfere with the analysis and detection of mainlobes as will be shown shortly. Thus, by multiplying Hanning function to the original signal, the effect and magnitude of sidelobes are substantially reduced. As per

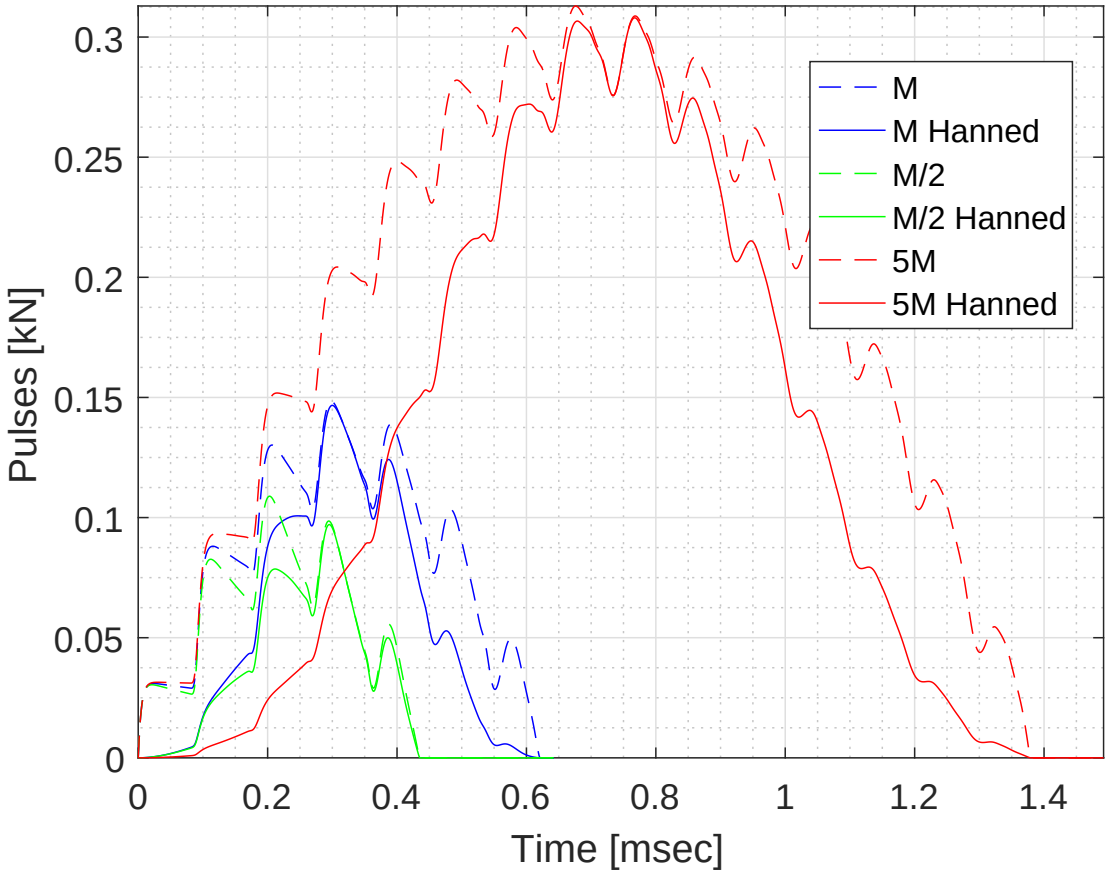

Figure 4.5: Original and Hanned pulses (without zero-padding)

discussion, both the Hanning function and zero-padding technique are required conjointly to increase the accuracy of frequency prediction, such as practiced by Jensen et al. (2014).

4.6.3 Normal and shifted transformations

Transformed signal from time-domain to frequency domain for the model with mass M/2 is shown in Fig. 4.6, which shows normal transformation (Fig. 4.6a) or shifted to be zero-centered (Fig. 4.6b) including the mirrored negative frequency range, in which the highest peak magnitude is recorded at the zero frequency. The zoom-in boxes show relevant range of frequency near to zero. Local peaks are highlighted in red, which indicate the most significant frequency (apart from $f = 0$) is around $10 - 11$ kHz.

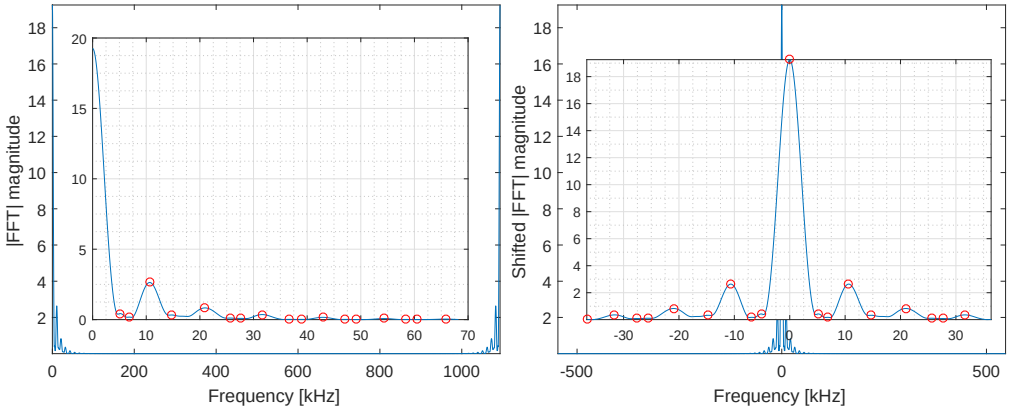

(a) Normal transformation **(b)** Shifted or zero-centered

Figure 4.6: FFT Magnitudes: M/2 model

The Fourier transformation returns complex data, consisting real and imaginary parts at every bin, i.e. $a + bi$ depending on the sample size, L. The magnitude values are calculated as absolute of these complex data, while the frequency of these magnitudes depends on the bin number it presents and sampling frequency of the signal. Often, the magnitude of transformed signal is divided by the

sampling frequency and an arbitrary number (according to general rule), however this is not practiced in this study in order to present the data in its original form.

4.6.4 Decibel (dB)-based transformations

Alternatively, the ordinate axis in the frequency analysis, e.g. Fig. 4.6, can also be presented in logarithmic scale. In order to elucidate this approach, the transformed signals are presented in two forms, namely magnitude-based decibel (dB) and power-based dB. The only substantial difference between them is the value of the latter is twice of the former, i.e.

$$\text{Power-dB} = 2 \times \text{Magnitude-dB} = 20\log_{10}\Big(\frac{\text{Magnitude}}{\text{Magnitude}_{\text{max}}}\Big) \tag{4.8}$$

for power-based, while the logarithmic value is the normalised magnitude from Fourier transformation against the maximum spectrum throughout the frequency range.

Figure 4.7 shows the decibel (dB) axis of spectrum for magnitude, where the transformed absolute complex numbers are normalised against the maximum value, which occurs at zero frequency consequently returning zero value at the above mentioned frequency. Similar to the magnitude display (Fig. 4.6), the graphs are symmetrical at both zero frequency and $f_{\text{n}}/2$. Local peaks are highlighted using red circles and it can be noted the location of highest peak is at $f_{\text{5M}} = 10.5279$ kHz, which represents the interval frequency of stress waves moving back-and-forth which can be observed from time to complete an interval in Fig. 4.5.

The spectrum in power-based dB scale is shown in Fig. 4.8 for the case of M model. The frequency of intervals in this case is analysed to be 10.6173 kHz. It can be compared to Figs. 4.6 (M/2), 4.7 (5M) and 4.8 (M); longer pulse duration and number of intervals in the pulse results in larger number of local peaks (or

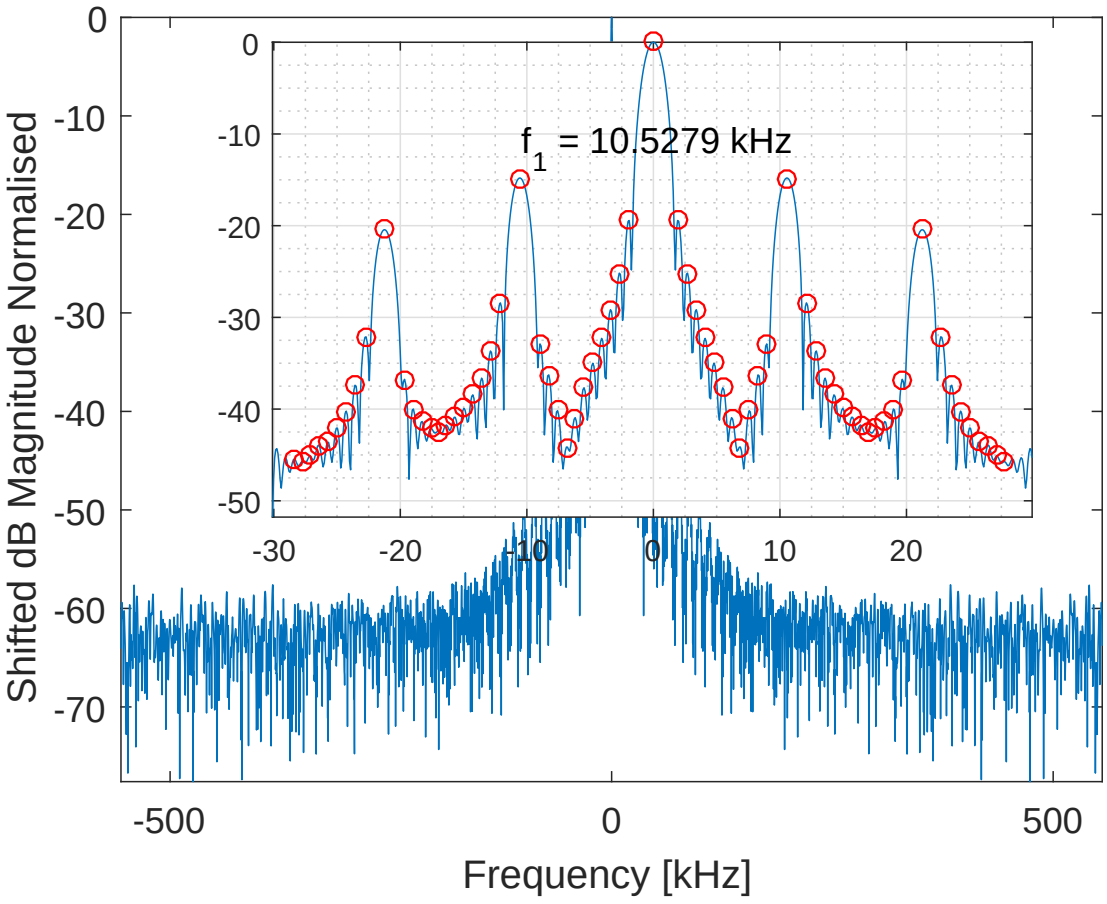

Figure 4.7: Shifted FFT dB Magnitudes of 5M model

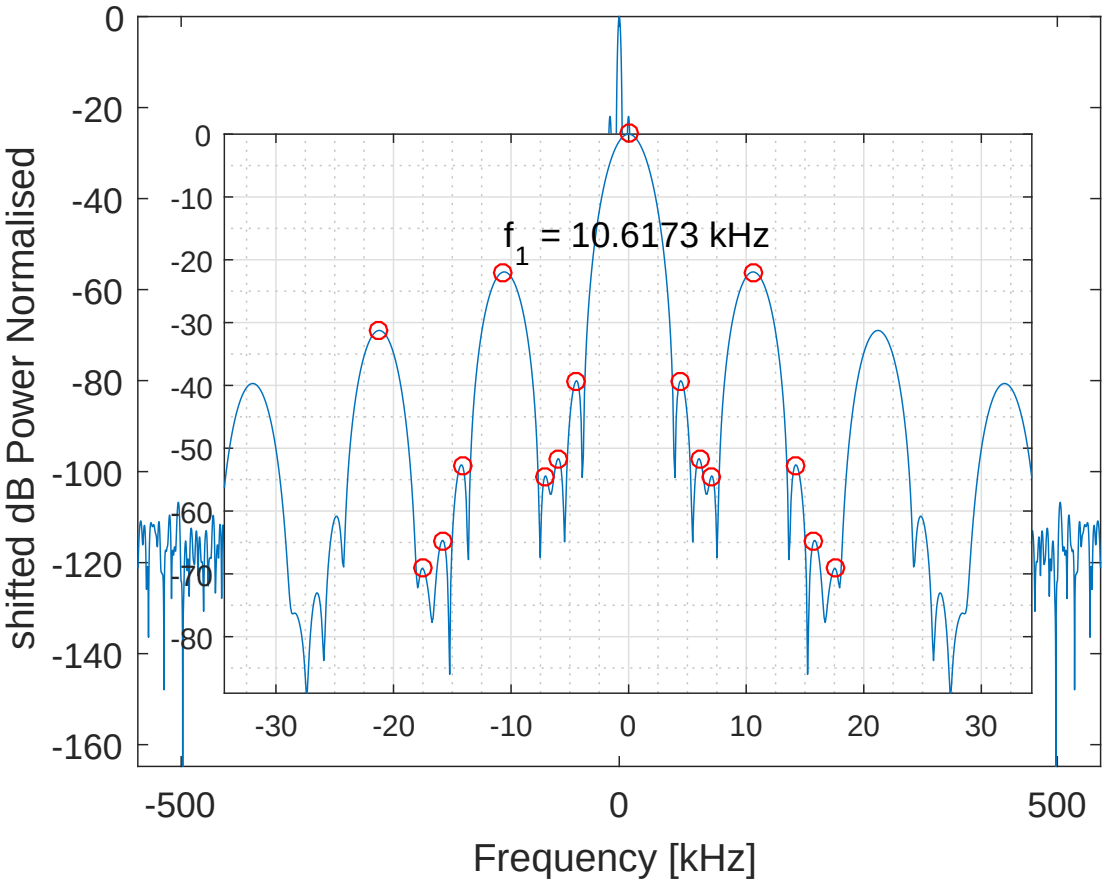

Figure 4.8: Zero-centered FFT dB Power of M model

sidelobes) within similar time frame, due to greater amount of zero-padded data being introduced into the signal.

Table 4.3: FE and CF interval frequency

Method	Model	Interval frequency [kHz]		% Diff.
		FFT	Theoretical (1D wave)	
FE	M/2	10.6164	11.5121	7.78
	M	10.6173		7.77
	5M	10.5279		8.55
CF	Original	11.4792		0.29
	Hann	11.4980		0.12

The interval frequencies for all three FE cases are tabulated in Table 4.3 in the FFT column. It can be observed that they are quite consistent between 10.5 to 10.6 kHz. However, based on 1-dimensional continuum wave theory, the frequency should be 11.51 kHz, which is calculated from

$$f_{\text{theory}} = \frac{1}{2l\sqrt{\rho}}\sqrt{E}. \tag{4.9}$$

One dimensional wave in continuum is used because Poisson's ratio in this study is set to be zero, which effectively defines the system to be one-dimensional. The interval frequency of stress wave is measured as inverse of twice of travelling time because the interval in the pulse is expected to show the duration for wave to travel back-and-forth inside the bar.

The discrepancies between 7.7-to-8.5% for FE models are not insignificant. There might be a possibility that the interval frequency returned by LS-DYNA simulation package does not exactly follow the continuum wave propagation theory. Thus, it is worth checking the frequency of the closed-form (CF) solution

using FFT method to ensure the discrepancy is only a numerical issue in the LS-DYNA explicit code.

4.6.5 FFT on closed form (CF) solutions

The frequency analysis is done on two-types of closed-form (CF) signals, i.e. original and Hanned (Table 4.2). The hammer mass used in this section is 26.6 gram, which is equivalent to the FE case of M model. The difference between signals is illustrated in Fig. 4.9. Note that in the original pulse (Fig. 4.9a), the signal reaches negative value after 0.58 msec, whereas in the windowed signal records approximately zero values (extremely small negative) during the same duration (Fig. 4.9b). This comparison is made to ensure that the discrepancy in the previous FE models is not because of recorded zero pulse before the end of contact duration. In this closed-form solution, the final interval (7^{th} interval) has only effectively around 4/9 of the last time interval in which the system is in contact, as the negative value of force indicates the end of contact duration.

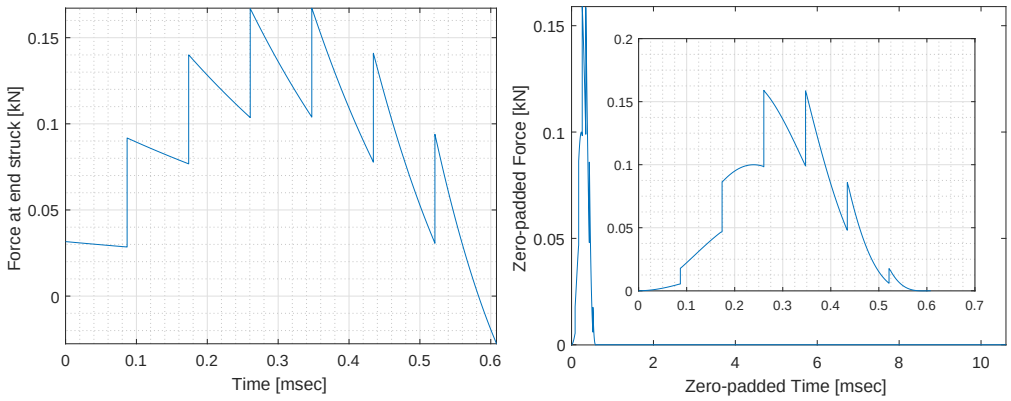

(a) Original signal **(b)** Windowed signal

Figure 4.9: Closed-form signals

The dB scale power transform for both CF signals of Fig. 4.9 is shown in Fig. 4.10. Note that the zero-centered transformation is employed in this case. It can be seen in the transformation from original signal (Fig. 4.10a) that the peaks spike

quite suddenly, as compared to the transformed signal where windowing and zero-padding are introduced (Fig. 4.10b). The signals in frequency domain become smooth mainlobes when windowed, with the existence of a couple of sidelobes between them. Three sidelobes are observed showing local peaks between $f = 0$ and the expected interval frequency of $f = 11.48$ kHz. As mentioned above, the introduction of zero-padding causes the signal in frequency domain to contain more datapoints, while the Hanning window assists in reducing the magnitude of sidelobes for better visualisation of mainlobes. The response of transformed windowed signal in Fig. 4.10b is quite similar with the one obtained via the FE method (Fig. 4.8).

Comparison between interval frequency values obtained by FFT with the theory is shown in Table 4.3, clearly showing the frequencies in CF are very close to their predicted value (errors of 0.1 to 0.3%). The most logical explanation regarding relatively significant discrepancy of the previous FE results in Section 4.6.4 may be attributed to the numerical inaccuracies introduced by the explicit code of LS-DYNA, and not due to the FFT approach using MATLAB.

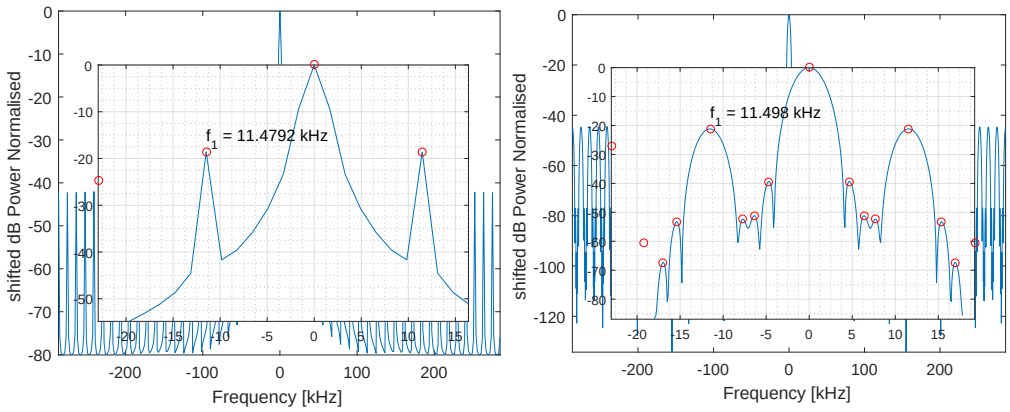

(a) Original **(b)** Windowed

Figure 4.10: FFT dB Power CF

4.7 Impact response of models with time-dependent material behaviour

This section analyses the effect of employing a time-dependent material model, viz. viscoelasticity (VE) in comparison to simple time-independent linear elastic model (TI-E) assigned to the impacted axisymmetric bar. In VE, the relaxation modulus can be defined using the Prony series (Park and Schapery, 1999) as

$$E(t) = E_{\text{eqm}} + \sum_{i=1}^{n} E_i e^{-\frac{t}{\rho_i}}, \tag{4.10}$$

where E_{eqm} is the equilibrium modulus and E_i and ρ_i are the relaxation strengths and relaxation times respectively. Manda et al. (2016) showed that a three-term Prony series ($n = 3$) adequately represents the relaxation modulus of trabecular bone with different volume fractions, BV/TV. The values determined in this above cited study are used to consider the influence of time-dependent material properties on impact response.

4.7.1 Implementing viscoelasticity in LS-DYNA

In time-independent elastic material model (abbreviated as TI-E), the single value of elastic modulus, E is taken as $E(\infty)$ or E_{eqm} from Eqn. 4.10, a long-term modulus representing the material resistance value when the load stabilises hence treated as in statically-applied manner in equilibrium. On the other hand, the viscoelastic material model in LS-DYNA, e.g. Mat076: General Viscoelastic requires elastic bulk modulus, K. Similar to the equilibrium modulus in TI-E, K in VE is defined as a long-term modulus

$$K_{\text{eqm}} = \frac{E_{\text{eqm}}}{3(1-2\nu)}. \tag{4.11}$$

The Poisson's ratio was defined as 0.33 and all subsequent analyses in this Thesis are conducted with this value. In order to exhibit relaxation phase in the VE model, shear relaxation moduli, G_i and decay constants, β_i for each term in Prony series are required. Hence, the general expression of the Prony series in LS-DYNA is

$$g(t) = \sum_{i=1}^{n} G_i e^{-\beta_i t}. \tag{4.12}$$

Comparing these two relaxation expressions in Eqns. 4.10 and 4.12, the relaxation strengths and times parameters in the former provided by Manda et al. (2016) need to be converted onto shear moduli and decay constants in the former respectively. Isotropic shear moduli are obtained from E and ν expressed as

$$G_i = \frac{E_i}{2(1+\nu)}, \tag{4.13}$$

while the decay constants (β_i) are simply inverse of the relaxation times (ρ_i) in which $i = 1, 2, 3$ for three terms of Prony series. In the case of three-term Prony series, the General Viscoelastic material model requires four input terms, in which the extra term is G_{eqm} with zero decay constant, fully expressed as

$$g(t) = G_{\text{eqm}} + G_1 e^{-\beta_1 t} + G_2 e^{-\beta_2 t} + G_3 e^{-\beta_3 t}. \tag{4.14}$$

Six (6) bone volume fraction models, i.e. BV/TV=19, 26, 33, 39, 43 and 43% are selectively chosen from Manda et al. (2016) on the basis of signifying direct correlation between material's stiffness and the reported BV/TV. The required input parameters are given in Table 4.4 by using conversions expressed in Eqns. 4.11, 4.13 and 4.14. All these conversions are applicable in this study assuming the material as having isotropic behaviour.

Table 4.4: Parameters of time-independent elastic (TI-E) and viscoelastic (VE) material models; Units: modulus [MPa], decay constant [ksec^{-1}]

BV/TV [%]	TI-E	VE adopting Prony series				
	E_{eqm}	K_{eqm}	G_{eqm}	i	G_i	β_i
				1	5.34	684.93
0.19	250.43	417.38	89.44	2	3.27	42.39
				3	5.90	3.75
				1	7.80	1111.11
0.26	317.18	528.63	113.28	2	5.55	119.76
				3	6.61	8.22
				1	12.18	1086.96
0.33	498.53	830.88	178.05	2	6.51	125.47
				3	6.83	10.24
				1	15.17	1351.35
0.39	545.65	909.42	194.88	2	10.55	129.03
				3	11.99	6.76
				1	16.32	3030.30
0.42	572.05	953.42	204.30	2	10.74	184.84
				3	10.66	9.10
				1	24.34	1010.10
0.43	904.68	1507.80	323.10	2	12.40	109.53
				3	19.95	7.15

4.7.2 Force response

The bar in this Section is discretised into the 4-noded axisymmetric 10×40 solid elements impacted by 2.5 kg rigid impactor. The length of the bar is 21 mm and its diameter is 10.6 mm. The impactor was assigned with axial velocity of 0.99 m/s, which is equivalent when it is dropped from 50 mm height (Table 3.4). In order to terminate the simulation, the pulse duration is estimated as

$$t_{\text{pulse}} \approx \frac{1}{r}\sqrt{\frac{m_{\text{impactor}}\pi l}{E}}, \tag{4.15}$$

then the termination time was set to be slightly longer than the estimated pulse width in Eqn. 4.15.

Two main outputs are investigated from the resulting force response at the end struck of axisymmetric bar, namely the peak load as the highest magnitude of compressive load experienced by the end struck and the pulse width, which is the contact duration of the impact incidence. Figure 4.11 shows graphical elastic and viscoelastic responses of three different BV/TVs, clearly depicts that viscoelastic models have a stiffer response than their TI-E counterparts.

The key numerical results for all models are tabulated in Table 4.5 with $E(t)$ represents E_{eqm} and $E(0)$ for TI-E and VE respectively. The modulus function $E(t)$ represents well the contribution of BV/TV to bone sample's stiffness for both material models. In addition, the stiffness of VE models, which is $E(0)$ is consistently higher than TI-E (E_{eqm}).

Based on the peak load values in Table 4.5, the corresponding maximum compressive stresses at end struck fall in the range of $19.3 \leq \sigma_{\max} \leq 38.1$ MPa as simulated by FE method which has similar configuration to the experimental set up in the next Chapter. Morgan and Keaveny (2001) loaded trabecular bone

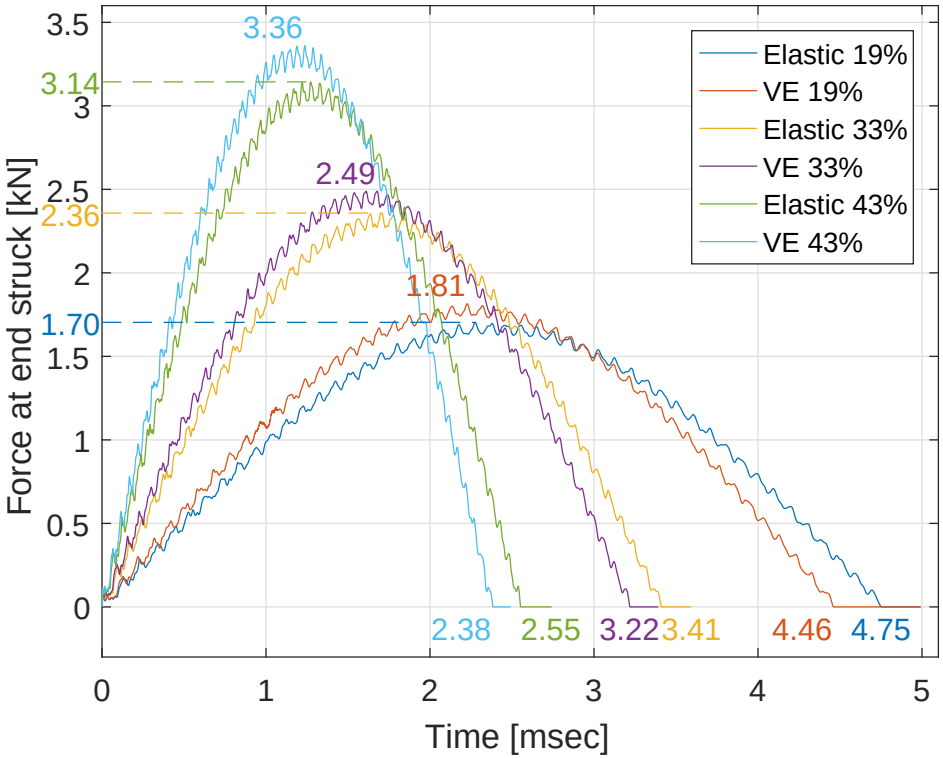

Figure 4.11: Effect of varying time-independent and viscoelastic properties towards peak load and pulse width

Table 4.5: Elastic modulus input of time-independent elastic (TI-E) and viscoelastic (VE) material properties with the corresponding peak load (F_{max}) and pulse width (t_{pulse})

BV/TV	Model	$E(t)$	Peak load		Pulse width	
		[MPa]	Value [kN]	% diff.	Value [msec]	% diff.
19%	TI-E	250.4	1.7037	**6.53**	4.7549	**6.14**
	VE	291.1	1.8150		4.4629	
26%	TI-E	317.2	1.9036	**7.31**	4.2455	**6.75**
	VE	373.1	2.0428		3.9591	
33%	TI-E	498.5	2.3580	**5.55**	3.4111	**5.57**
	VE	570.0	2.4889		3.2212	
39%	TI-E	545.7	2.4641	**7.39**	3.2646	**7.16**
	VE	651.2	2.6461		3.0310	
42%	TI-E	572.1	2.5223	**7.34**	3.1919	**6.71**
	VE	677.7	2.7074		2.9777	
43%	TI-E	904.7	3.1434	**6.94**	2.5544	**6.67**
	VE	1063.4	3.3615		2.3839	

samples from femoral neck by means of extensometer producing yield strength of 17.45 ± 6.15 MPa. Another range of strength was reported by Shim et al. (2005) for trabecular bone from cervical spine to be roughly around 5-20 MPa, which were subjected to dynamic test by means of split Hopkinson pressure bar (SHPB) set to $10^2 - 10^3$/sec of strain rate. Based on these two ranges, the current numerically-simulated maximum compressive stresses for low BV/TV, e.g. BV/TV=19% ($\sigma_{\max} = 19.3$ MPa); fall around the maximum reported range of yield strength, while in the case of higher BV/TV they appear to be beyond the reported strength in the cited literature. Nonetheless, it remains to be seen in this Chapter whether actual bovine trabecular bones can withstand the simulated magnitudes of compressive stress in this impulsive work; the relevant results will be presented and discussed in the following experimental Chapter.

Another output is interval frequency of the stress wave travelling back-and-forth the bar's length which is obtained by Fourier transformations. Some results are shown in Fig. 4.12a and 4.12b for TI-E and VE models respectively. VE models exhibit higher frequency compared to their less stiff TI-E counterpart which is consistent with the observation on its shorter interval time in Fig. 4.11.

The frequencies are compared with the theoretical values, calculated from Eqn. 4.9 where $E(t)$ values assigned to each model are tabulated in Table 4.5, i.e. $E(t) = E(0)$ for VE models. Table 4.6 shows increasing difference with theoretical frequencies as the elastic modulus becomes higher. In other words, the difference between evaluated frequency by FFT with its theoretical value is proportional to the modulus value. The study indicates that the impact response of a viscoelastic trabecular bone can be estimated by undertaking a time-independent analysis using $E(0)$ in place of the static modulus.

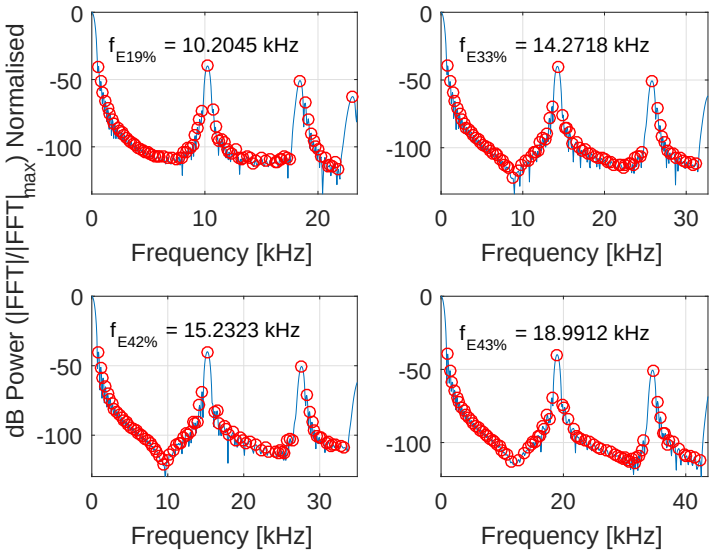

(a) by varying time-independent properties

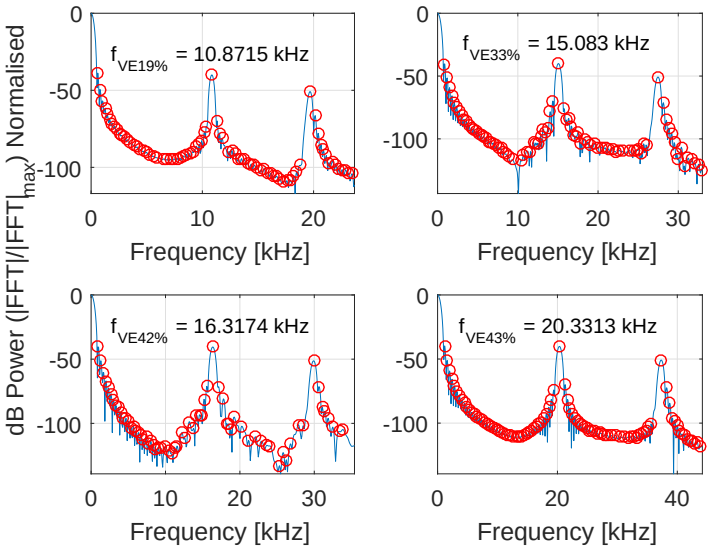

(b) by varying viscoelastic properties

Figure 4.12: Effect on interval frequency

Table 4.6: Frequency of TI-E and VE simulations returned by Fourier transform against theoretical value

BV/TV	Model	Interval frequency [kHz]		
		Fourier transform	Theoretical	% diff.
0.19	TI-E	10.2045	10.4102	1.98
	VE	10.8715	11.2237	3.14
0.26	TI-E	11.4639	11.7157	2.15
	VE	12.2915	12.7066	3.27
0.33	TI-E	14.2718	14.6879	2.83
	VE	15.0830	15.7055	3.96
0.39	TI-E	14.8580	15.3664	3.31
	VE	15.9789	16.7870	4.81
0.42	TI-E	15.2323	15.7337	3.19
	VE	16.3174	17.1251	4.72
0.43	TI-E	18.9912	19.7862	4.02
	VE	20.3313	21.4518	5.22

4.7.3 Modulus-to-output variable relations

The parametric study on elastic modulus in Sections 3.5.3 and 4.5.2 points to the requirement of using linear direct best fit regression for relating $\sqrt{E}$ to the peak load and interval frequency, i.e. $F_{\max} \propto \sqrt{E}$ and $f \propto \sqrt{E}$ respectively. On the other hand, its effect to the pulse width is mathematically defined with inverse proportionality relation or negative power law, i.e. $t_{\text{pulse}} \propto 1/\sqrt{E}$. Note that the relations derived in this Section are only applicable to the current specific system configuration, such that 2.5 kg impactor hitting a bar of 10.6 mm diameter and 21 mm length dimensions from 50 mm drop height with the defined material properties as in Table 4.4.

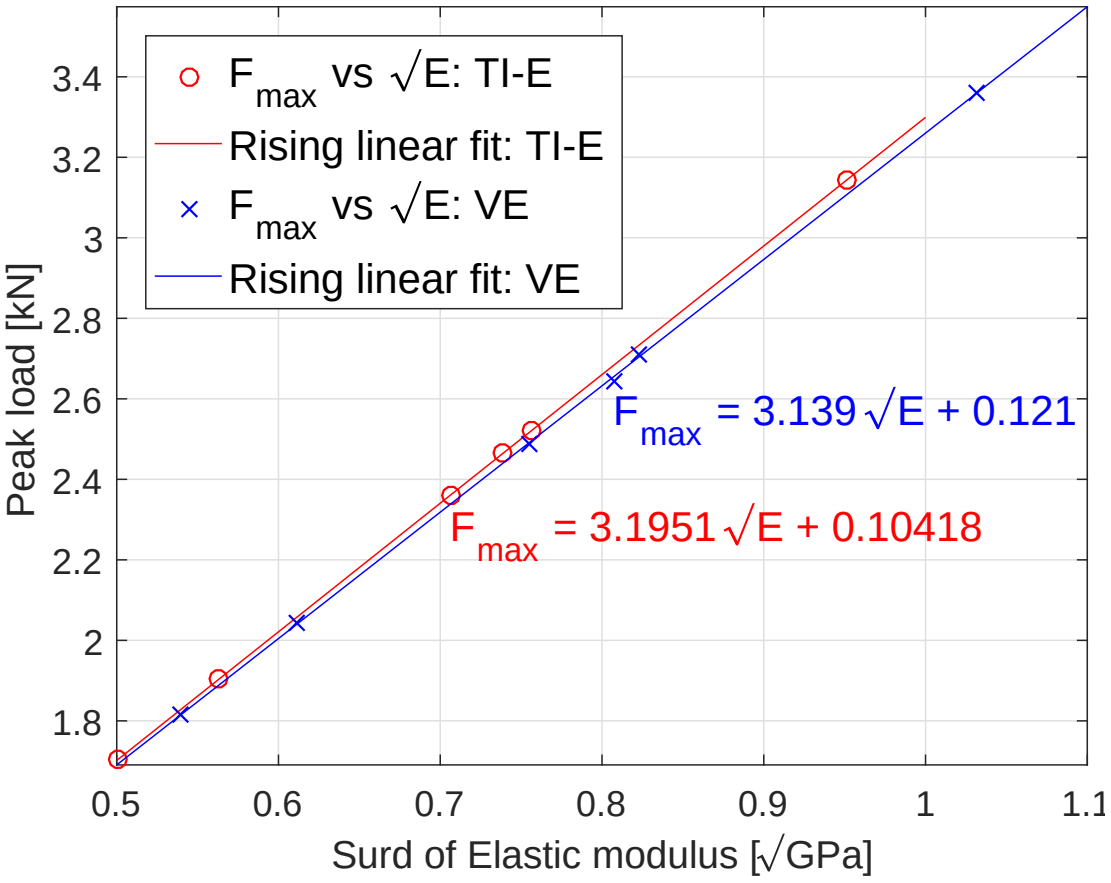

Figure 4.13: Peak load relation with elastic modulus for varying material properties

Figure 4.13 shows the linear relation between $\sqrt{E}$ and peak load, with the

equations obtained as

$$F_{\max} = 3.195\sqrt{E} + 0.104 \quad [\text{kN}] \tag{4.16}$$

and

$$F_{\max} = 3.139\sqrt{E} + 0.121 \quad [\text{kN}] \tag{4.17}$$

for TI-E and VE respectively. The current numerical solution provides the non-zero ordinate-intercepts as shown in Eqns. 4.16 and 4.17 indicating slight discrepancy by this method as opposed to zero intercept solved in the closed-form solution, e.g. in Eqn. 3.44.

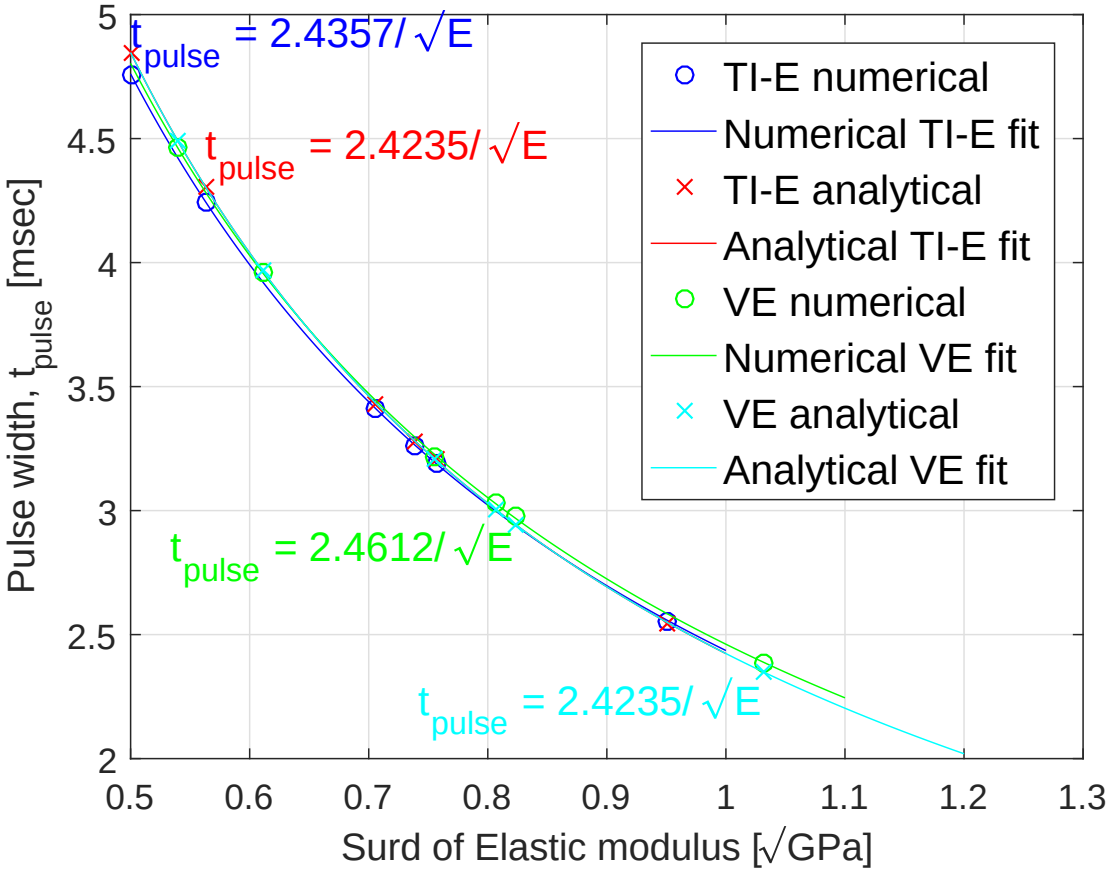

Figure 4.14: Pulse width relation with elastic modulus for varying material properties

Inverse proportion of pulse width is shown in Fig. 4.14 for four different methods,

i.e. numerical and analytical TI-E and VE models. The analytical solution is solved by the estimator of contact duration given in Eqn. 4.15, which is similar for both material models, expressed as

$$t_{\text{pulse}} = \frac{2.4235}{\sqrt{E}} \quad [\text{msec}], \tag{4.18}$$

with obviously zero residuals. The power law indices for numerical simulation data are very close to negative unity, though not exact, e.g. -0.97 for TI-E numerical fit. Their coefficients are slightly higher than the prediction in Eqn. 4.18, even though the residuals are still small, signifying good proposed power law regressions.

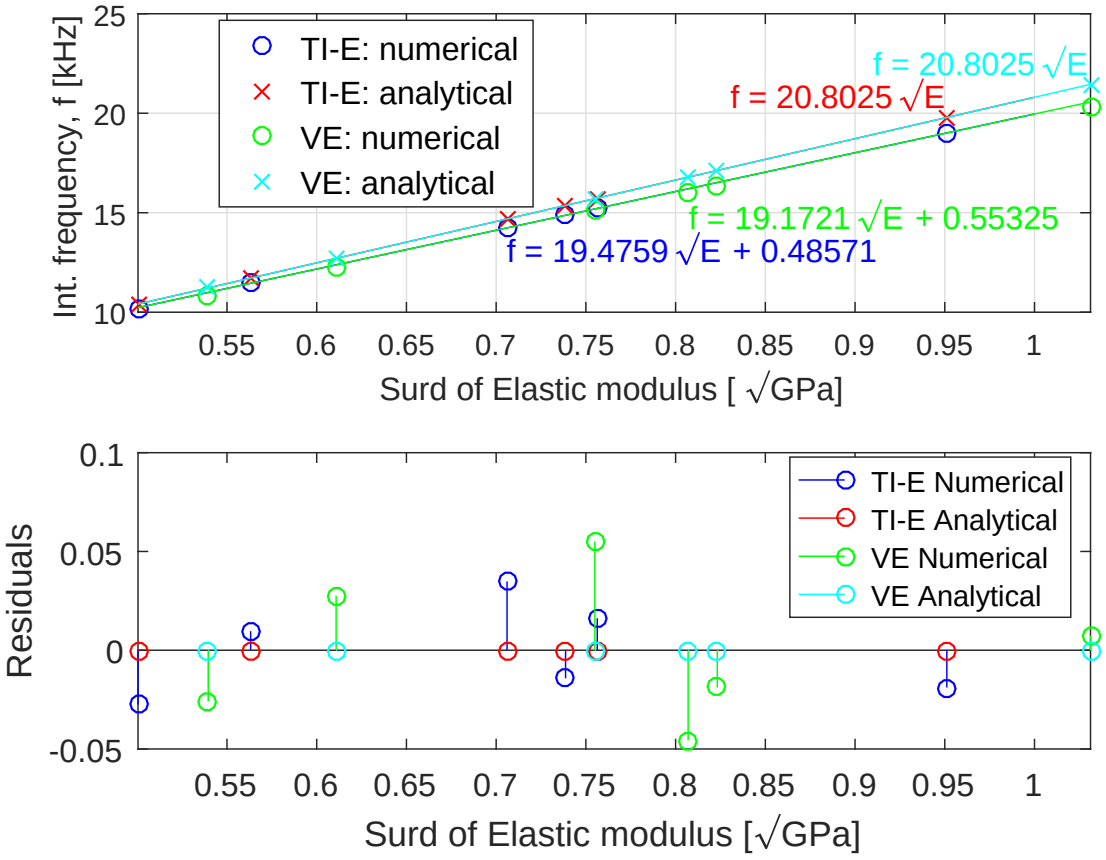

Figure 4.15: Interval frequency relation with elastic modulus for varying material properties

Finally, the linear model is fitted into interval frequency and square-root of modulus data obtained from both methods, i.e. numerical simulation via Fourier transform and theoretical governing equation as shown in Fig. 4.15. The theoretical frequency relation is expressed as

$$f = 20.8025\sqrt{E} \quad [\text{kHz}], \tag{4.19}$$

while the full straight line equations for returned Fourier transform data are

$$f = 19.4759\sqrt{E} + 0.4857 \quad [\text{kHz}] \tag{4.20}$$

and

$$f = 19.1721\sqrt{E} + 0.5533 \quad [\text{kHz}] \tag{4.21}$$

for TI-E and VE respectively.

The regressions in Eqns. 4.20 and 4.21 show the intercepts, i.e. $f(0)$ in the Fourier transform fitted data are substantial, while theoretically the value should be zero (see Eqn. 4.19). These intercepts highlight the numerical error presented by the Fourier transform's returned frequency data. The error here is mainly due to the numerical calculation of FE method as proved and discussed in Section 4.6.5; and not because of the FFT method.

4.7.4 Concluding remarks on elasticity

Time-dependent VE model is defined by its relaxation modulus governed by decaying exponential function as expressed by Eqn. 4.14. In impulsive response, the decaying effect is not apparent in the short period of loading time, nonetheless higher initial stiffness is introduced in comparison to the long-term modulus, i.e. $E(0) > E_{\text{eqm}}$. Hence, TI-E and VE material models can be represented by

E_{eqm} and $E(0)$ respectively and the viscoelastic material is treated as a time-independent material with higher elasticity.

The resulting maximum compressive stresses are in the range of 19-38 MPa, falls in the upper limit of reported yield strength of trabecular bone tested in dynamic compression mode: see Morgan and Keaveny (2001); Shim et al. (2005). Achievability of these stress values will be tested experimentally in the next Chapter as the cited literature suggest the current values predicted by FE analysis are beyond the yield strength of the trabecular bone.

In the elastic modulus-output variable relations, the square-root of elastic modulus, $\sqrt{E}$, exhibits direct linear proportionality with peak load and the resulting wave interval frequency, see Eqns. 4.17 and 4.21 while establishing inverse relation with pulse width as shown in Eqn. 4.18. These findings are consistent with the previous parametric study on elastic modulus in the closed-form solution (Section 3.5.3) and FE analysis on structural stiffness (Section 4.5.2).

Chapter 5

Impact tests on cancellous bone

5.1 Introduction

This Chapter describes the experimental set up of impact tests performed on bovine trabecular bone samples. The primary aim is to determine the impact properties of bone. In addition, the FE models are developed to replicate the experimental response for certain groups of samples.

The objective for the work in this Chapter includes investigation of varying responses of trabecular bone samples to impact loads with different bone volume ratios, BV/TV, and sample characteristics, e.g. existence of growth plate. The measured response is the time-varying force measured at the impacted and restrained surfaces of the samples. The key outputs of response under investigation are the measured peak load ($F_{\max}$) and pulse width (t_{pulse}), as well as the rising force gradient, i.e. loading rate ($\dot{F}$).

5.2 Experimental methods

The experimental procedure includes multiple steps starting with bone harvesting and storing, followed by preparing the samples (Section 5.2.1) to be tested. The samples are then scanned using micro-computer tomography (μCT) for evaluating the microstructural characteristics of the samples (Section 5.2.2). The geometry and mass of each specimen is recorded. The bones and samples were stored at -20 °C before being utilised for testing which was conducted at room temperature. The process of harvesting to testing of the bovine trabecular bone samples is summarised in Fig. 5.1.

5.2.1 Sample preparation

Bovine femoral bones, under 30 months old, were obtained from a local butcher which required no ethical approval. They were stored below the freezing point, i.e. at -20 °C prior to subsequent preparations. Femoral heads and greater trochanters were dissected by using a hacksaw after the bones were fully thawed in the normalising process at room temperature.

Figure 5.2a shows two proximal parts of bovine femurs that were sectioned: femoral head (BFH) and greater trochanter (BGT), to extract trabecular bone samples in their approximate principal direction, i.e. it was assumed that the principal trabecular alignment is in this direction as shown in Fig. 5.2b.

Trabecular bone samples ($n = 31$) were then extracted from two femoral heads and greater trochanters in a hydrated condition, as a means to mitigate against temperature damage by using a 10.7 mm inner diameter diamond-coated coring tool (Starlite, Rosemont USA). The obtained samples were cut parallel at edges by using a low-speed saw (Buehler, Germany), producing cylindrical shape specimens, with the average diameter of 10.76 ± 0.08 mm and mean length of

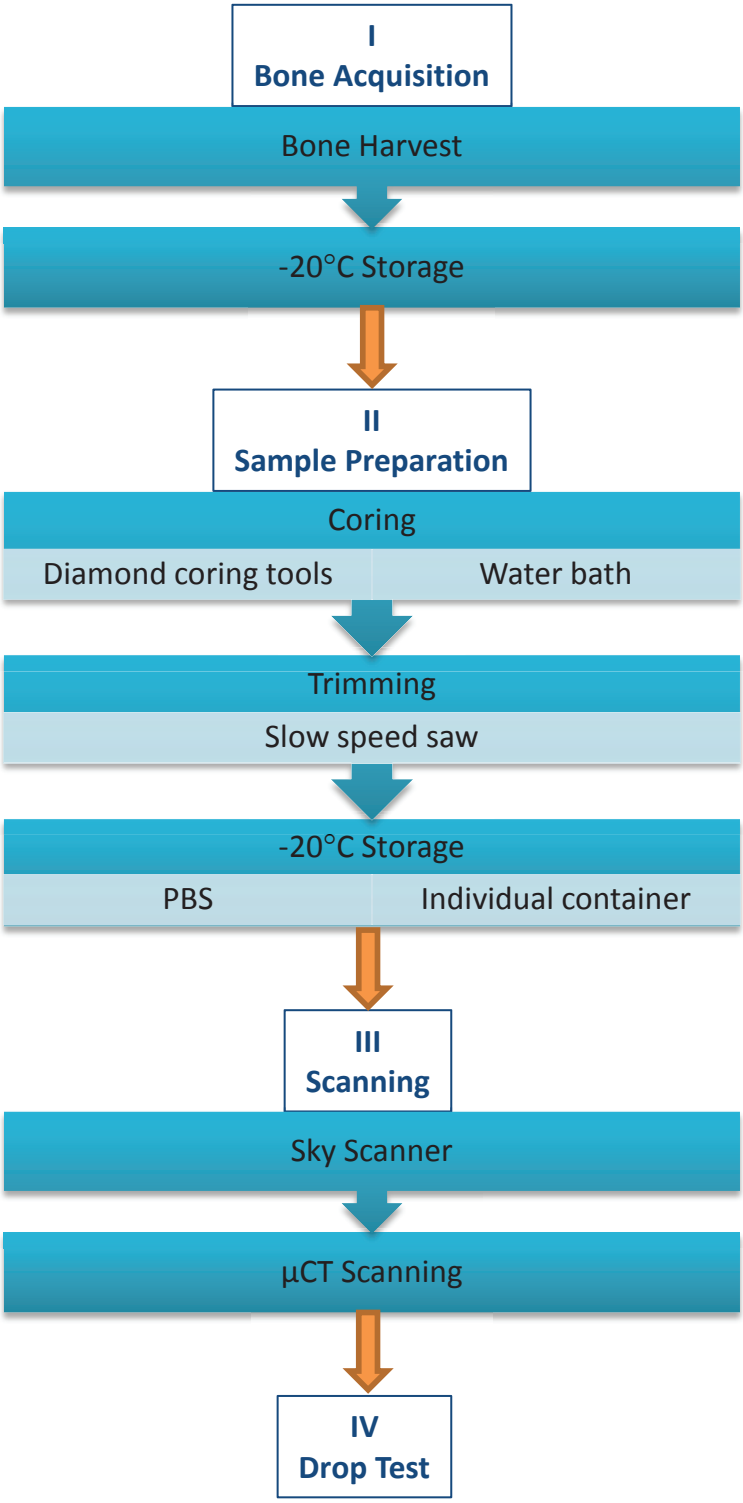

Figure 5.1: Flowchart on the experimental procedure

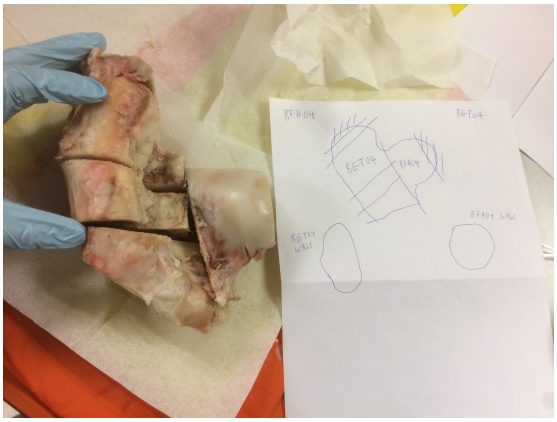

(a) Into femoral head (BFH) and greater trochanter (BGT) parts

(b) Cross-sectional view of trabecular alignment (human specimen) as a reference

Figure 5.2: Sectioning proximal femur

21.90 ± 0.67 mm as tabulated in Table 5.1. With respect to their diameters, all measurements were precise as the average measured value is between 10.7-10.8 mm. With regards to their length, the values were between 21.23 and 22.47 mm; the trimming process was intended to give 21 mm length samples. Each specimen was placed in its individual epoxy tube filled with phosphate-buffered saline (PBS) to keep it hydrated then stored at -20 °C until the mechanical testing was conducted.

Table 5.1: Dimensions of samples; BFH refers to femoral head, while BGT refers to greater trochanter

Part	Sample	Diameter [mm]				Length [mm]			
		D_1	D_2	D_3	D_{ave}	L_1	L_2	L_3	L_{ave}
BFH04	s1	10.75	10.76	10.75	10.75	21.81	21.64	21.47	21.64
	s2	10.75	10.71	10.79	10.75	22.09	22.02	21.99	22.03
	s3	10.78	10.83	10.72	10.78	21.58	21.54	21.57	21.56
	s4	10.77	10.72	10.73	10.74	21.95	21.85	21.85	21.88

Continued on next page

Table 5.1 – continued from previous page

Part	Sample	Diameter [mm]				Length [mm]			
		D_1	D_2	D_3	D_{ave}	L_1	L_2	L_3	L_{ave}
	s5	10.77	10.71	10.72	10.73	22.01	22.03	22.01	22.02
	s6	10.69	10.74	10.79	10.74	21.95	21.89	21.91	21.92
	s7	10.76	10.77	10.76	10.76	22.03	22.06	21.97	22.02
BFH05	s1	10.78	10.79	10.79	10.79	21.99	21.99	22.07	22.02
	s2	10.71	10.76	10.78	10.75	21.91	21.93	21.87	21.90
	s3	10.80	10.77	10.68	10.75	22.03	21.79	21.96	21.93
	s4	10.77	10.76	10.74	10.76	22.04	22.25	22.20	22.16
	s5	10.85	10.84	10.83	10.84	22.08	22.12	22.07	22.09
	s6	10.78	10.73	10.73	10.75	21.44	21.34	21.34	21.37
	s7	10.75	10.72	10.74	10.74	21.90	22.01	22.10	22.00
BGT04	s1	10.76	10.66	10.68	10.70	21.52	21.54	21.51	21.52
	s2	10.80	10.80	10.64	10.75	22.45	22.41	21.42	22.43
	s3	10.77	10.66	10.80	10.74	21.83	21.82	21.77	21.81
	s4	10.74	10.77	10.80	10.77	22.03	22.00	22.04	22.02
	s5	10.74	10.66	10.74	10.71	20.58	21.54	21.56	21.23
	s6	10.74	10.69	10.66	10.70	22.43	22.47	22.40	22.43
	s7	10.75	10.73	10.66	10.71	20.62	20.62	20.61	20.62
	s8	10.75	10.74	10.66	10.72	21.81	21.83	21.81	21.82
	s9	10.75	10.72	10.66	10.71	22.00	22.44	22.02	22.15
BGT05	s1	10.73	10.79	10.86	10.79	22.44	22.40	22.57	22.47
	s2	10.73	10.79	10.83	10.78	22.31	22.36	22.33	22.33
	s3	10.76	10.87	10.77	10.80	22.31	22.28	22.35	22.31
	s4	10.79	10.74	10.75	10.76	21.94	22.02	22.04	22.00
	s5	10.85	10.74	10.84	10.81	21.98	21.93	21.99	21.97
	s6	10.78	10.81	10.81	10.80	21.63	21.54	21.53	21.57

Continued on next page

Table 5.1 – continued from previous page

Part	Sample	Diameter [mm]				Length [mm]			
		D_1	D_2	D_3	D_{ave}	L_1	L_2	L_3	L_{ave}
	s7	10.81	10.83	10.78	10.81	21.84	21.86	21.89	21.86
	s8	10.89	10.78	10.74	10.80	21.84	21.89	21.92	21.89

The trabecular bone samples were prepared in cylindrical shape with length to diameter ratio of approximately 2:1. This ratio of cylindrical specimen geometry has been previously found to record lower standard errors of the modulus as well as strength estimation compared to the cube (Keaveny et al., 1993).

5.2.2 μCT scanning and image reconstruction

Prior to the drop tests, the prepared samples were subjected to μCT scanner with an image resolution of 17.22 μm using Skyscan 1172 (Bruker, Kontich, Belgium) to obtain the sliced scanned images. The scanning procedure utilised 54 kV and 185 μA voltage and current sources respectively, with additional parameters of 885 msec exposure and 0.5 mm aluminium filter between X-ray source and the specimen. The images were then reconstructed in NRecon programme (Version: 1.6.9.4, Bruker, Kontich, Belgium) with no further reduction in resolution; typical reconstructed images are shown in Fig. 5.3.

The reconstructed images in Figs. 5.3a and 5.3b show typical samples having high BV/TV. The latter has a growth plate (GP) in the upper region (seen as a diagonal line). In addition, Fig. 5.3b also illustrates inhomogeneity of bone volume ratio (BV/TV) along the sample, i.e. the bottom region appears to be relatively porous. Meanwhile, Fig.5.3c depicts a sample with an apparently low BV/TV, thus categorised as a porous sample. An example of cross-sectional scanned image for each reconstructed model is shown in Fig. 5.4, in which the

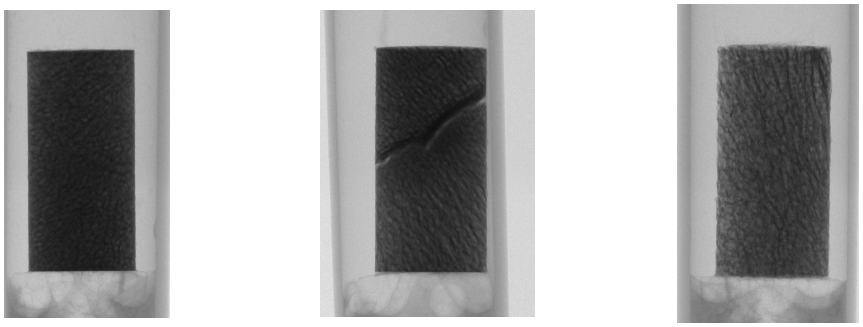

(a) High BV/TV **(b)** High BV/TV with GP **(c)** Low BV/TV

Figure 5.3: Reconstructed images of micro-CT scanned samples

level of porosity is clearly depicted, i.e. dense and porous samples are illustrated in Fig. 5.4a and 5.4c respectively. The presence of growth plate is shown in Fig. 5.4b for this dense sample.

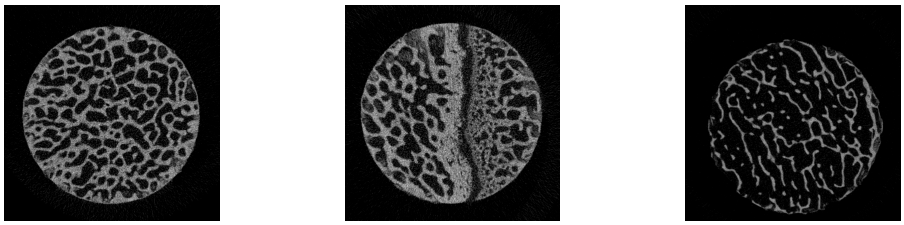

(a) High BV/TV **(b)** High BV/TV with GP **(c)** Low BV/TV

Figure 5.4: Example of cross-sectional scanned image of

A morphometric analysis was conducted on those reconstructed images by using CT Analyser software (CTAn, Version: 1.17.7.2, Bruker, Kontich, Belgium) to determine the samples' bone volume ratios. Considering all the specimens and the average values for each specimen, the bone volume fraction, BV/TV was found to be in the range of $10 - 53\%$ (mean $\pm$ SD: $25 \pm 14\%$) as shown in Table 5.2. Regional variations were also considered for all samples. Each sample was divided into top, middle and bottom regions and their BV/TVs are evaluated for each case. The results are included in Table 5.2. Bone volume fraction values for regions which had a growth plate were not evaluated, e.g. BFH04s1 sample. The table shows high BV/TV values for the samples extracted from the femoral

head, which range between 35.03-52.57 %, indicating that the samples can be considered to be dense. The samples from greater trochanter show BV/TV of 10.10-26.45 %, which are consistently lower than those from the femoral head. High BV/TV values (shown in blue in Table 5.2) would be expected to have a higher impact strength, while specimens with lower bone volume ratios or those with growth plates are likely to have lower strengths.

Table 5.2: Bone fractions [%] of samples at overall and certain regions; with calculated apparent density, ρ_{app} [$\times 10^{-6}$ kg/mm^3]

Part	Sample	Bone volume ratio, BV/TV				BV/TV	ρ_{app}
		Top	Middle	Bottom	**Ave**		
BFH04	s2	36.742	36.204	32.631	**35.19**	35.03	1.49
	s5	34.762	40.834	44.984	**40.19**	40.62	1.48
	s1	43.397	-	28.909	**36.15**	37.89	1.47
	s3	38.922	37.529	-	**38.23**	41.72	1.53
	s4	-	-	44.702	**44.70**	45.93	1.52
	s6	40.021	-	41.969	**41.00**	48.32	1.30
	s7	55.547	47.540	-	**51.54**	50.92	1.36
BFH05	s1	43.281	50.683	46.240	**46.73**	46.85	1.43
	s2	55.685	55.792	47.577	**53.02**	52.57	1.50
	s3	46.006	52.932	56.250	**51.73**	51.91	1.51
	s4	52.551	55.915	48.124	**52.20**	52.51	1.50
	s5	58.026	52.554	-	**55.29**	48.88	1.44
	s6	-	35.577	35.107	**35.34**	37.46	1.33
	s7	42.635	-	38.662	**40.65**	41.56	1.36
BGT04	s6	26.907	26.852	23.771	**25.84**	25.37	1.20
	s9	18.469	20.987	24.216	**21.22**	21.47	1.17
	s1	18.011	20.181	19.531	**19.24**	19.93	1.15

Continued on next page

Table 5.2 – continued from previous page

Part	Sample	Bone fraction, BV/TV [%]				BV/TV [%]	ρ_{app}
		Top	Middle	Bottom	**Ave**		
	s3	11.649	18.603	23.751	**18.00**	18.16	1.20
	s7	18.574	18.523	16.441	**17.85**	17.81	1.24
	s8	14.710	14.859	16.692	**15.42**	15.26	1.10
	s2	16.161	12.927	9.995	**13.03**	12.90	1.04
	s4	14.325	9.458	8.451	**10.74**	10.93	1.04
	s5	7.843	9.977	12.450	**10.09**	10.10	1.44
BGT05	s3	27.992	26.382	25.510	**26.63**	26.45	1.21
	s6	23.034	23.333	23.285	**23.22**	23.07	1.23
	s1	16.928	18.823	20.673	**18.81**	18.67	1.18
	s7	17.058	17.422	20.320	**18.27**	17.99	1.13
	s2	15.929	20.944	24.234	**20.37**	20.54	1.14
	s5	20.093	17.738	14.995	**17.61**	17.61	1.11
	s4	14.945	12.216	11.577	**12.91**	12.95	1.06
	s8	12.613	10.443	10.059	**11.04**	11.01	1.06

The apparent density of samples is measured following the definition by Johanson et al. (1993), where the wet mass is divided by the total sample volume. The wet mass, m_{wet} of a sample is obtained after subjecting it to a centrifugal loading at 8000 rpm for 15 minutes to remove excess liquid from the sample, then weighed in the air. Thus, the apparent density is given by

$$\rho_{app} = \frac{4 \times m_{wet}}{\pi D_{ave}^2 L_{ave}} \tag{5.1}$$

where the D_{ave} and L_{ave} are average sample diameter and length provided in Table 5.1. The samples from femoral head show consistently high apparent density ($1.30 \leq \rho_{app} \leq 1.53 \times 10^{-6}$ kg/mm^3), while the density of samples from greater

trochanter is consistently lower with exception of sample BGT04s5 which was found to be heavier, most probably due to an intermittent scaling error. The average of apparent density was 1.31×10^{-6} kg/mm^3 which was used in the previous analyses with the closed form solution, e.g. Section 3.5.3 and FE method, e.g. Section 4.5.2.

Degree of anisotropy (DoA) and average trabecular thickness (Tb.Th) were also determined for all samples and were found to fall in the range of $0.1613 - 2.7395$ and $161.3 - 240.4$ μm respectively. This micro-structure analysis excludes eight (8) samples from femoral heads with growth plates, as the morphometric results of them are deemed to be unrepresentative of their micro-structure.

5.2.3 Impact test configuration

Drop tests were conducted to investigate the response in the form of force experienced at the top and bottom of cancellous bone samples from 50 mm drop height. The samples were dynamically tested with the force sensors (ICP® 208C05) attached to the 2.5 kg falling impactor striking the specimen along its height to measure the impulsive force history recorded at the impacted surface at 32 kHz sampling frequency, while another force sensor measured the force response at the bottom as shown in Fig. 5.5.

The impactor comprised mainly double-layered cuboids, in which the lower part was wider to encompass the guide rails and top force sensor, while the upper part was designed to centralise most of the hammer's weight to the impacted area of the hammer. The total mass of the hammer was 2.5 kg, made of aluminium grade 6061-T6 to produce realistic dynamic load upon the impacted specimens. The drop tower had two guide rails which were used to mark the initial positions of both the lowest surface of the hammer and the top surface of the trabecular bone

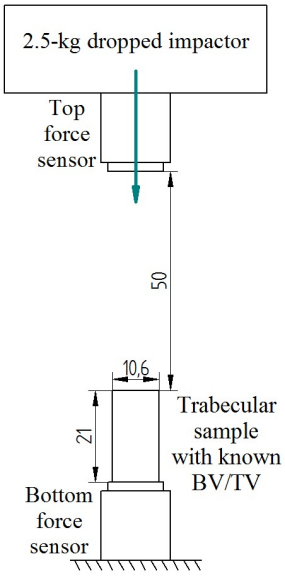

Figure 5.5: Schematic diagram of the drop test (not to scale); Dimensions shown in [mm].

sample. In addition, they prevent the hammer from rotating, ensuring orthogonal projection of impact on the end struck.

Some general rules were observed to obtain the best experimental orientation as advised in PCB Piezotronics (n.d.*a*). Among these, the impact loading needs to be 'central' as opposed to 'edge loading', which depends on the level of flatness of the cylindrical bottom end of the sample as well as the placement of the sample on top of the impact cap.

The initial velocity, v_0 was estimated from the drop height, h as $v_0 = \sqrt{2gh}$ (Eqn. 3.7), where g is acceleration due to gravity. This configuration is expected to produce an initial velocity of the hammer of 0.99 m/s before impact with kinetic energy of 1.226 Joule based on the principle of conservation of energy as discussed in Section 3.2.

As the guide rails were used to control the moving hammer, the supposedly

contacting surfaces between hammer's holes and guide rails are likely to generate friction, leading to a slight loss of energy. In order to minimise this factor, ball-bearings were used in between the hammer's holes and the rails.

Previous studies have shown that there is a slight energy loss in an actual drop test. Laing and Robinovitch (2010) conducted drop tests in which living humans were dropped from a 50 mm height on a force plate while recording the motion using 249 Hz, eight-camera motion measurement system detecting the reflective markers placed on several spots. In this experiment, the drops were achieved by releasing cables which held the subjects initially. The study found energy loss of 7.4%. In this study, it was assumed that the loss of energy is small. Therefore, the conservation of energy principle resulting in drop height-velocity relation of Eqn. 3.7 is considered to be sufficiently accurate.

5.2.4 Force data measurement

This Section describes how force measurement data was read from the force sensors, transferred into the data acquisition device, then finally read and written by the LabVIEW programme.

The force sensor (ICP® 208C05) is a piezo-sensor product of PCB Piezoelectrics, designed to measure the dynamic force response in the range of up to 5000 lb (22.24 kN) in compression. The device returns output in positive polarity for compression. The sensor has upper frequency limit of 36 kHz, which is equivalent to recording data at every 2.778×10^{-5} sec interval. More accurate measurement is obtained by following general rules and tips by PCB Piezotronics (PCB Piezotronics, n.d.*a*,n; Metz, 2007).

The quartz ICP® force sensors are more accurate than regular strain gauge load cells because they are designed with higher ringing frequency, i.e. 36 kHz. The inclusion of impact cap in the sensor's design enhances the accuracy of

measurement while protecting the sensor itself. The surface of impact cap is a convex and slightly curved to assist spreading the applied loads over the entire surface. In this study, a thin damping layer of a softer material is unnecessary since the contact is between metal impactor and the relatively less stiff trabecular bone sample (PCB Piezotronics, n.d.*a*).

The force sensors are connected onto PCB 442B104 signal conditioner as an intermediary device before the data acquisition (DAQ) card. The signal conditioner serves as an indicator for correct installation and signal's presence from the measuring sensors. Its red indicator for each channel lights up if there is no detected signal, mainly signalling either faulty sensor, broken wire or unconnected channel. Indicators were checked before any test was conducted. This device is then connected onto the data acquisition card, which is a built-in device of NI USB-6251 BNC which has maximum sampling rate of 1.25 MS/s for its 8-differential analogue inputs .

Laboratory Virtual Instrumentation Engineering Workbench (LabVIEW) is a visual programming language by National Instrument (NI) commonly used for the data acquisition. In order to acquire data from sensor(s), users are required to build a graphical block diagram which resembles a flow chart in LabVIEW's dataflow programming language, conveniently by creating three necessary components, namely front panel, block diagram and connector panel. These components represent LabVIEW subroutines, which are called virtual instruments (VIs). Two main tasks programmed into the VI are first to acquire the data read from the sensor, and then to write the measurement into a readable file format, e.g. text file.

The measured force signal following the drop test is written into a simple text editor with two columns of data, namely time history depending on the sampling frequency, as well as the force measured at each time history in voltage unit. The

voltage data is then converted according to the force sensor's sensitivity of 0.2277 V/kN as provided in the calibration certificate of ICP® 208C05 model. This data allows analysts to plot the force response at the end struck, then analyse important features of the pulse, i.e. peak load, pulse width, time to peak load, prolonged failure period and second peak load in failure region as will be presented and discussed in this Chapter.

5.3 General responses

There are two main responses from this experiment, namely the post-impact physical structure of the samples and the recorded forces at both ends, i.e. top and bottom surfaces. The former is useful for explaining the features obtained in the force data. In this Section, the force responses obtained from the drop test are presented; these comprise of multiple response pulses. Subsequent discussion (in the following Sections) focuses on the first pulse.

5.3.1 Post-test samples conditions

Typical conditions of samples from the femoral head and greater trochanter after the tests are shown in Fig. 5.6.

It is observed in Fig. 5.6a that some samples from femoral head have no apparent damage, e.g. BFH04s2, which is likely to have behaved elastically when dynamically tested. On the other hand, dense samples with growth plates were either fractured along the growth plate region, e.g. BFH04s4 or were partially damaged but still retained most of their original structure, e.g. BFH04s7. These damages occurred along the growth plate. All samples from trochanter (Fig. 5.6b) which have relatively low BV/TV failed, either by getting squashed at one end, e.g. BGT04s2 or excessively crushed, e.g. BGT04s8. This physical observation is important for analysing the obtained load response measured by the force sensors.

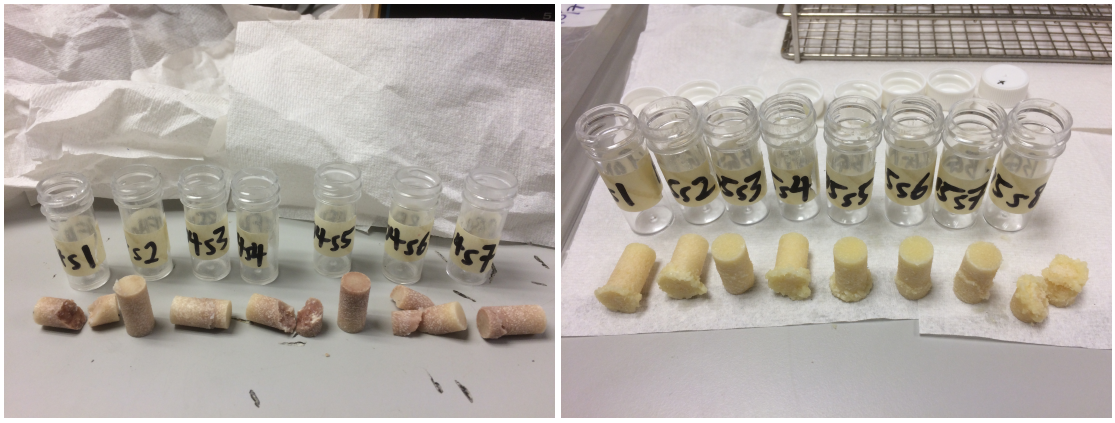

(a) from femoral head (BFH04) **(b)** from greater trochanter (BGT04)

Figure 5.6: Typical post-test sample conditions. The numbering was arranged in order from left to right

5.3.2 Overall pulses

The pattern of overall pulses depends on whether the impacted sample has been displaced away (Fig. 5.7) after the first impact or remained in position post-impact (Fig. 5.8) sandwiched between the two force sensors. The overall pulses consist of multiple impulses until the drop test process halts as shown in Figs. 5.7a and 5.8a. In the drop test, the hammer rebounds after striking the sample, then moves downwards again due to gravity for the subsequent strikes and this process continues until there is no gap between the impact caps of the two sensors. The measured force after the impulses have stopped is recorded to be around 24.5 N, corresponding to the weight of 2.5 kg hammer.

The key difference between overall pulses for the 'remained standing' and the 'displaced' samples is the second pulse reading in comparison to the first pulse. In the case of remained standing sample, the first pulse records the highest peak load (Fig. 5.8a); the presence of sample after the first strike produces lower subsequent pulses corresponding to sequentially lower drop heights after each strike on the same bone sample. On the other hand, if the sample was displaced after the first

strike, it causes the hammer to directly strike the base, hence the second pulse is higher than the first, even for some other subsequent impulses (Fig. 5.7a) due to stiff contact between metals, i.e. the impact caps of top and bottom force sensors.

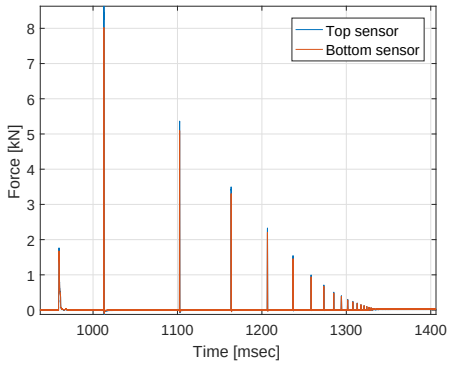

(a) in force responses

(b) physically

Figure 5.7: Response of displaced sample

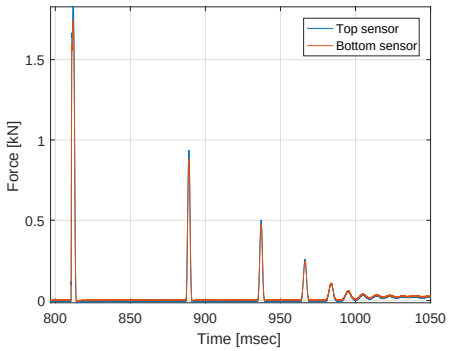

(a) in force responses

(b) physically

Figure 5.8: Response of remained standing sample

5.4 Response of samples with high BV/TV

From this Section onwards, the analysis of impacted trabecular bone focuses on the first pulse as it is not possible to estimate the velocity or energy imparted during subsequent impacts even for samples that remained standing. Samples were assumed to be dense when the bone volume fraction (BV/TV) exceeded 35%; these were all extracted from the femoral head. The dense samples were

extracted from two sources of bovine femurs (BFH04 and BFH05 in Table 5.2) and there were fourteen (14) samples in total.

5.4.1 General behaviour

The responses of impacted samples were categorised according to their physical condition after the test as well as their resulting force history at the two ends. In general, there are two main categories of mechanical responses, namely the elastic and inelastic responses. The elastic response of force history is expected to be comparable to the closed-form solution and elastic FE simulations. On the other hand, the existence of growth plate in some dense samples introduces weak region around the area and causes fracture to be developed along the growth plate. As a result, the obtained force history has elastic response only up to the failure load, then plasticity or damage dominates.

The responses for high BV/TV values (marked in blue in Table 5.2) are presented in Fig. 5.9. It is apparent that pulses recorded by both top and bottom sensors are almost identical. Therefore, only force responses measured at the top of the samples were considered. It can be seen from Fig. 5.9 that the force response of these high BV/TV samples is bell-shaped with a rise time almost similar to the fall time. This indicates that most of these samples remain largely elastic in the impact duration as the response resembles that obtained from the closed-form solution and elastic FE simulation. In many cases, the rise time is somewhat shorter than the fall time (particularly true for sample with BV/TV=35.03 %) indicating that the samples do encounter an inelastic regime. There are two main output parameters from the experimental pulses, namely the peak load ($F_{\max}$) and pulse width (t_{pulse}). Due to the limitation of sampling frequency of 32 kHz, the sensor is unable to capture the wave bouncing back-and-forth inside the sample, i.e. the measured force history does not present a jagged response, which could be used in the determination of frequency of travelling stress waves.

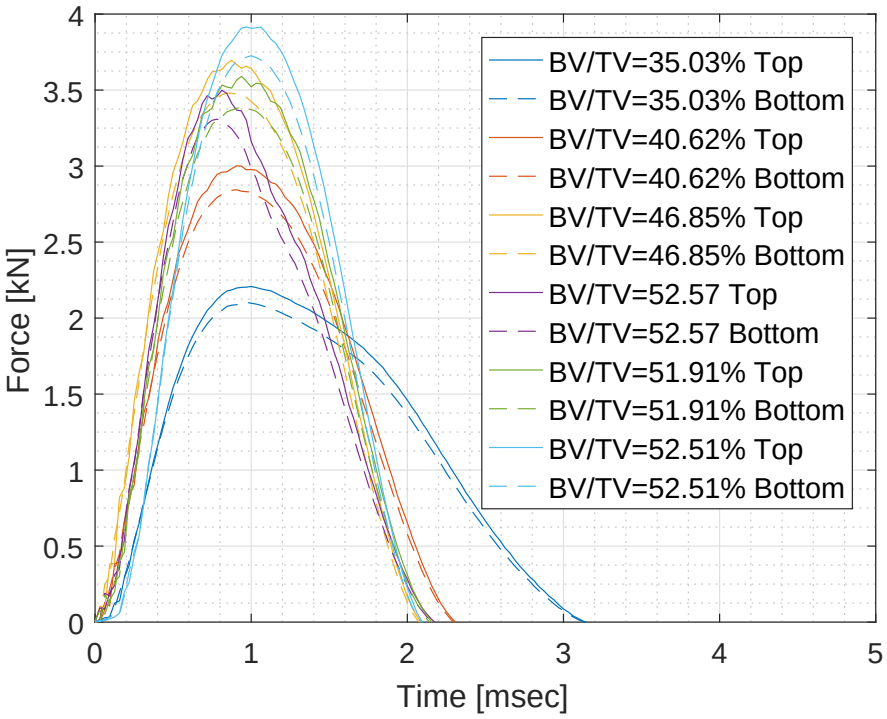

Figure 5.9: Forces measured at both ends in the elastically-responded dense samples from femoral head

In general, the force responses of Fig. 5.9 illustrate a stiffer response (higher forces and shorter pulse durations) for samples with higher BV/TV values. The ranges of peak force: 2.2-3.9 kN; and pulse width: 2.0-3.2 msec, in this Figure had been observed in both the closed-form solution and FE simulations based on typical properties of trabecular bone for this dynamic system (e.g. as in Figs. 3.7a and 4.4). However, those elastic moduli were defined on the basis of typical trabecular bones and were not specifically available for the tested samples.

The peak load values in Fig. 5.9 correspond to maximum compressive stresses of 24.3-43.0 MPa, assuming full elastic response was exhibited. In the last Chapter, the simulation of various BV/TV samples using TI-E and VE material models predicted the maximum stresses of 19.3-38.1 MPa (see Section 4.7.2). It is appropriate to claim the peak load-stress values observed in the current work support the achievability of the maximum stress simulated in the time-dependent data by Manda et al. (2016).

Assuming that these high BV/TV samples behave in an elastic manner, the $F_{\max} - \sqrt{E}$ and $t_{\text{pulse}} - \sqrt{E}$ relations derived from the closed-form solution (Eqns. 3.44 and 3.45) for these tests can be applied to the current experimental results because they share identical system definitions, i.e. the mass of impactor, drop height and sample's dimensions.

BV/TV is found to have a strong influence on the impact response: the peak response decreases and the pulse width increases with decrease in BV/TV values. This finding is consistent with the closed-form solution for impact on the elastic bodies, wherein higher sample stiffness results in higher peak and shorter pulse duration, e.g. Fig. 3.7a.

5.4.2 Deducing dynamic elastic modulus: Fitting

The bone samples under impact loading are expected to exhibit relatively higher elastic modulus in comparison to static modulus due to higher strain rate. Static tests undertaken in previous studies have shown that elastic modulus can be related to BV/TV with reasonable confidence. Here, the dynamic elastic modulus, E_{d} of the trabecular bone samples is considered as a function of its BV/TV. As has been discussed earlier, the peak load $F_{\max}$ is directly proportional to $\sqrt{E}$ for elastic material. Here, the $F_{\max}-$BV/TV is derived based on the data from Fig. 5.9.

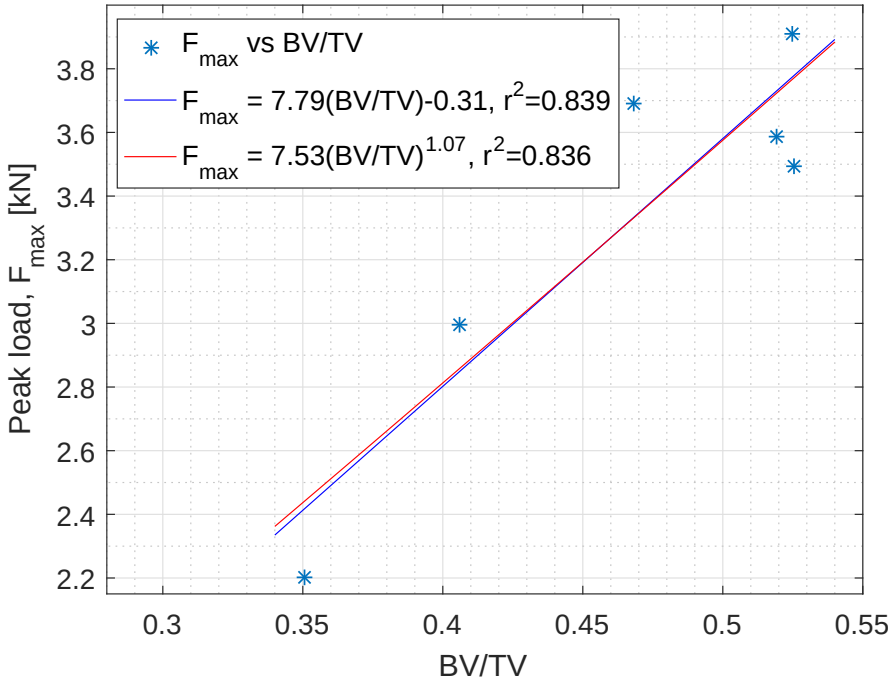

Figure 5.10: Linear and power law regressions for peak load-BV/TV relations

Two equations of best fit for $F_{\max}-$BV/TV are shown in Fig. 5.10; these are

$$F_{\max} = 7.79(\mathrm{BV/TV}) - 0.31 \quad [\mathrm{kN}] \tag{5.2}$$

and

$$F_{\max} = 7.53(\mathrm{BV/TV})^{1.07} \quad [\mathrm{kN}] \tag{5.3}$$

for linear and power law models respectively. Both equations appear to be very similar, approximately demonstrating a linear relationship (in both cases the exponent is almost unity). The coefficient of determination is also close to the values found in previous static studies, e.g. Goulet et al. (1994) with r^2=0.88.

Using $F_{\max}$ from Eqns. 5.3 in Eqn. 3.44 the dynamic elastic modulus can be expressed as

$$E_{\mathrm{d}} = 5.175(\mathrm{BV/TV})^{2.14} \quad [\mathrm{GPa}] \tag{5.4}$$

producing a power law relationship between elastic modulus and BV/TV. It should be noted that this relation holds as long as the sample remains elastic and it is not related to the configuration of test conducted, i.e. independent of the discussed parameters such as drop height and sample size.

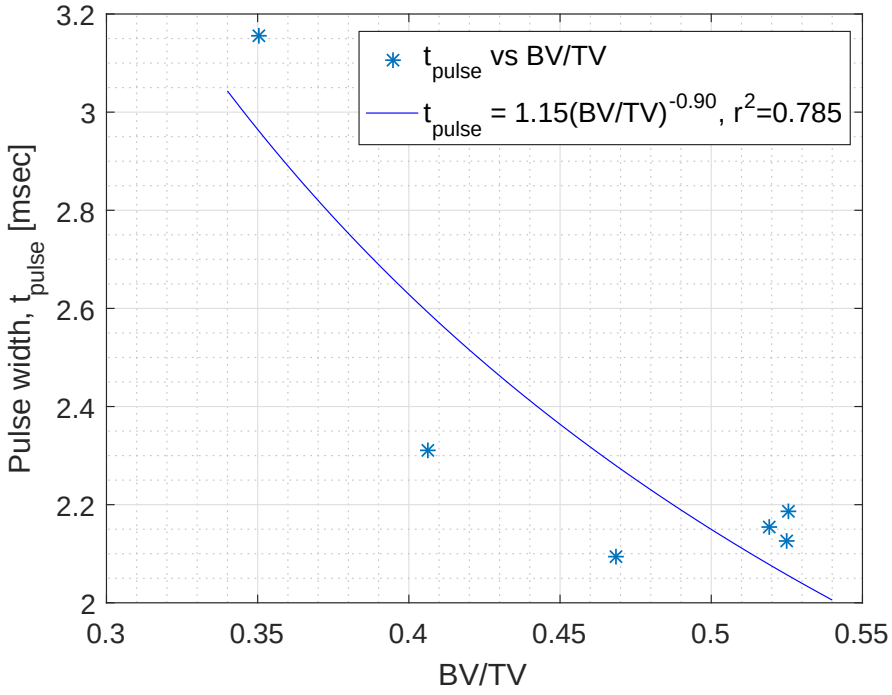

Figure 5.11: Power law regression for pulse width-BV/TV relation

Similar procedure was applied with the pulse width data to first obtain the power law regression as shown in Fig. 5.11. The inverse power law relation between t_{pulse} and BV/TV is expressed as

$$t_{\text{pulse}} = 1.15(\text{BV/TV})^{-0.90} \quad [\text{msec}], \tag{5.5}$$

where the negative exponent depicts the inverse correlation. Using Eqn. 5.5 in Eqn. 3.45 the dynamic elastic modulus can expressed as

$$E_{\text{d}} = 4.355(\text{BV/TV})^{1.8} \quad [\text{GPa}]. \tag{5.6}$$

Both Eqns. 5.4 and 5.6 are independent of test parameters and are derived based on the impacted samples with BV/TV in the range of $35.03 - 52.57\%$.

Comparing the two empirical dynamic elastic modulus expressions of Eqns. 5.4 and 5.6 based on the peak load and pulse width data respectively, the elastic modulus defined by the pulse width relation provides a slightly higher value. An analysis of this comparison is presented in the next Chapter together with static moduli found in the literature. These elastic modulus equations can be used to provide input to the closed-form and FE models for the corresponding sample-specific cases with known BV/TV values.

5.4.3 Deducing dynamic elastic modulus: Inverse modelling

The elastic (or assumed to be elastic) responses can also be analysed by applying inverse modelling technique, i.e. estimating the elastic modulus for a specific specimen and then comparing the experimental force response to the corresponding closed-form solution or FE simulation. Two most important aspects to be replicated in the experimental pulse response are the peak load and pulse width

for the analysis on elastic behaviour. However, it must be noted that the *in vitro* samples might have experienced some inelasticity during the impact, i.e. the response is not fully-elastic. While the closed-form solution is limited to elastic response, the FE simulations, with suitable post-elastic parameters, can incorporate the inelastic response as well. In this study, inelasticity was incorporated using von Mises elastoplasticity. It is recognised that bone has tension-compression asymmetry (Bayraktar and Keaveny, 2004; Levrero-Florencio et al., 2016; Xie, Wallace, Callanan and Pankaj, 2018) with regard to yield suggesting the use of pressure-sensitive yield criterion such as Drucker-Prager. However, in the experiments being conducted, the stresses experienced by the samples are primarily in the impact direction with negligible stresses developing in the radial direction. Consequently, the use of von Mises criterion is adequate. Perfect plasticity was assumed for elasto-plasticity in the first instance (subsequent sections consider other assumptions). Inverse modelling with elastoplasticity helps in predicting both the elastic as well as post-elastic properties. Thus, two FE models were developed for each sample, namely elastic and elasto-perfectly plastic models.

In the elasto-plastic model, the yield strength, σ_{Y} was assigned according to the maximum load measured experimentally, assuming that the peak load corresponded to yield stress.

For the elastic modulus, initial estimates were made using Eqns. 5.4 and 5.6 and these were then perturbed to obtain the best fit. The yield strength and the elastic moduli that provided the best fit are given in Table 5.3 along with the elastic moduli values evaluated from Eqns. 5.4 and 5.6. It can be seen that the empirical relations predict the E values reasonably well, in exception of samples with BV/TV=0.41 and 0.47 (errors of 60% and 37% respectively); the discrepancy between these data and the regression fit curve is also observed in Fig. 5.11. It is, clearly, important to recall that BV/TV is not the lone predictor of the mechanical behaviour which is governed by the micro-structure as well.

Table 5.3: FE models of high BV/TV samples utilising elasto-plastic parameters based on the experiment

BV/TV	Sample	σ_Y	E [GPa]		
[%]		[MPa]	Trial-and-error	Eqn. 5.4	Eqn. 5.6
35.03	BFH04s2	24.28	0.65	0.55	0.66
40.62	BFH04s5	33.15	1.20	0.75	0.86
46.85	BFH05s1	40.37	1.40	1.02	1.11
52.57	BFH05s2	38.51	1.32	1.31	1.37
51.91	BFH05s3	39.53	1.35	1.27	1.34
52.51	BFH05s4	43.02	1.40	1.30	1.37

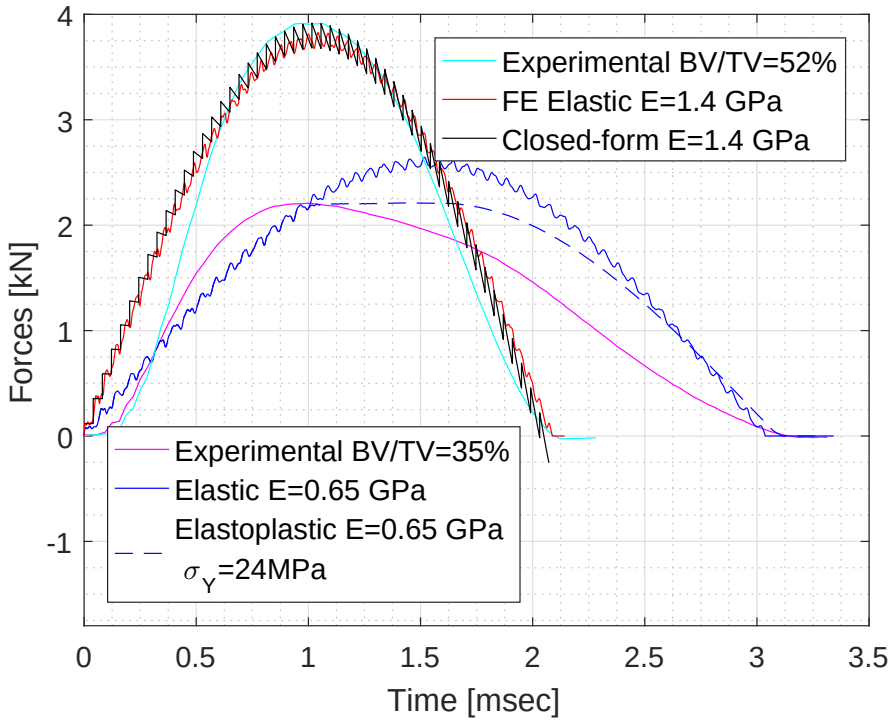

Figure 5.12: Inverse modelling to match peak load and pulse width of samples with BV/TV=35% and 52%

Figure 5.12 shows the experimental pulses of BV/TV = 35 and 52% with the corresponding FE and closed-form results with the specimen-specific elastic moduli, i.e. 0.65 GPa (lowest) and 1.4 GPa (highest) respectively. The models try to replicate the pulse width and peak load obtained from the experimental results. In the case of BV/TV=35%, the FE model suggests the sample is likely to have undergone some inelastic deformation prior to achieving the peak load, which the elasto-plastic model simulates reasonably well. The elasto-plastic model captures the peak response well but results in a flatter post-peak response, which is apparently due to the assumption of perfect plasticity.

On the other hand, very close resemblance is observed for BV/TV=52 % model, in which both peak load and pulse width values have good match when the elastic model is employed. The elastic simulation is verified using the closed-form solution, which is similar to that shown in Fig. 4.2.

5.4.4 Response of samples with growth plate

The high BV/TV samples with growth plate introducing weak region have an initially elastic and then inelastic deformation, which includes breakage as shown in Fig. 5.13. Simulating the behaviour of these inhomogeneous samples was considered beyond the scope of this study.

However, samples with comparable BV/TV, but without growth plate, were compared with those having growth plates in Fig. 5.14. It is observed that the pulse width of response while undergoing post-elastic deformation is higher than the elastic response, having an elongated duration in the failure region. The peak load for samples with growth plate is also lower than the peak load for samples without growth plate.

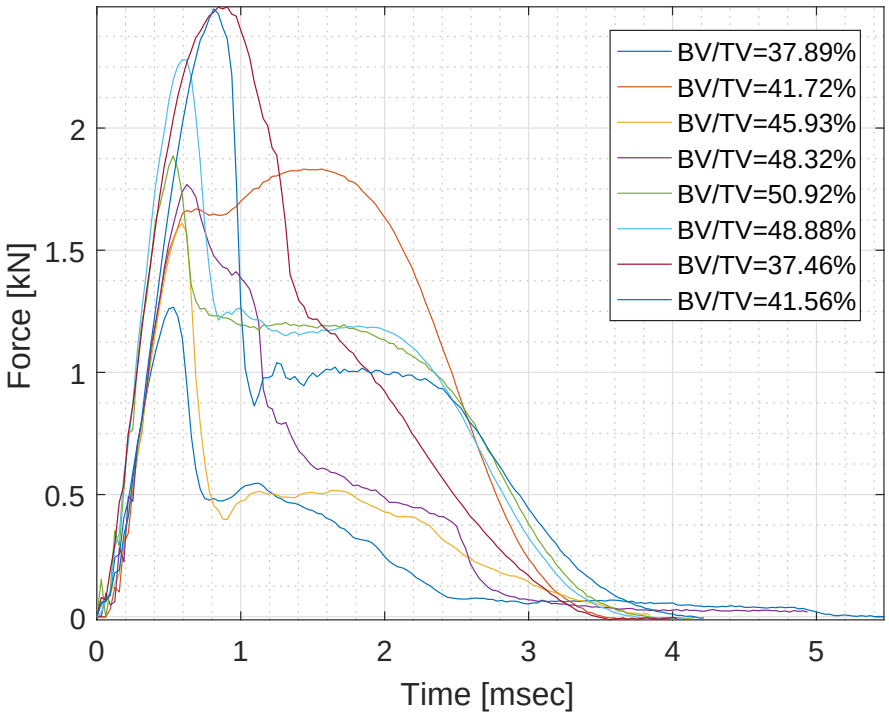

Figure 5.13: Force patterns measured at the top of high BV/TV samples with growth plate

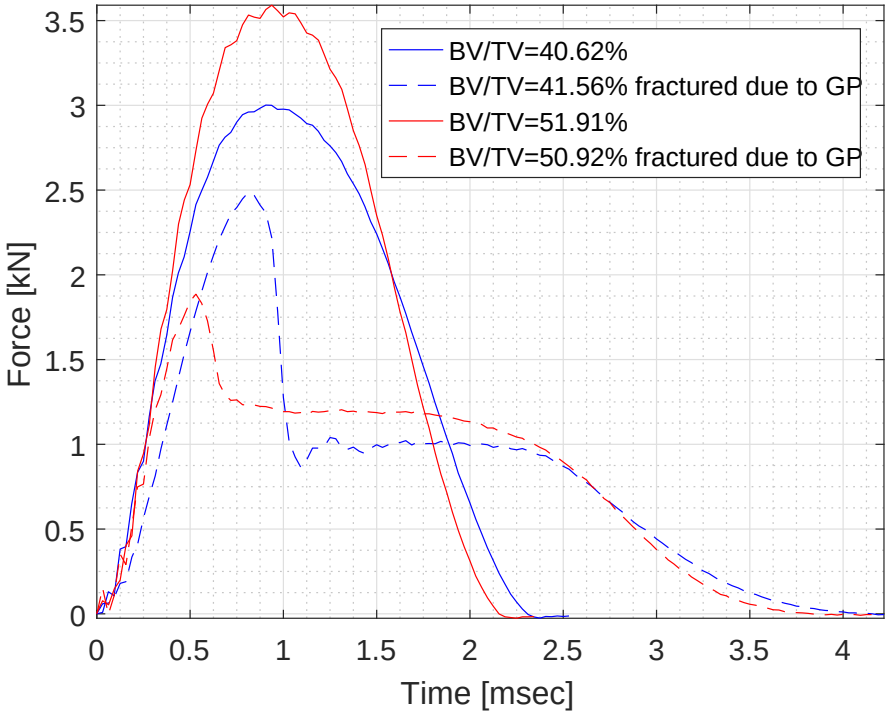

Figure 5.14: The effect of growth plate for samples with similar BV/TV

5.5 Response of samples with low BV/TV

The low BV/TV samples (without growth plates) were extracted from two sources of bovine trochanters; there are seventeen (17) samples in total. The samples were considered porous if the bone volume fraction (BV/TV) was below 27%. All tested samples were damaged while they remained standing between the two force sensors. The failure modes of these samples can be categorised into those that (a) have significant proportion of the sample height crushed or complete fracture or (b) where the failure is localised in a small region while the original shape is still discernible. Two types of failure mode (a) are depicted in Figs. 5.15a and 5.15b while mode (b) is typified by failure in Fig. 5.15c. In this Section, the analysis focuses on the post-peak response; the elastic region is discussed in the next section on the loading rate (Section 5.6).

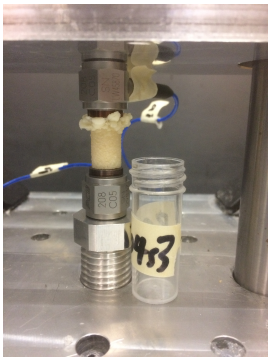

(a) significant crushing

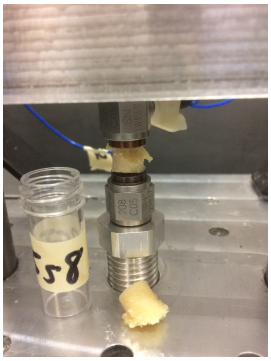

(b) complete fracture

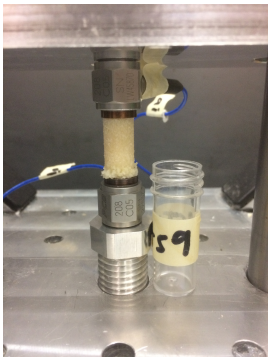

(c) localised failure in small region

Figure 5.15: Failure modes of low BV/TV samples

The load responses measured at the top of these porous samples are presented in Fig. 5.16 which are grouped according to the above mentioned categories: crushed and failed groups. Figure 5.16a shows the load responses from crushed samples have a generally undiscernable random looking pattern after the peak load is achieved at relatively low stress in comparison to the failed samples of

Fig. 5.16b, e.g. 3.7 MPa. In general, this group of samples have a low BV/TV, typically under 0.15. The random force pattern can be explained by physical post-test appearance of the samples -some of these were crushed along the height while others had relatively more localised crushing. For example, the sample with BV/TV=0.18 experienced crushing at the end struck only as shown in Fig. 5.15a. This phenomenon can be explained by referring to its high variation of regional BV/TVs as shown in Table 5.2, i.e. the value of bottom region is moderate (23.8%) while the top section which was damaged had only 11.6% BV/TV which was too porous.

On the other hand, the pulses of samples of Fig. 5.16b had a response pattern similar to the dense samples with growth plate in Fig. 5.13. Typical response pattern is shown in Fig. 5.17. The response comprised of an initial peak (denoted as F_{p}), followed by a drop to a finite non-zero value (F_{drop}) followed by yet another increase in the force value before it returns to zero. The prolonged inelastic response includes the second peak load ($F_{\mathrm{max,pl}}$) in that region. This study considered durations between the above mentioned forces viz. drop time (t_{drop}) and the prolonged plastic time (t_{pl}) between $F_{\mathrm{p}} - F_{\mathrm{drop}}$ and $F_{\mathrm{drop}} - F_{\mathrm{end}}$ respectively, in which F_{end} corresponds to the zero force at the end of impact. It also considered the forces F_{p}, F_{drop} and $F_{\mathrm{max,pl}}$ in the analysis for any empirical relationships. The pattern of Fig. 5.17 has not been discussed in previous studies.

5.5.1 Peak stress and load

The stress corresponding to the peak force was plotted against BV/TV as shown in Fig. 5.18. The stress values are then regressed against BV/TV by using linear and power law models as shown in Fig. 5.18. Poor relations are found for both linear and power law regressions, i.e. $r^2 = 0.207$ and 0.214 respectively, suggesting these two models poorly represent the scattered peak stress data.

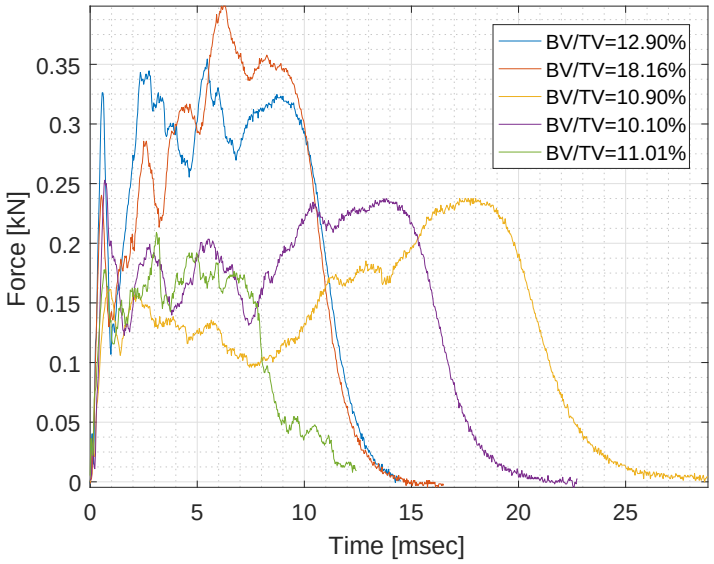

(a) which are crushed

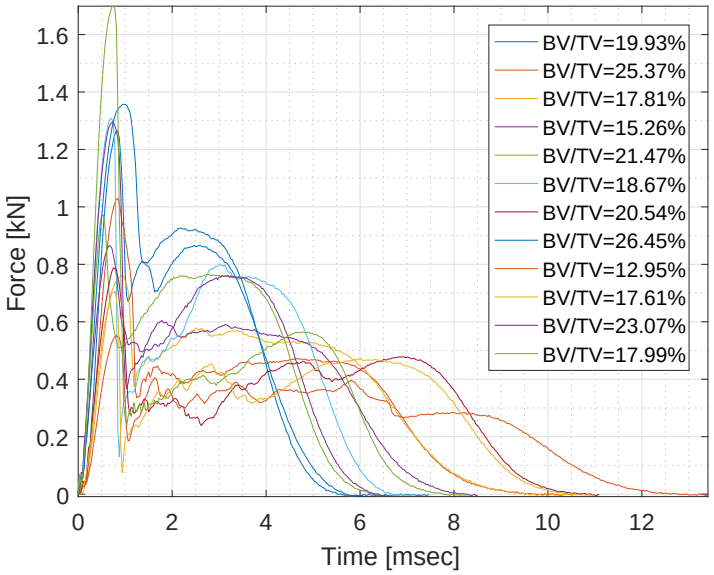

(b) which the failure is localised

Figure 5.16: Force responses of low BV/TV samples

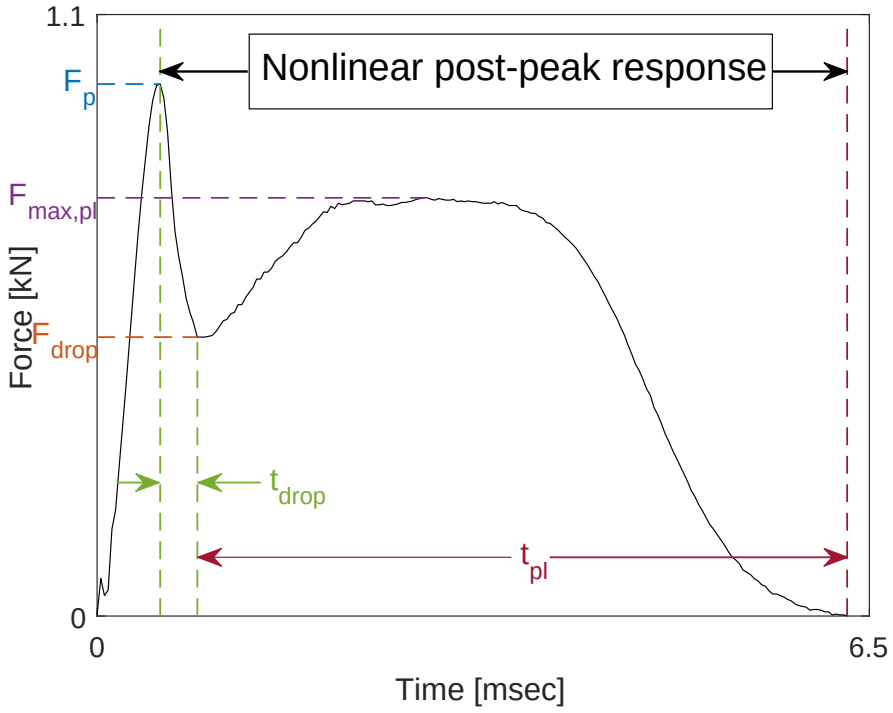

Figure 5.17: Key outputs in typical nonlinear post-elastic response

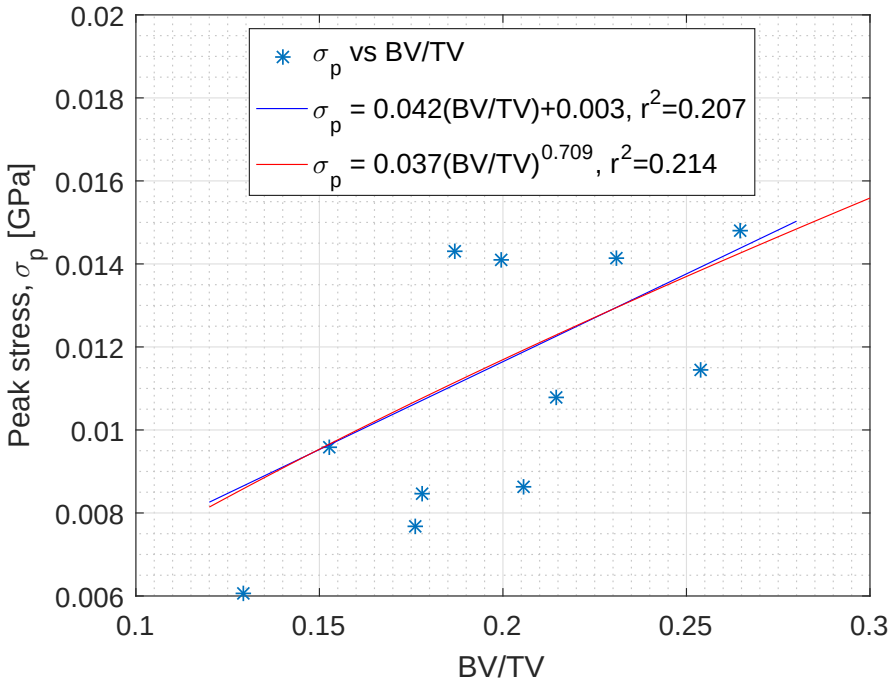

Figure 5.18: Linear and power law regressions for peak stress-BV/TV relation

The peak stresses, σ_{p} in Fig. 5.18 fall in the range of 6-15 MPa for 13.0-26.5% BV/TV. This range is comparable to the tested samples under SHPB which reported strengths around 5-20 MPa (Shim et al., 2005) and also by uniaxial compression tests of varying strain rate (Linde et al., 1991) suggesting strength between 2 to 15 MPa for trabecular bone.

Attempts to relate the drop force (F_{drop}) and the peak load in plastic regime ($F_{\mathrm{max,pl}}$) also result in low r^2 values when related to BV/TV as shown in Fig. 5.19. The power law is chosen as the regression type due to its slightly better r^2 representation compared to the linear model for both output parameters. All three force responses, namely $\sigma_{\mathrm{p}}, F_{\mathrm{drop}}$ and $F_{\mathrm{max,pl}}$ appear to increase with BV/TV, but have poor correlations. So while direct proportionality between load and BV/TV holds for samples with a near-elastic response (Fig. 5.10 and Eqns. 5.2-5.3), it does not depict the response of the failed samples well. There are two key reasons for this. Firstly the samples are not homogeneous and have different shapes and sizes of "weak" zones (refer to Tables 5.1 and 5.2) and secondly the BV/TV parameter does not incorporate the inherent anisotropy of trabecular bone.

5.5.2 Duration of plasticity

This study also considered the time durations in Fig. 5.17 which are t_{drop} and t_{pl}. These output parameters were also regressed against BV/TV values.

It was shown previously in the elastic response that the contact time has inverse proportionality with BV/TV, e.g. Fig. 5.11 and Eqn. 5.5. As for the time-related response in the plastic region, e.g. the prolonged time in plastic region t_{pl} demonstrates a similar trend as shown in Fig. 5.20.

Meanwhile, another time-based output, viz. the drop time (t_{drop}) was found to increase with BV/TV, though it had low coefficients of determination ($r^2 \approx 0.1$) for both linear and power law models as shown in Fig. 5.21. It may be recalled

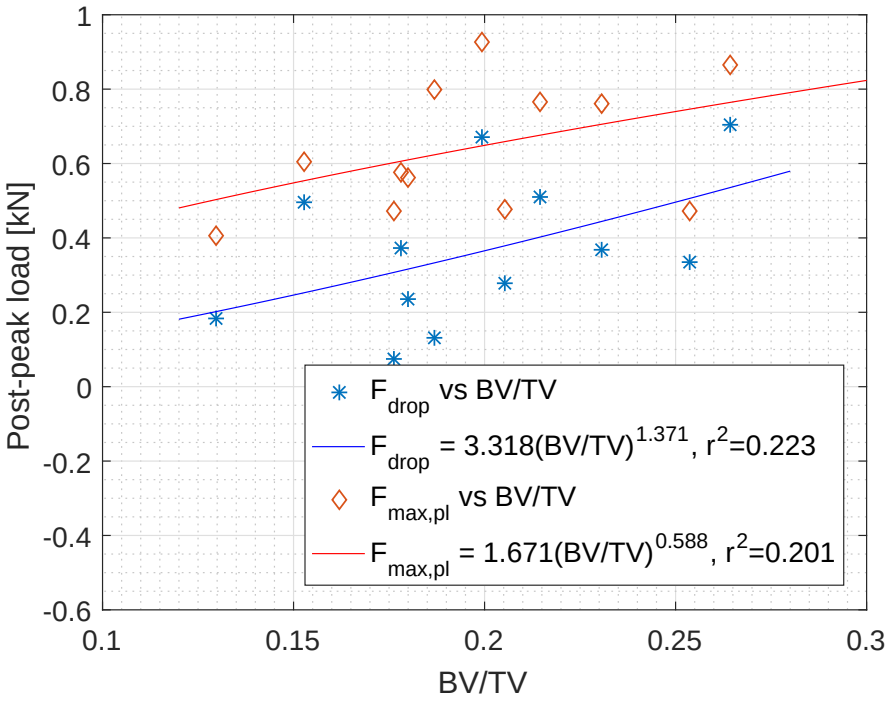

Figure 5.19: Power law regressions for drop force- and plastic peak load-BV/TV relations

that for elastic analysis, the pulse width (and the corresponding drop duration) decreases with increasing BV/TV values. The opposite trend in drop time of the failed samples can be explained by the fact that lower BV/TV samples are likely to be more "brittle" than the higher BV/TV samples, thereby exhibiting a sharper drop.

5.5.3 Verdict on the sample failure

The samples fail mainly due to two reasons: existence of growth plate found in the case of high BV/TV samples from the femoral head; or due to low bone volume fraction as seen in samples from trochanters. The response of the failed samples typically has three regions: a rise up to the peak load, a proportion of which is likely to be elastic; a post-elastic localisation response; followed by a prolonged plastic phase. This trend is demonstrated by samples with medium

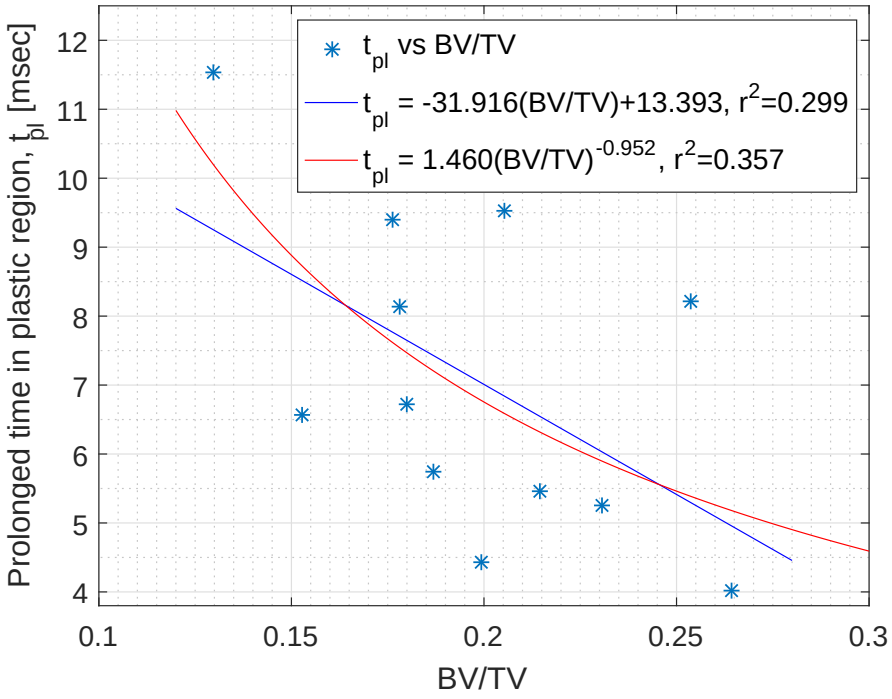

Figure 5.20: Linear and power law regressions for prolonged plastic time-BV/TV relation

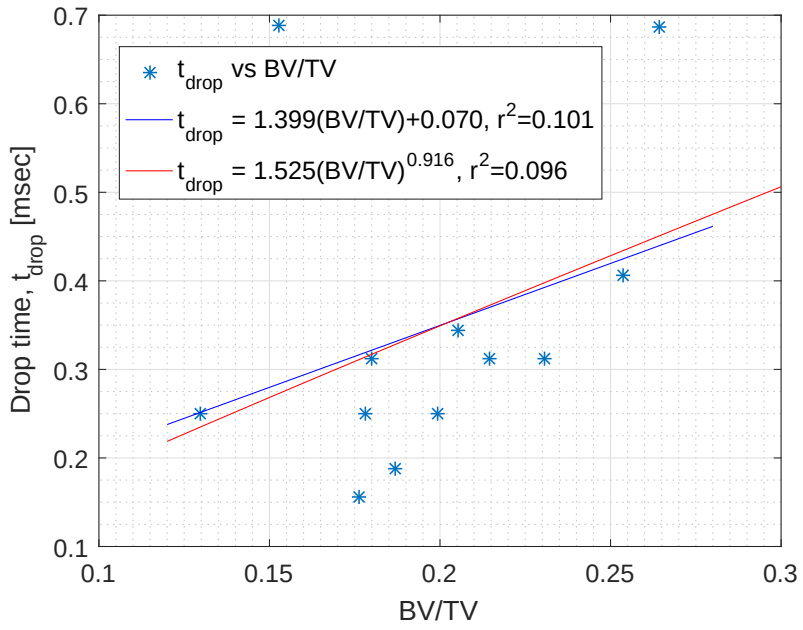

Figure 5.21: Linear and power law regressions for drop time-BV/TV relation

BV/TV values. Samples with significantly low BV/TV values are seen to get crushed with little discrenible trend.

5.5.4 Elasto-softening FE modelling

In this Section, FE modelling is used as an attempt to simulate the inelastic response by using elasto-plasticity. The primary aim is to simulate the shape shown in Fig. 5.17. The FE model employs von Mises yield criterion to define the material in plastic regime. In the first instance, the yield strength is assigned to be 10.88 MPa based on the average peak stress in Fig. 5.18. The post-yield behaviour is defined by the isotropic strain softening model in which the yield surface in multiaxial plasticity shrinks in an affine manner, by assigning the material's tangent modulus to be a negative value, i.e. $E_{\tan} < 0$. Previous studies have used strain softening to simulate localisation, e.g. Keyak (2001); Hosseini et al. (2012). Five models are developed with varying post-elastic negative tangent moduli of $E_{\tan} = -53.1, -26.55, -15.93, -10.62$ and -5.31 MPa for $-10, -5, -3, -2$ and -1% of E softening respectively. The elastic modulus is defined to be 531 MPa while the softening $E_{\tan}$ values are arbitrarily chosen.

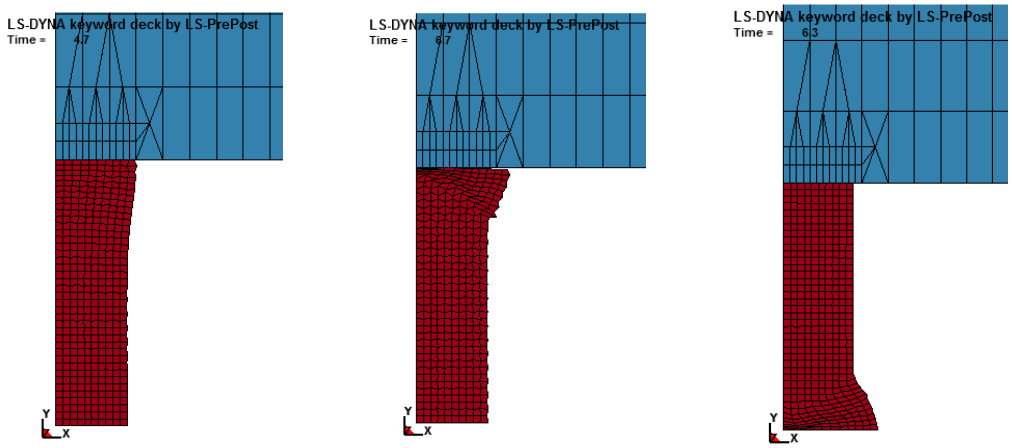

(a) -0.03E **(b)** -0.05E **(c)** -0.10E

Figure 5.22: Sample conditions at the end of simulation time in softening models

The deformations for these softening models are shown in Fig. 5.22 for $E_{\tan} = -3\%, -5\%$ and -10% of E. $E_{\tan} = -0.03E$ appears to cause the elements not to be severely distorted as shown in Fig. 5.22a; this case is close to perfect-plasticity and plastic deformations appear to be diffused along the length of the sample rather than being localised. Meanwhile, in the cases with steeper softening slopes, the localised deformation is either at the top (e.g. 5% in Fig. 5.22b) or bottom (e.g. 10% in Fig. 5.22c) section of the bar. It was discussed in the closed-form solution that the stresses at the end struck increase in steps every time the wave returns. The same phenomenon occurs at the restrained end as well. Therefore, localisation can be initiated at either of the two ends. This deformation mode is not observed in the case of perfect-plasticity, e.g. Fig. 5.12 or if hardening plasticity is applied.

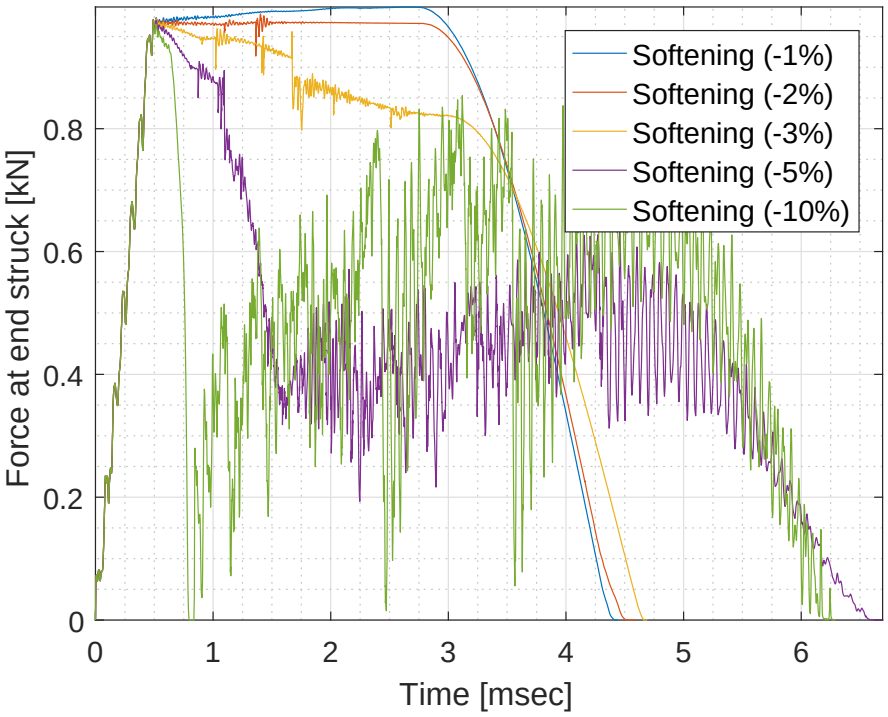

Figure 5.23: FE softening responses at the end struck for five varying $E_{\tan}$

The forces at end struck for five varying $E_{\tan}$ softening models are plotted in Fig. 5.23. The elastic region is identical up to the assigned yield stress of 10.88

MPa, corresponds to normal yield force of approximately 0.96 kN. The load in -10% model drops down to zero in an almost brittle manner, then producing the nonlinear post-peak response which can be seen to be somewhat comparable to the idealised experimental pattern of Fig. 5.17. A similar pattern is observed in -5% model. Both softening pulses produce high frequency jagged responses, which are likely to be due to numerical issues from this explicit code.

Meanwhile, the force responses for models with less steep tangent moduli, e.g. -1% of elastic modulus do not show radical drop of force from the yield value and less disturbed signal is depicted. Smoother signal in softening mode is explained by the less element distortion for less steep $E_{\tan}$ models, as illustrated in Fig. 5.22a. However, models with larger (less negative) $E_{\tan}$ values for simulating impact response fail to replicate the general behaviour of nonlinear post-peak response observed in the failed samples as shown in Fig. 5.17. These results assist in concluding that the attempt to capture the post-elastic responses of failed samples with low BV/TV is achievable by assigning sufficiently high negative tangent modulus value in softening.

The study did not include damping in the simulation of the response. It has been shown that for impulsive loading and low damping ratios, the influence of damping on the response is negligible (Chopra, 2001). It is known, however, that the numerical damping is introduced in the simulation by the algorithms in the FE software (Livermore Software Technology Corporation, 2017*b*).

Specimen-specific modelling was performed to check if softening plasticity models could replicate the experimental results. Two samples with significantly different BV/TV viz. 15.26% and 23.07% were chosen. The von Mises yield criterion is again used, while the yield strengths were assigned as 9.6 MPa and 14.1 MPa for 15.26% and 23.07% samples respectively; these are obtained by dividing their

maximum force, $F_{\max}$ which is assumed to be at the yield point with the cross-sectional area of the specimen (shown in Fig. 5.18). The elastic modulus for the two specimens is estimated to be 312 and 545 MPa respectively from the E_{d}-BV/TV relation (Eqn. 5.10) which is derived in the following Section.

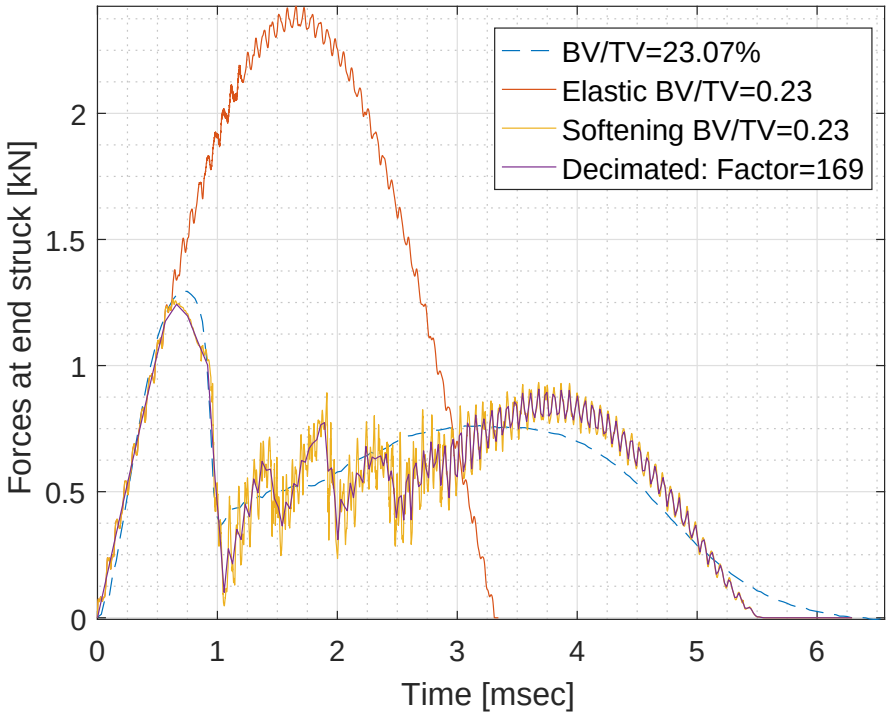

Figure 5.24: An example of specimen-specific softening models (including decimation) with its elastic case

It is important to note that when a sample demonstrated inelastic impact response, it is unable to attain the peak load at the end struck which it would have experienced had it remained elastic. The assigned elastic modulus of 545 MPa (BV/TV=23.07%) demonstrates this effect as shown in Fig. 5.24 in which the elastic case has higher peak load compared to the assigned yield force, hence supporting the selected yield strength for the sample. The isotropic softening model is defined with $E_{\tan} = -0.1E$ producing noisy post-yield response as shown in the figure. A 'decimate' filter is applied to the response (the details of this feature are explained in the next Chapter). The filtering process produces

a comparatively smoother pulse while retaining the important output parameters, e.g. the overall shape, yield point and end time.

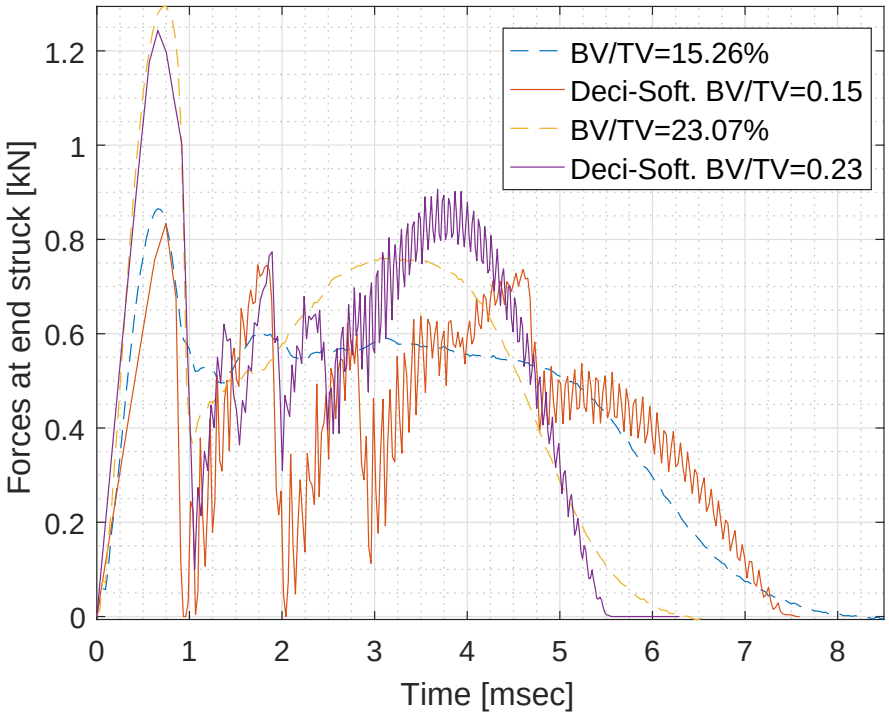

Figure 5.25: Comparing two specimen-specific cases. 10% softening is used for BV/TV=23.07% while the lower BV/TV model requires 20% softening to capture the post-elastic response

Both filtered models, viz. BV/TV=0.15 and 0.23 are compared in Fig. 5.25 against their experimental results. The post-elastic response from FE simulations is seen to be good in capturing: 1) the drop of load after yield point; 2) second peak load in plastic regime ($F_{\text{max,pl}}$); and 3) the prolonged plastic time, t_{pl}. Nevertheless, the drop force (F_{drop}) value simulated by FE models requires further investigation. The FE models also show that the lower BV/TV value (hence lower elastic modulus) is proportional to the yield strength (see Fig. 5.18), while having inverse proportionality with the plastic response time similar to regressions shown in Fig. 5.20.

In bone mechanics, the yield criterion is mostly based on strain rather than stress.

For instance, Kopperdahl and Keaveny (1998) reported 0.84% yield strain under compression for human vertebral specimens. Putting this value along with the modulus of 531 MPa results in the corresponding yield strength of 4.46 MPa, which is substantially lower than the assigned yield strength values based on the experimental results. It should, however, be noted that the available yield strain values are from static tests. It is generally accepted that both elastic modulus and yield strength of a material increase for dynamic loading, i.e. tested under higher strain rate (Meyers, 1994). In this study, simulations were attempted with the low value of yield strength developed from previously conducted static tests. These simulations led to severe distortion of elements resulting in the formation of negative volume, thus terminating the simulation procedure with error. An attempt to simulate post-elastic behaviour requires not only strength parameters, e.g. yield strength; but also post-peak evolutionary behaviour. This is important as stresses from regions that are unable to carry any more loads are redistributed.

5.6 Loading rate, $\dot{F}$ in elastic region

Despite obvious differences between high and low BV/TV samples from the femoral head and greater trochanter respectively, all pulse responses share a similar trait, which is the initial rising force up to the peak load, in which at least the initial part (say the first half of the rising load) is likely to be in the elastic region. Even the failed samples from trochanter have this rising response in the initial stage.

Figure 5.26 shows two force data on impact for a high BV/TV sample (BV/TV=46.85%) and a low BV/TV sample (BV/TV=26.45%). In both cases, the values of forces up to half the peak load are included. Although it is recognised that the rising pulse forces on impact does not vary linearly, linear regression is used to draw line of best fit for each set of data, in which the gradient of such

lines is the loading rate, $\dot{F}$. The coefficients of determination, r^2 which are very close to unity show that straight line fit is a good approximation.

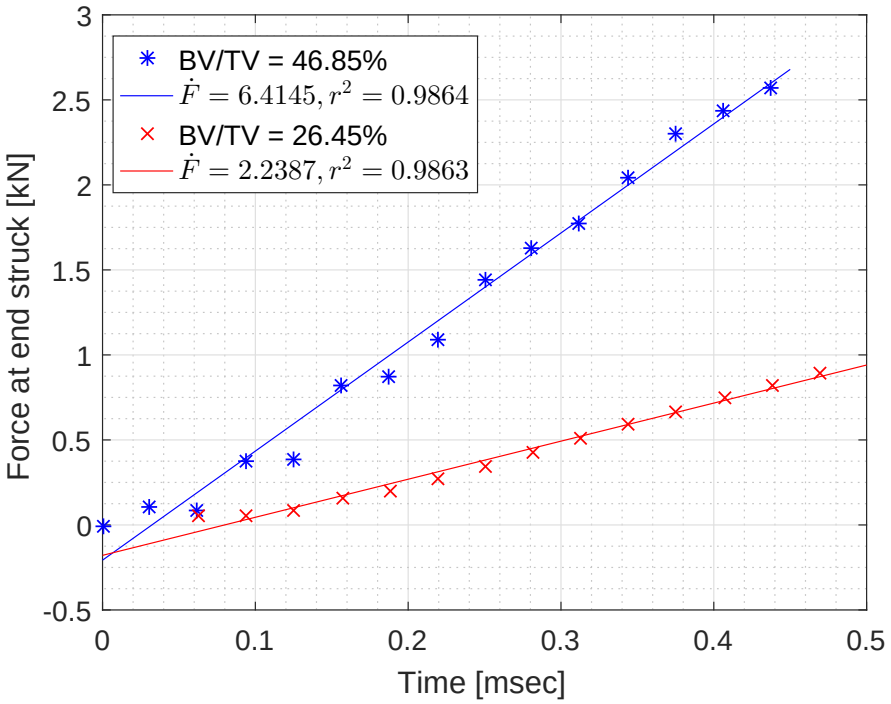

Figure 5.26: Gradients of linear region representing loading rate, $\dot{F}$

The analysis on loading rate-bone fraction ($\dot{F}-$BV/TV) relation enables these data to be utilised for deriving the dynamic elastic modulus of trabecular bone samples as a function of BV/TV by relating this to the theoretical $\dot{F} - E$ expression of Eqn. 3.49. Similar regression method as in Section 3.5 is used to fit the rising experimental datapoints hence obtaining its loading rate for each sample with known BV/TV. The results are shown in Fig. 5.27, scattered between $12 - 53\%$ of BV/TV.

Two regression models are used to represent the scattered data, namely the linear and power law. The equations of best fit for $\dot{F}-$BV/TV are shown in Fig. 5.27, which are

$$\dot{F} = 13.7048(\text{BV/TV}) - 1.0020 \quad [\text{kN/msec}] \tag{5.7}$$

and

$$\dot{F} = 14.9943(\text{BV/TV})^{1.3526} \quad [\text{kN/msec}] \tag{5.8}$$

for linear and power law respectively. Both equations look quite similar, approximately showing a linear relationship. The proposed linear and power law fit equations have the coefficient of determinations, r^2 of 0.925 and 0.918 respectively, showing excellent representation of the regressions for the scattered data. Figures 5.26 and 5.27 show high $\dot{F}$ value due to higher BV/TV parameter indicating a stiff response, establishing a fact which is also supported by the two regression models in Eqns. 5.7 and 5.8.

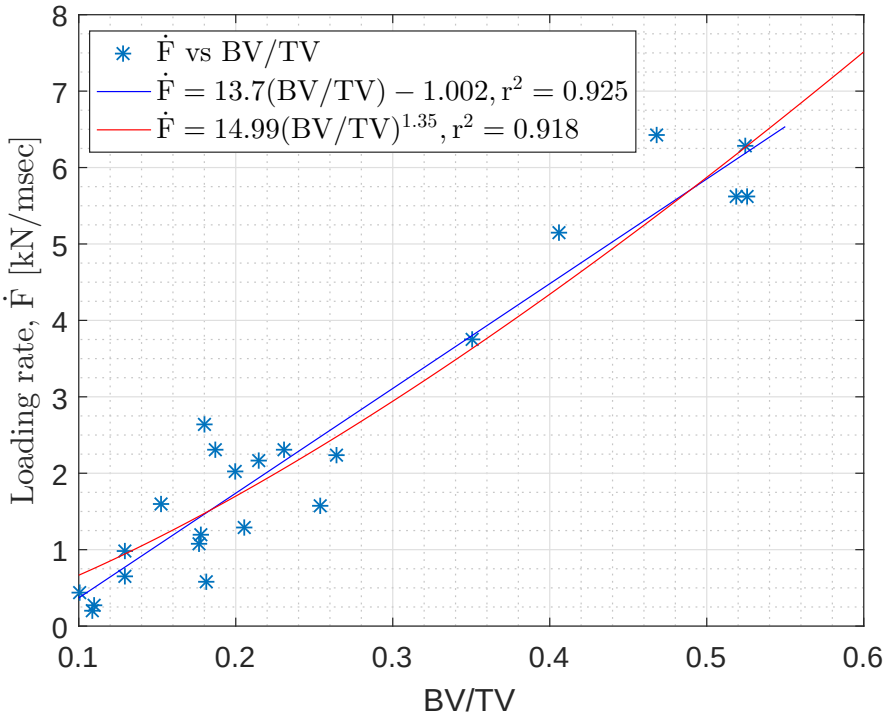

Figure 5.27: Linear and power law regressions for loading rate-bone ratio ($\dot{F}$−BV/TV) relation

Solving for both Eqns. 5.7 and 5.8 with the closed-form solution's expression, $\dot{F} = 3.7811E$ (Eqn. 3.49), the dynamic elastic moduli can be expressed as

$$E_{\text{d}} = 3.62455(\text{BV/TV}) - 0.265 \quad [\text{GPa}] \tag{5.9}$$

and

$$E_{\mathrm{d}} = 3.96559(\mathrm{BV/TV})^{1.3526} \quad [\mathrm{GPa}] \tag{5.10}$$

as functions of bone volume fraction, BV/TV based on the loading rate data. Equations 5.9 and 5.10 correlate elastic modulus and BV/TV in the forms of linear and power law respectively, while the resulting moduli are quite comparable for given BV/TV variables. Equations 5.9 and 5.10 are derived based on BV/TV of samples in the range of $12.95 - 52.57\%$.

5.7 Limitations

This Chapter considered the determination of the elastic and post-elastic mechanical properties of trabecular bone subjected to impact loading on the basis of bone volume fraction. While this approach has provided a number of good results, it clearly has limitations. The first limitation is the assumption of isotropy of trabecular bone samples. The mathematical relationships provided by the closed-form solution do not consider the degree of anisotropy (DoA) presents in the actual bone samples. Secondly, the samples are not homogeneous. The BV/TV values of the samples in the three regions from top to bottom show considerable variation. Thirdly, the manner in which the load is carried by the samples is unlikely to be axisymmetric. This happens because while the samples were cored with an attempt to align them in the principal trabecular directions, there is no practical approach to fully ensure this.

The simulation and analytical results have a jagged pattern which represents the dynamic wave bouncing back and forth. This type of response can only be possibly captured experimentally if an extremely high sampling rate were to be employed.

Chapter 6

Analysis on the derived dynamic elastic modulus functions

6.1 Introduction

This Chapter considers the dynamic elastic moduli, E_{d}, derived in the last Chapter. A number of mechanical properties have been reported as representing dynamic behaviour in literature, however most tests in these studies were conducted in a static or a quasi-static manner under relatively low strain rates, e.g. 0.03 /sec (Lotz et al., 1990) and 0.01 /sec (Goulet et al., 1994).

The main objective in this Chapter is to consider the four derived dynamic elastic modulus in Eqns. 5.4, 5.6, 5.9 and 5.10 with mathematical expressions reported in the literature, as well as with the creep tests conducted at Edinburgh (Xie et al., 2017). FE analysis is used to predict the strain rate in the impact tests, in order to justify our elastic moduli equations categorically as dynamic.

6.2 Problem definition

The bone is expected to behave in an elastically stiffer manner when subjected to dynamic loads (Hansen et al., 2008). The derived elastic moduli are suitable to be labelled as 'dynamic' when the bone is loaded at a relatively high strain rate, e.g. (Shim et al., 2005). Even though the impact test is categorised as dynamic in nature, the strain rate involved in the test is required to assign the modulus to the loading rate. This strain rate can be derived using FE analysis. Elemental strains are analysed in some elements of the FE bone model in order to estimate the strain rate experienced by the bone model.

6.3 Strain rate via FE analysis

Impact on bone from a heavy object apparently would be expected to subject bone to a relatively high strain rate loading. In the absence of experimental measurements, which could be facilitated by dynamic strain gauges or high speed camera, a numerical approach provides an alternative. In this study, the strain rate is obtained via FE analysis, in which simulation of impact with assumed material properties is used to evaluate displacements and strains and consequently the strain rate.

Two methods were employed to extract strain history in this study: 1) From the nodal displacement history and 2) directly from the strain data. In both cases, the vertical direction, i.e. the path of impactor, is considered for the evaluation of displacement or strain. The vertical displacement history of a top node between centre and circumference for sample with $E = 650$ MPa is shown in Fig. 6.1 with its corresponding apparent vertical normal strain (ϵ_{vert}) obtained by dividing the top displacement with the undeformed length of bar, i.e. 21 mm.

Figure 6.1 shows that the strain rate is expected to be the highest immediately

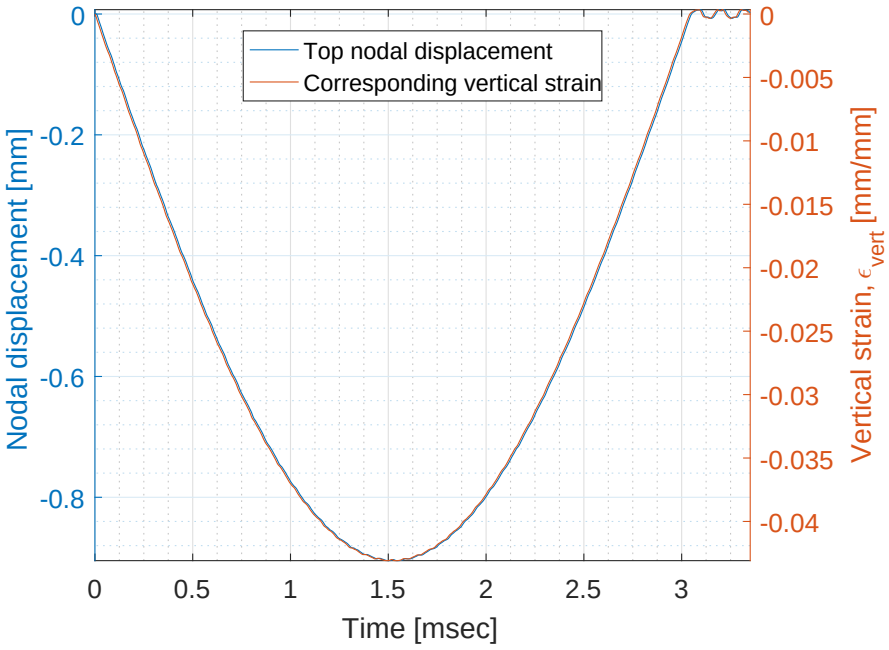

Figure 6.1: Top nodal displacement and corresponding apparent vertical normal strain

after the impact and reduces to zero before changing sign. This study focuses on the evaluation of average ($\dot{\epsilon}_{\text{ave}}$) and secant ($\dot{\epsilon}_{\text{sct}}$) strain rates across the whole sample, which will be described later.

Two methods were used to filter the strain signal. The first method was a 'moving-average', in which the average of samples was taken over a sliding window of 501-span length across neighbouring data with the current datapoint as the centre of the filtering process. The second filter is 'decimate' with a factor of 169 with a special feature of finite impulse response (FIR) included. The FIR option maintains the first data in the original signal, hence ensuring the accuracy of capturing the maximum derived strain rate at the initial instance of the impact in this work. In the analysis conducted, the signal contains 6000-6500 elements. The results after employing the two filtering methods are shown in Fig. 6.2a.

The derivative of the filtered vertical strain history is performed to obtain the

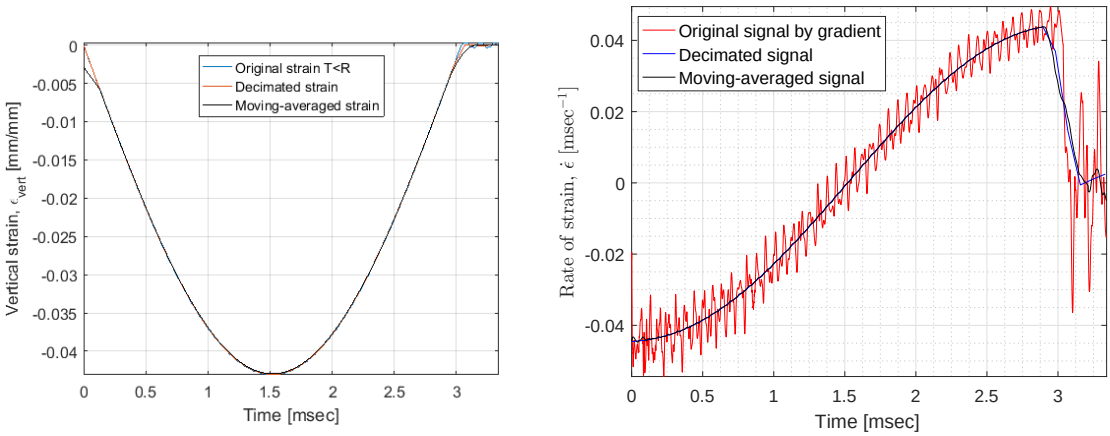

(a) Filtered signals

(b) Strain rates

Figure 6.2: Vertical normal strain rate from displacement

strain rate. In this method, each datapoint in the strain curve is differentiated by means of the numerical 'Gradient' function in MATLAB and the results are shown in Fig. 6.2b. In this case of impact response analysis, the derived strain rate will vary with time. The strain rate history was calculated as the ratio between gradients of both strain and time datasets, in which the spacing between each datapoint is assumed to be unity. This 'gradient' function calculates the central difference for interior datapoints, which is best explained by one-dimensional gradient grad_strain = gradient(strain) as

$$\text{grad\_strain}(j) = 0.5\big[\text{strain}(j+1) - \text{strain}(j-1)\big] \tag{6.1}$$

where j is the current datapoint which varies from the second to the second last data point in the strain output.

Figure 6.2b shows that the average strain rate at impact is 44.53 /sec by considering decimated signal. Meanwhile, the secant strain rate was obtained by considering the maximum normal strain and the time taken to achieve this is 28.04 /sec. These strain rates are significantly higher than those from previous

studies that employed strain rates of 0.0033 /sec (Li and Aspden, 1997) and 0.01 /sec (Goulet et al., 1994).

In the second approach, strain was obtained directly from integration points. The minimum principal strain was used for analysis (it was found to correspond to the vertical normal strain). Strains at the single integration point of selected elements were extracted from the FE analysis results.

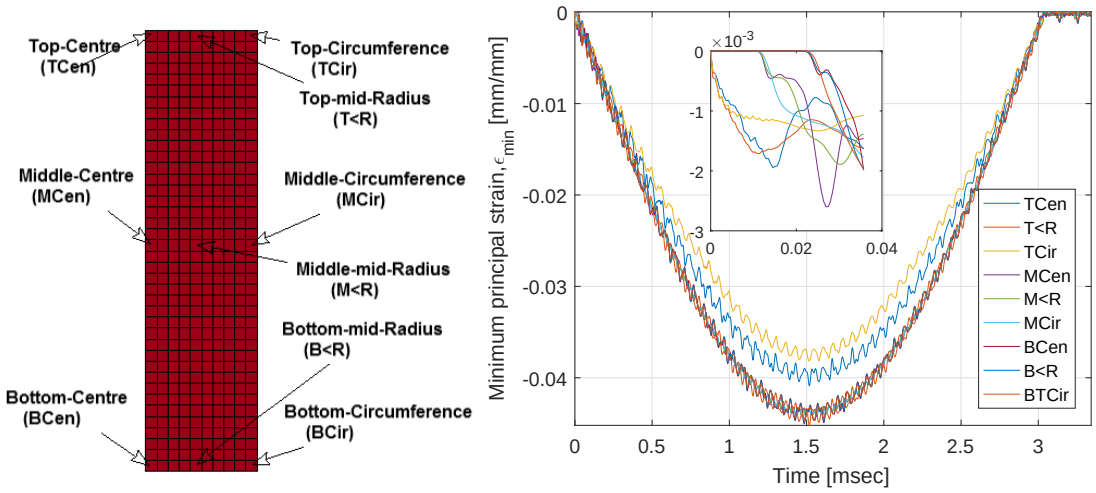

(a) Locations of selected elements **(b)** Plotted elemental history

Figure 6.3: Minimum principal strain distribution

The model of impacted bone is shown in Fig. 6.3a labelled with nine (9) main segments: 'Centre', 'Circumference' and 'Mid-radius' in the radial direction and top, middle and bottom in the axial direction. Three elements are selected at the top: Top-Centre (TCen), Top-mid-radius (T<R) and Top-Circumference (TCir) (Fig. 6.3a). Similarly three elements at mid-height and three in the bottom row are selected and named appropriately.

The strain history at the integration point of the selected nine elements is shown in Fig. 6.3b which shows most elements have similar strain histories, with only elements at the circumference and centre of the impacted surface have slightly lower strain readings, perhaps as a result of LS-DYNA calculating the

strains. Other regions have very comparable strain history if averaged values are considered for representing the jagged pattern. At the local levels, large fluctuation of strain occurs as a result of the dynamic effect.

In a dynamic test, strain varies with time and location. While mathematically strain is associated with an infinitesimal volume, in an experimental setting it is associated with a gauge length; a large gauge length provides an average strain over a larger region. In FE analysis where strains are evaluated from elemental nodal displacements, the gauge length is represented by the element size. More localised strains will be output with decrease in element size. This is particularly relevant for wave propagation problems considered in this study. The discussed closed-form solution demonstrates the strong fluctuation in stresses (and consequently the strains) during the response pulse. It is apparent that at the local level, strain rates due to impact are extremely high. However, this study is interested in apparent strains associated with the entire sample.

As an indication of wave propagation through the model, the zoom-in box in Fig. 6.3b depicts the lagged starting time of the responses experienced by elements at the middle and bottom sections compared to the end struck (top), demonstrating the time required for the stress wave to travel from the end struck towards the bottom support. The secant strain rate, $\dot{\epsilon}_{\text{sct}}$ from Fig. 6.3b is estimated to be 29.78 /sec considering the peak strain of -0.0452 and the time taken to reach the value to be 1.518 msec, which is similar to that found from Fig. 6.1. In the subsequent analysis on strain, an element in T<R region is chosen as a representative of the whole model to derive the apparent strain rate since it can be considered as a generic representation of the rest of the regions.

The effect of different elastic moduli, E in the inverse-modelling models (Section 5.4) on minimum principal strain is shown in Fig. 6.4. In the initial period following the impact, the strain history is similar. The strain history diverges for

different moduli and the peak strains are inversely proportional to the Young's modulus. As a basic cross-check on the strain history pulses, the peak strain for $E = 1.40$ GPa model is compared to the corresponding strain value obtained via Hooke's law based on the model's peak load in Fig. 5.12. The peak value of minimum principal strain for each model as shown in Fig. 6.4 corresponds well to the peak strain calculated by considering the Hooke's law in its basic form.

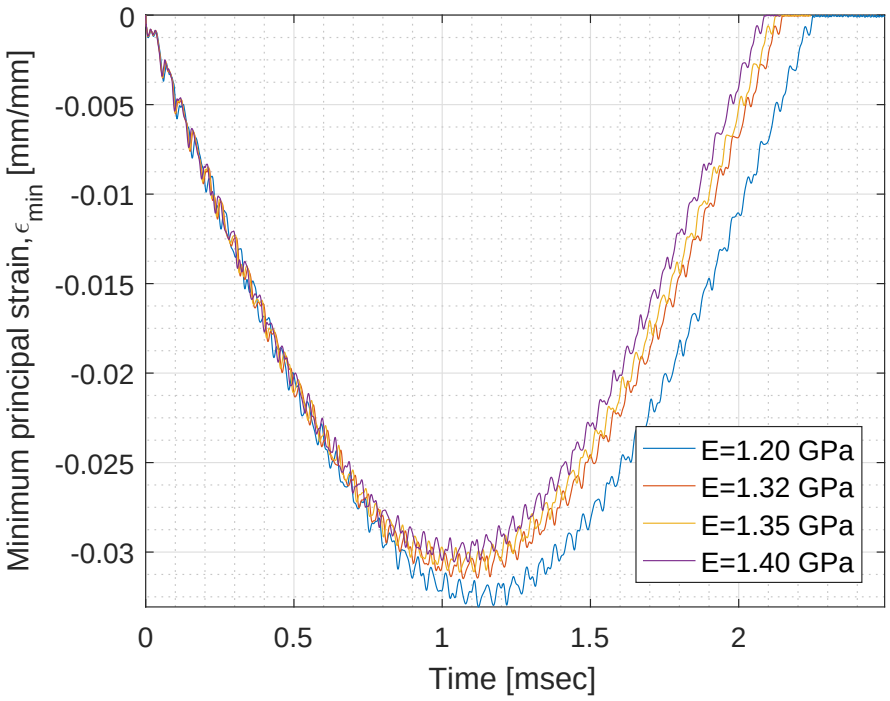

Figure 6.4: The effect of varying elastic modulus on principal strain

The absolute maximum strain values evaluated by this elastic FE analysis undertaken with the largest elastic moduli found from trabecular bone tests in the last Chapter are around 3-3.25% in compression. This range of strain is beyond the limit of the reported yield strain for trabecular bone found from static tests (Bayraktar et al., 2004), suggesting the samples which were considered to behave elastically (plotted in Fig. 5.9) may have experienced some inelastic deformation. Previous studies undertaken using static mechanical tests have shown that the yield strain of human trabecular bone in compression is around 1.04% (Bayraktar

et al., 2004). While some studies indicate that yield stress increases with loading rate, similar statements about strain have not been made.

The jagged strain response will produce jagged strain gradients, with variations likely to increase as element size is decreased. Therefore, similar filtering methods as in the evaluation of strain rate from top displacement were utilised. The results after employing the two filtering methods are shown in Fig. 6.5a.

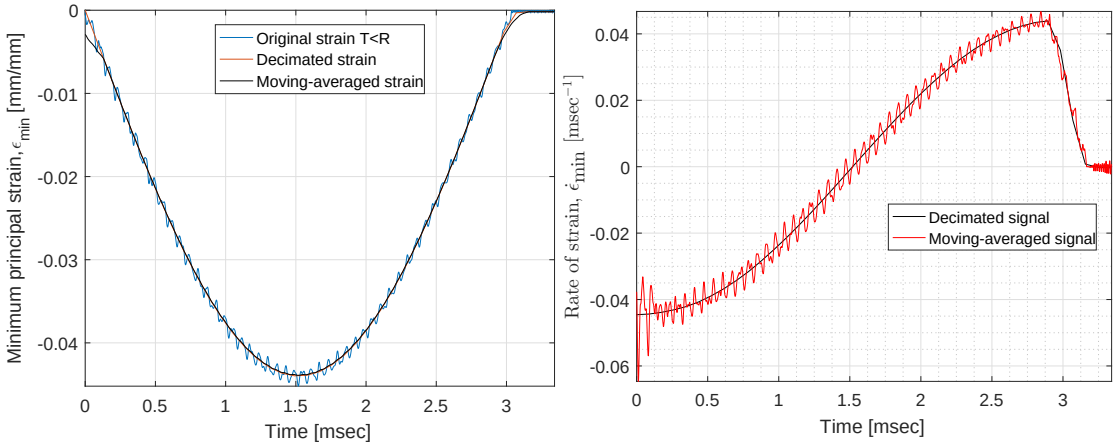

(a) The original and filtered signals

(b) Using '*Gradient*' function

Figure 6.5: Method to obtain strain rate. The elastic modulus is assumed to be 650 MPa

From the strain history, it is apparent that the maximum rates will be at the start and end instants of the pulse and zero when the strain attains peak value. The rates obtained from both filtered signals are comparable, however the gradient of decimated signal is smoother compared to the moving-averaged, hence the decimated results will be utilised in the subsequent investigation. Decimation by sufficiently-high factor produces smooth parabolic curve.

Important features between strain and its rate are labelled in Fig. 6.6. The double-ordinate plots show that the opposing rates are caused by the negative parabolic shape of the decimated strain pulse. As expected, the time corresponding to zero rate, $t_{\text{zero-rate}}$ is at the instant of peak minimum principal strain,

$|\epsilon|_{\max}$. Meanwhile, the end time, $t_{\text{pulse}} = 3.04$ msec in this figure corresponds to the force-time plot of Fig. 5.12 for 650-MPa elastic modulus model.

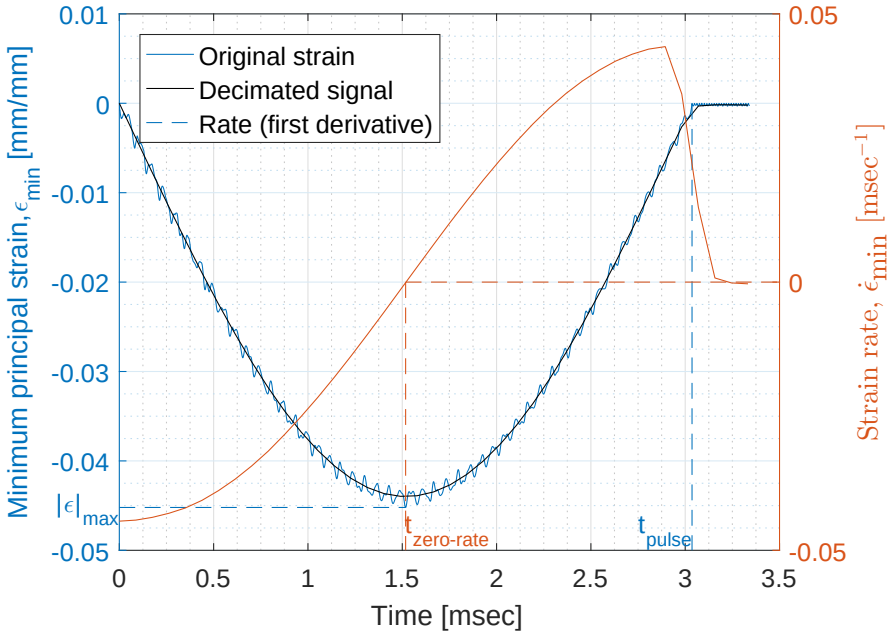

Figure 6.6: Important features of strain and its rate. The model uses E=650 MPa

Consider pulse width-elastic modulus (Eqn. 3.45) and peak load-modulus (Eqn. 3.44) relations, the secant peak strain is estimated to be 31 /sec and it is independent of elastic modulus as shown in the closed-form solution. The effect of E on the strain rate is shown in Fig. 6.7 for five FE models. Similar with the previous explanation by the closed-form solution, the elastic modulus by FE analysis does not affect the initial and final (at the end of pulse) strain rates which for the parameters considered here are in the range of ± 44.3 sec^{-1}. However, between the time instant of the strike and the peak strain is attained, samples with higher elastic modulus have a lower absolute strain rate. If a secant strain rate is estimated by simply using the peak strain and the time taken to attain it, then the secant strain rate is found to slightly decrease with increasing moduli, e.g. 29.78 /sec and 29.36 /sec for 650 MPa and 1400 MPa models respectively. This slight discrepancy, however, can be attributed as only a numerical issue.

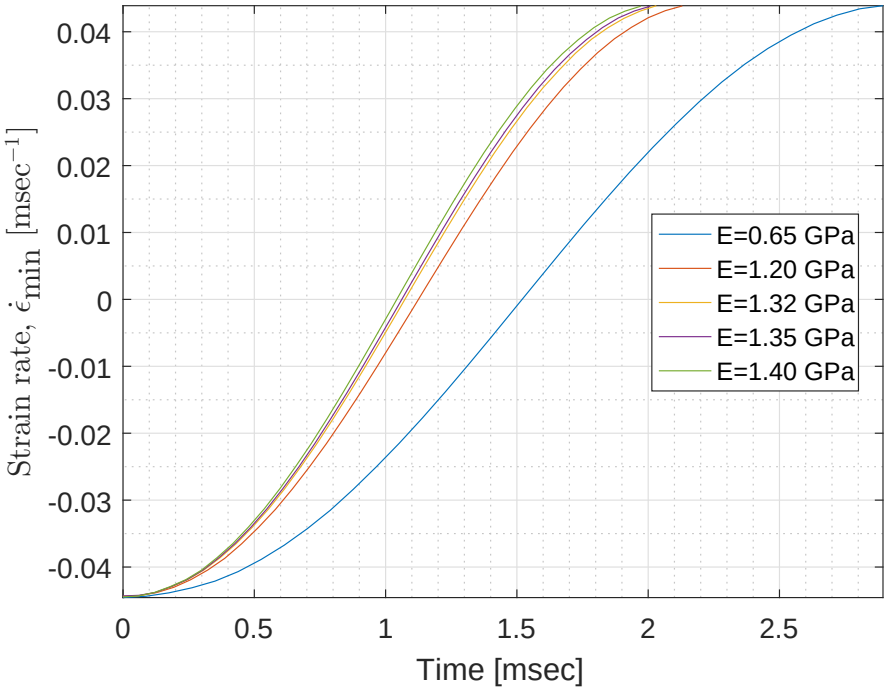

Figure 6.7: The effect of varying elastic modulus on principal strain rate

Table 6.1 shows the strain rates derived by the FE analysis. Both methods (displacement and derivation of strain) give comparable values of secant (28-30 /sec) and average (44-45 /sec) strain rates. Average strain rates are higher because they are measured at the initial rise of the strain history. This range of strain rates is around the mean±standard deviation value reported by Enns-Bray et al. (2018) of 48 ± 19.7 /sec when trabecular bone samples were subjected to mass dropped from 36 mm height.

If local strain rates are considered, they change abruptly from small to large values (see Fig. 6.4) as the wave travels back and forth. These abrupt changes cannot be readily included in the closed-form solution or the numerical simulation. It has been shown, however, that the averaged strain rates i.e. $\dot{\epsilon}_{\text{sct}}$ and $\dot{\epsilon}_{\text{ave}}$ do not change with elastic modulus (see Fig. 6.7 and Table 6.1), since increasing modulus results in lower peak strain along with shorter pulse duration (Fig. 6.4). Therefore, the inclusion of strain rate effect from a specific drop height is not

Table 6.1: Strain rates of the current impulsive system by FE method and closed-form solution. E_1, E_2 and E_3 refer to 0.65 GPa, 1.2 GPa and 1.4 GPa models respectively

Type	Method	Source	Strain rate [sec^{-1}]		
			E_1	E_2	E_3
Secant, $\dot{\epsilon}_{\text{sct}}$	FE	Apparent strain	28.04	28.78	28.80
		Principal strain	29.78	29.46	29.36
	CF	Closed-form solution		31.23	
Average, $\dot{\epsilon}_{\text{ave}}$	FE	Apparent strain	44.56	44.39	44.48
		Principal strain	43.90	43.86	43.83

*Apparent strain was obtained from top displacement history

**Minimum principal strain was calculated at integration point

required. In the case of increasing drop height, on the other hand, the strain rate will be automatically higher which will possibly require a higher dynamic modulus as a consequence in the numerical simulation.

Young's modulus of bone has been reported to increase by the factor of 1.5 when the applied strain rate was 6 times higher (Hansen et al., 2008). Increase of modulus with strain rate has also been reported for concretes, though the magnification factor has been reported not to be significantly higher (Wang et al., 2012; Deng et al., 2016). As a physical explanation, the bone is viscoelastic when it is in its natural wet condition (Lakes et al., 1979); behaving like a spring with a small shock absorber (Turner and Burr, 2001; Lakes, 2001); this viscous nature disappears when it is dried (Park and Lakes, 1986; Turner and Burr, 2001). Inclusion of viscoelasticity has been shown to produce a stiffer response in Section 4.7. The presence of viscous damper takes into account the deformation speed, therefore the effect of strain rate on modulus is expected.

6.4 Comparison of the derived E_{d}(BV/TV) expressions

In order to evaluate the performance of the developed E_{d} equations, they are compared to several selected mathematical relations from previous work in literature as well as our own work on the creep test.

6.4.1 E_{d}(BV/TV) versus literature

A number of empirical relations have been suggested between elastic modulus of bone and its densitometric measures such as BV/TV, ash or apparent density (these were discussed in Chapter 2). Here, three such correlations are selected, namely in Li and Aspden (1997), Lotz et al. (1990) and Goulet et al. (1994) labelled as *Lit.1*, *Lit.2* and *Lit.3* respectively, to be compared with the derived dynamic elastic moduli in the present work. The three chosen expressions were all obtained from experimental tests applying compression on trabecular bone samples of either cylindrical (*Lit.1* and *Lit.2*) or cubic shape (*Lit.3*) obtained from different human anatomical sites. The densitometry of cancellous bones in *Lit.1-2* were reported as apparent density, while in *Lit.3* as BV/TV. In order to allow direct comparison with the derived moduli which are as functions of BV/TV in this study, therefore the apparent density parameter, ρ_{app} in *Lit.1-2* is converted to BV/TV by using

$$\mathrm{BV/TV} = \frac{\rho_{\mathrm{app}}}{1.8} \tag{6.2}$$

formulated by Helgason et al. (2008) based on the relative density reported by Gibson (1985), in which the density is in g/cm^3. As a side note, Johanson et al. (1993) claimed that the real and ash densities are not significantly correlated to

the apparent density; contradicting the normalisation formulae by Keyak et al. (1994). However Eqn. 6.2 relates apparent density with BV/TV instead.

Each test was conducted under different strain rates imparted by displacement of the compressive platens. However, the strain rates employed were considerably lower than the strain rates of current work in Table 6.1. The experimental details of *Lit.1-3* are tabulated in Table 6.2.

As mentioned previously, dynamic elastic moduli expressions, E_{d}, in this study are derived by combining closed-form parametric relations with three main outputs of the elastic response, namely the peak load (F_{max}), pulse width (t_{pulse}) and the loading rate ($\dot{F}$) as expressed by Eqns. 5.4, 5.6 and 5.9-5.10 respectively. The comparison of these four modulus predictors with respect to BV/TV is shown in Fig. 6.8 along with those from previous studies.

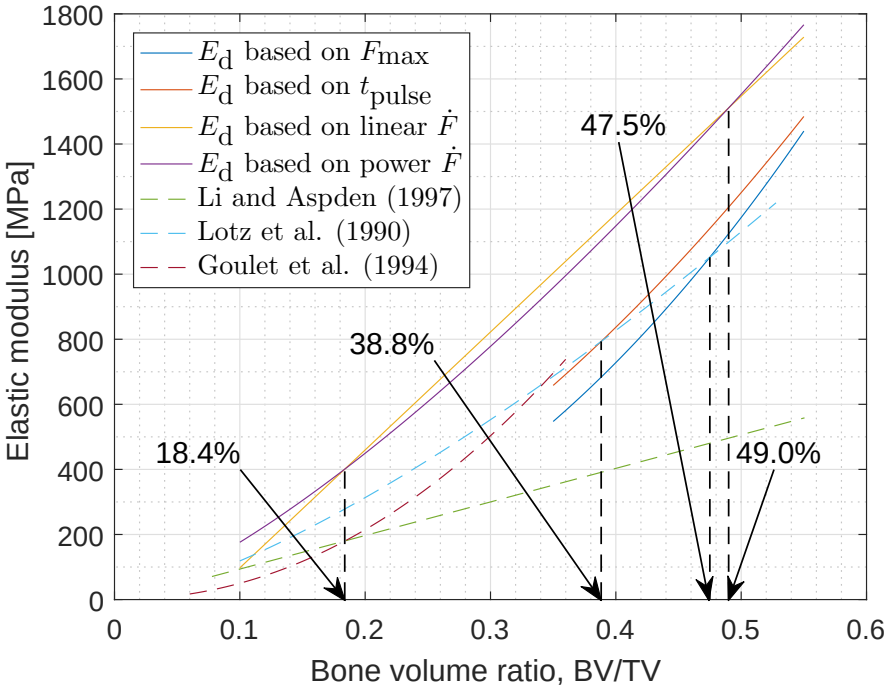

Figure 6.8: Comparison on the derived E_{d}(BV/TV) with different expressions from the literature

Table 6.2: Experimental details of particularly-selected literature

Reference	Study	Harvesting site	Densitometric measure	ρ-range (g/cm^3)	Geometry L^3 or D×L (mm)	Strain rate (sec^{-1})
Lit.1	Li and Aspden (1997)	Femoral head	ρ_{app}	$0.14 - 1.4$	9×7.7	0.0033
Lit.2	Lotz et al. (1990)	Femoral neck	ρ_{app}	$0.18 - 0.95$	9×5	0.03
Lit.3	Goulet et al. (1994)	Pooled	BV/TV	$0.06 - 0.36$	8^3	0.01

The dynamic moduli derived from loading rate, $\dot{F}$ are substantially higher than those from the peak load, $F_{\max}$ and pulse width, t_{pulse} from elastic responses. On the other hand, Eqn. 5.4 of $F_{\max}$ has the lowest elastic modulus predicted value.

Each of the plotted relations have their range, reflecting the BV/TV of specimens involved in the derivation. In the case of $F_{\max}$ and t_{pulse}, the BV/TV falls between $35.03 - 52.57\%$, representing dense samples from femoral head. On the other hand, as the derivation of $\dot{F}$ considers almost all samples (excluding those that were crushed and those with growth plates), the minimum BV/TV considered is 12.95%. The moduli equations based on $F_{\max}$ and t_{pulse} are expressed in power law, since their closed-form relations are developed with the square-root of E, i.e. $F_{\max} \propto \sqrt{E}$ and $t_{\text{pulse}} \propto 1/\sqrt{E}$. Meanwhile, the linear empirical relations $\dot{F} \propto E$ derived in the closed-form solution allows both linear and power law relations of $E_{\text{d}}-$BV/TV to be established.

The developed equations are compared to the three relations from previous studies as tabulated in Table 6.2. Since the elastic modulus in Lotz et al. (1990) and Li and Aspden (1997) were expressed as functions of apparent density, Eqn. 6.2 was used to convert the apparent density to BV/TV. The conversion was performed on both the elastic modulus relations as well as their range of density as shown in Table 6.3. This comparison is also shown in Fig. 6.8.

Table 6.3: Summary of E_d−BV/TV relations compared with literature

BV/TV	E_d: Elastic modulus [MPa]; *Lit.1-3*: Percentage difference [%] of E_d with *Lit.1-3*													
[%]	Eqn. 5.4			Eqn. 5.6			Eqn. 5.9				Eqn. 5.10			
	E_d	*Lit.1*	*Lit.2*	E_d	*Lit.1*	*Lit.2*	E_d	*Lit.1*	*Lit.2*	*Lit.3*	E_d	*Lit.1*	*Lit.2*	*Lit.3*
12.95							204.4	64.6	19.8	136.9	249.8	101.2	46.5	189.6
18.37		-			-		400.8	122.6	44.1	123.0	400.8	122.6	44.1	123.0
35.03	548.3	55.8	-20.2	659.1	87.3	-4.0	1004.7	185.5	46.3	44.1	959.7	172.7	39.7	37.6
38.83	683.5	74.8	-13.9	793.4	102.9	0.0	1142.4	192.1	44.0		1103.1	182.1	39.0	
47.50	1052.0	118.9	0.0	1140.3	137.3	8.4	1456.7	203.1	38.5		1448.8	201.5	37.7	
49.00	1124.4	126.7	2.3	1206.0	143.1	9.8	1511.0	204.7	37.5	-	1511.0	204.6	37.5	-
52.57	1307.0	145.3	7.8	1368.7	156.9	12.9	1640.4	207.9	35.3		1661.8	211.9	37.1	

**Lit.1*: Li and Aspden (1997): $E = 573[1.8(\mathrm{BV/TV})] - 9.4$; $\quad 0.078 \leq \mathrm{BV/TV} \leq 0.778$

**Lit.2*: Lotz et al. (1990): $E = 1310[1.8(\mathrm{BV/TV})]^{1.40}$; $\quad 0.10 \leq \mathrm{BV/TV} \leq 0.528$

**Lit.3*: Goulet et al. (1994): $E = 6310(\mathrm{BV/TV})^{2.10}$; $\quad 0.06 \leq \mathrm{BV/TV} \leq 0.36$

**Positive percentage differences signify higher value of E_d than modulus reported in the literature

The graphical plots in Fig. 6.8 are then numerically compared in Table 6.3 by utilising key BV/TV values while these values in *Lit.1-3* columns are percentage difference with the respective derived E_{d}. The listed BV/TV values mainly highlight the boundary of each curve as well as the intersection points between different curves which are also shown in the figure, and datapoint between subsequent intersections. For instance, at the intersection points between Eqns. 5.9 and 5.10 correspond to BV/TV=18.4% and 49.0%, their differences with relevant literature expressions are identical. In the case of Lotz et al. (1990), its curve intersects with Eqns. 5.4 and 5.6 show the differences are nil at BV/TV=47.5% and 38.8% respectively while its elastic modulus is slightly higher prior to these intersection points. Elsewhere, the dynamic elastic modulus equations show significantly higher predicted moduli up to three times compared to the values from literature, such as between Eqns. 5.9 and 5.10 with Li and Aspden (1997).

6.4.2 E_{d}(BV/TV) versus instantaneous loading creep test

Even though the strain rates reported in the literature are significantly lower than those employed in this study, the comparison with previous studies includes additional uncertainties, such as the method of obtaining the BV/TV of the samples, converting density to BV/TV and issues associated with different geometries. To remove some of these uncertainties, data from instanteneous loading creep tests conducted at Edinburgh (Xie, Wallace and Pankaj, 2018) were utilised. These tests had several similarities to the current study: they employed bovine bone which was similarly harvested and stored; they used similar sample shapes and sizes; and bone volume ratio was evaluated using micro-CT as in this study. Although these creep tests aimed to apply instantaneous loads, this was not possible and the real rate of loading had an apparent strain rate of 0.01 /sec (Xie et al., 2017).

The resulting moduli with their respective constructed BV/TV value are shown in Fig. 6.9, along with the regressed linear and power law expressions which are almost identical, with an identical coefficient of determination ($r^2 = 0.52$).

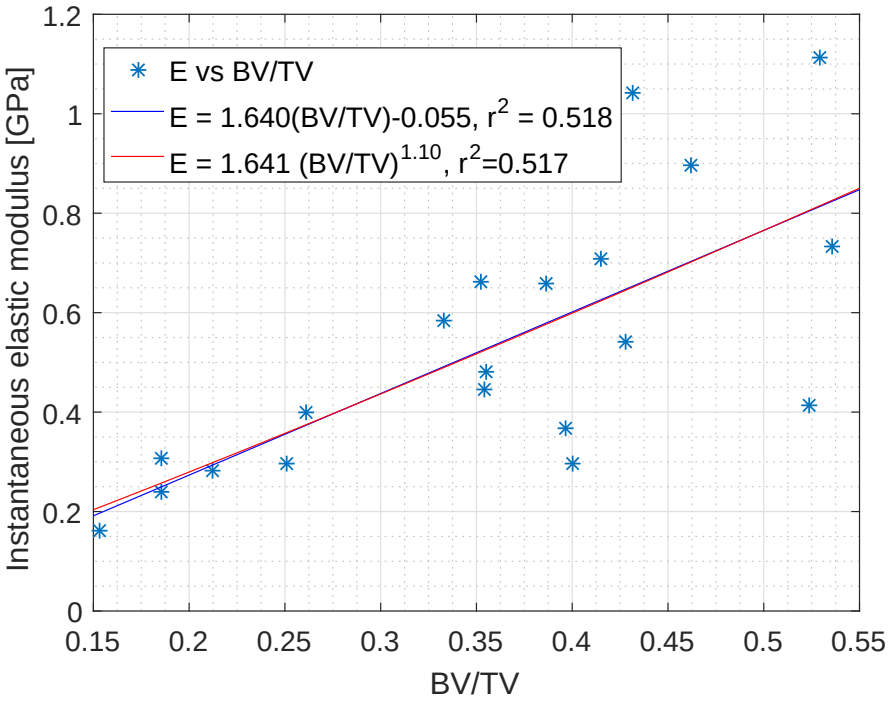

Figure 6.9: Linear and power law regressions on the instantaneous monotonic region of creep test under 0.01/sec strain rate. The original data is available in Xie, Wallace and Pankaj (2018)

In this quasi-static test on 20 trabecular bone samples, the elastic modulus for a strain rate of 0.01 /sec is expressed against BV/TV in the power law regression as

$$E = 1.641(\mathrm{BV/TV})^{1.10} \quad [\mathrm{GPa}]; \quad \mathrm{r}^2 = 0.517. \tag{6.3}$$

The BV/TV range for the samples used was 15-55% and the samples were extracted from the bovine trochanters and femoral heads. The elastic modulus obtained from this loading is compared to the derived E_d in Fig. 6.10.

The elastic modulus mathematical expression of 0.01 /sec strain rate is shown to be systematically lower than all four derived E_d equations ($\dot{\epsilon}_\mathrm{sct} \approx 30$ /sec). The

differences increase substantially for higher BV/TV. These plots show that E_{d} obtained from impact tests is higher than that obtained from loading rate test and that of previous studies. It can be concluded that the effect of strain rate on the resulting material response of trabecular bone, in which bone tested at higher strain behaves stiffer corresponds to higher elastic modulus values of the loaded samples.

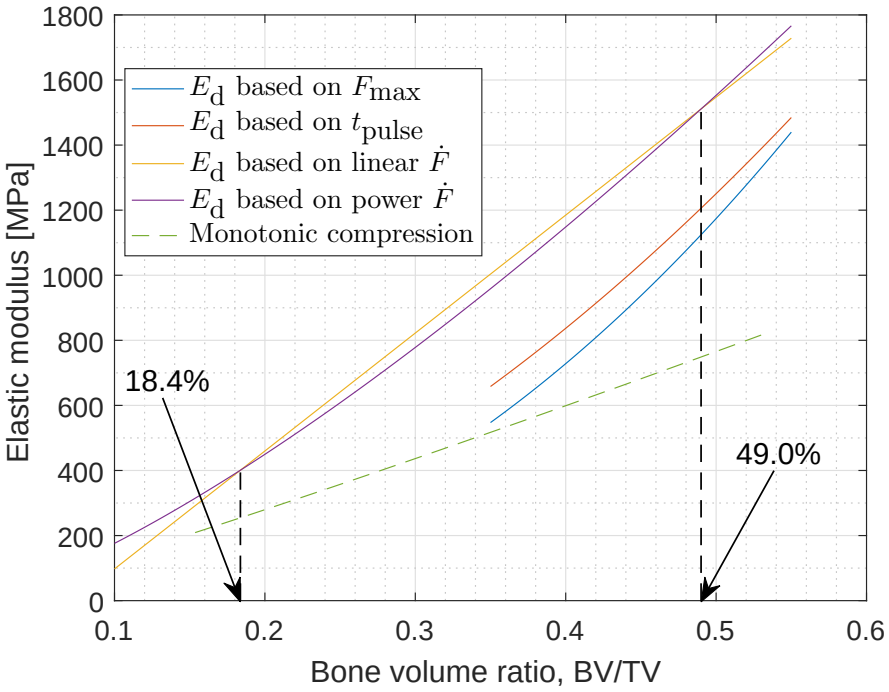

Figure 6.10: Comparison on the derived E_{d}(BV/TV) different expressions of varyingly-high strain rate (initial average of 44 /sec; secant of 30 /sec) with monotonic compression at apparent strain rate of 0.01 /sec

Chapter 7

Conclusions

7.1 Introduction

This Chapter summarises the methods employed in this study and the main findings. The achievement of original objective is commented and the recommendations for future work are outlined.

7.2 Development of analytical code

An analytical code was developed to derive an expression for the force at end struck for a prismatic elastic object restrained at one end and impacted at the other end.

- Equation expressing the force history at the end struck was derived for the pulse duration, t_{pulse}, during which the impactor remains in contact with the object using 'Symbolic math computation' in MATLAB.
- The number of intervals, N, for the stress wave to traverse the length of the sample and returns to the end struck in the pulse duration is inversely

proportional to the mass ratio, α. As N increases, so do the number of terms in the force history equation. The developed code can be readily expanded to include a wide range of mass ratios.

7.3 Parameter-output variable relations

The parameters in the expression of the force at end struck were examined to evaluate their effect on peak load, $F_{\max}$, pulse width, t_{pulse}, interval frequency, f and number of stress intervals, N. Generally, stiffer response of the pulse is shown by simultaneous higher peak load and shorter pulse width.

- Mass ratio, α is inversely proportional to the number of intervals, N, peak load, $F_{\max}$ and pulse width, t_{pulse}. It does not, however, affect the interval frequency, f.
- The square-root of drop height, h, which is related to the velocity of impactor, has direct proportionality with the peak load. Other output variables which are pulse width, number of intervals and interval frequency are independent of the drop height.
- The square-root of the bar's elastic modulus, E is directly proportional to the peak load, $F_{\max}$, and interval frequency, f; it is, on the other hand, inversely proportional to pulse width, t_{pulse}. The number of intervals, N, is not influenced by E. The loading rate, $\dot{F}$ increases with the modulus and can be used to derive the elastic modulus of the impacted bone from experimental results.

7.4 Numerical simulation of impact

The impact problem was simulated in FE using the commercial package of LS-DYNA. The elastic solution from the simulation was benchmarked against the

closed-form solution. The FE simulation has the advantage of simulating problems beyond the elastic case.

In the FE analysis, 2D solid model using axisymmetric elements was utilised. Both exclusion and inclusion of Poisson's ratio were considered; the former replicates the case for which closed-form solution was developed. The peak load and pulse width are not, however, significantly affected by the Poisson's ratio, while increase with the impactor's mass. The structural stiffness, k, which includes the elastic modulus and geometrical dimensions (area and length) has direct proportionality with the peak load, while the pulse width decreases with increasing k.

The application of fast Fourier transform (FFT) on the response obtained from FE results showed that the numerical solution from the explicit code in LS-DYNA returns an interval frequency with small deviation from the value that is expected theoretically. An FFT procedure on the response from the closed-form solution, on the other hand, results in an interval frequency that matches well with the theoretical value.

Time-dependent viscoelastic material behaviour was incorporated into the FE model and it shows stiffer response compared to the models with time-indepedent elastic modulus. The relations of peak load, pulse width and interval frequency with the square-root of E developed based on the time-independent FE models are comparable to their counterparts derived by the closed-form solution.

7.5 Response of impacted trabecular bone samples

Drop tests were performed on trabecular bone samples with known BV/TV and standardised geometry by a 2.5-kg impactor from a drop height of 50 mm. The force history was obtained at the end struck and the bottom using force sensors.

These two responses were found to have identical characteristics -only the first pulse was considered in the subsequent analysis.

Two main patterns of the impulsive response were obtained; those that were apparently elastic and those that were inelastic. As for the former, the response corresponds to the samples with high BV/TV value without growth plates. Samples with growth plates demonstrated an inelastic response indicating that the growth plates introduce a weak region.

Samples with low BV/TV had an elongated inelastic response. The prolonged time in the inelastic region was found to be inversely proportional to the BV/TV of the failed samples, which is comparable to the relation between pulse width and BV/TV of the apparently elastic samples. Meanwhile, shorter drop time was found for lower BV/TV samples, which exhibits "brittle" response compared to the diffused drop of moderately higher BV/TV samples.

7.6 Modelling impact responses

Inverse modelling was used to predict the elastic modulus of samples using FE analysis. This method is only applicable to the samples whose responses are apparently elastic (high BV/TV samples without growth plates). The moduli obtained were in the range of 650 to 1400 MPa for samples with BV/TV ranging between 35-53%. Higher BV/TV samples were found to generally correspond to higher elastic modulus.

Simulating the pattern of inelastic response was found to require elasto-plastic softening material model to capture the force history output pattern. The value of tangent modulus in softening was assigned arbitrarily to match the experimental post-elastic response, in which lower absolute value causes the response to have

closer resemblance to response from models with perfect-plasticity. Further investigation is required to simulate this post-peak impact behaviour.

7.7 Dynamic elastic moduli, E_{d}

Dynamic elastic moduli were derived using four approaches from three output variables: peak load, pulse width and loading rate in conjunction with the closed-form solution. Power law regression model was used to correlate the BV/TV of tested apparently elastic samples with the resulting outputs of peak load and pulse width. These expressions were then used to associate the predicted dynamic elastic modulus, E_{d} with the BV/TV of the samples by combining those equations with the corresponding relations obtained from the closed-form solution.

The initial rising region of the pulse was assumed to be elastic and analysed by fitting the loading rate, $\dot{F}$ with the BV/TV. By applying a similar procedure as for $F_{\max}$ and t_{pulse}, linear and power law relations were developed with the closed-form solution to obtain the empirical dynamic elastic moduli as functions of BV/TV.

7.8 Assessment of the obtained dynamic moduli

The expressions of dynamic elastic moduli were compared to a number of selected moduli from literature that have been reported for relatively low strain rate loadings (< 0.03 /sec). Strain rate imparted by impact was estimated using FE analysis. The average strain rate history was obtained from filtered minimum principal strain and displacement histories. The average strain rate was shown to have the highest value of 44.3 /sec at the initial stage for the experimental set-up considered in this study. The secant strain rate was obtained by considering the peak strain and the time taken to attain it; it was found to be around 30 /sec. These values are significantly higher than those of previous studies that reported

the elastic modulus of bone, thus the moduli expressions in this work can be labelled as 'dynamic'.

In comparison to the three elastic moduli from literature, the derived dynamic elastic moduli were found to be higher (up to three times in some cases). The previous studies in which the results were compared with had strain rates recorded at 0.0033, 0.01 and 0.03 /sec, which are lower than the current impact scenario.

In order to draw a closer comparison, the elastic modulus expression was derived for samples that had been subjected to compressive loading at 0.01 /sec apparent strain rate. These previous samples were very similar to those used in the present study and their BV/TV values had been obtained using identical techniques. From this comparison, the effect of higher strain rate on the elastic modulus was demonstrated, i.e. stiffer response was observed when the samples were tested at higher secant strain rate of 30 /sec in the current work under impact.

7.9 Comparison of research achievements with the "Original objective"

The current study has achieved the original objective (Section 1.3), -which was to relate the bone properties to measurements under impact -which was observed to be in the above mentioned range of strain rate. The study, however, does not evaluate the effect of varying range of this rate. The evaluated measurement in this study is bone volume fraction obtained from reconstruction of scanned images by micro-computed tomography.

7.10 Future work

- Post-elastic behaviour of failed samples requires further investigation using the current softening-plasticity model. At present, the tangent modulus is

arbitrarily assigned in an attempt to match the plastic response. Whilst this reproduces the post-elastic trend found in the experiment, it also includes high frequency noise.

- The analysed mechanical properties in this study only consider their relation with bone's BV/TV, whilst previous studies have shown that other indices of microstructure affect these properties. Further investigations may reveal the relationships between the properties and broad spectrum of microstructural indices.
- The current experimental set up can be extended to include additional layers of realistic materials, such as cortical bone, soft tissue and protective clothing to investigate their combined effect on the impact load. Improved understanding on this issue will assist in modelling full femur subjected to a sideways fall. The femur FE model can be defined as heterogeneous materials by using the E_{d}-BV/TV empirical relations developed from this study.

References

Ariza, O., Gilchrist, S., Widmer, R. P., Guy, P., Ferguson, S. J., Cripton, P. A. and Helgason, B. (2015), 'Comparison of explicit finite element and mechanical simulation of the proximal femur during dynamic drop-tower testing', *Journal of Biomechanics* **48**(2), 224–232.
URL: *http://www.ncbi.nlm.nih.gov/pubmed/25527888*

Bayraktar, H. H. and Keaveny, T. M. (2004), 'Mechanisms of uniformity of yield strains for trabecular bone', *Journal of Biomechanics* **37**(11), 1671–1678.

Bayraktar, H. H., Morgan, E. F., Niebur, G. L., Morris, G. E., Wong, E. K. and Keaveny, T. M. (2004), 'Comparison of the elastic and yield properties of human femoral trabecular and cortical bone tissue', *Journal of Biomechanics* **37**(1), 27–35.
URL: *http://www.ncbi.nlm.nih.gov/pubmed/14672565*

Bekker, A., Kok, S., Cloete, T. J. and Nurick, G. N. (2014), 'Introducing objective power law rate dependence into a visco-elastic material model of bovine cortical bone', *International Journal of Impact Engineering* **66**, 28–36.
URL: *http://dx.doi.org/10.1016/j.ijimpeng.2013.12.003*

Bessho, M., Ohnishi, I., Matsuyama, J., Matsumoto, T., Imai, K. and Nakamura, K. (2007), 'Prediction of strength and strain of the proximal femur by a CT-based finite element method', *Journal of Biomechanics* **40**(8), 1745–1753.

Bevill, G. and Keaveny, T. M. (2009), 'Trabecular bone strength predictions using finite element analysis of micro-scale images at limited spatial resolution', *Bone* **44**(4), 579–84.
URL: *http://www.ncbi.nlm.nih.gov/pubmed/19135184*

Bowman, S. M., Guo, X. E., Cheng, D. W., Keaveny, T. M., Gibson, L. J., Hayes, W. C. and McMahon, T. A. (1998), 'Creep contributes to the fatigue behavior of bovine trabecular bone', *Journal of Biomechanical Engineering* **120**(5), 647–654.

Carter, D. R. and Hayes, W. C. (1977), 'The compressive behavior of bone

as a two-phase porous structure', *The Journal of Bone and Joint Surgery* **59**(7), 954–962.

Charlebois, M. (2008), Constitutive Law for Trabecular Bone in Large Strain Compression, PhD thesis, Technische Universität Wien.

Chopra, A. K. (2001), *Dynamics of Structures: Theory and applications to earthquake engineering*, second edn, Prentice Hall, Upper Saddle River, New Jersey.

Ciarelli, T. E., Fyhrie, D. P., Schaffler, M. B. and Goldstein, S. A. (2000), 'Variations in three-dimensional cancellous bone architecture of the proximal femur in female hip fractures and in controls', *Journal of Bone and Mineral Research* **15**(1), 32–40.

Cody, D. D., Gross, G. J., Hou, F. J., Spencer, H. J., Goldstein, S. A. and Fyhrie, D. P. (1999), 'Femoral strength is better predicted by finite element models than QCT and DXA', *Journal of Biomechanics* **32**(10), 1013–1020.

Completo, A., Fonseca, F. and Simões, J. A. (2007), 'Experimental validation of intact and implanted distal femur finite element models', *Journal of Biomechanics* **40**(11), 2467–76.
URL: *http://www.ncbi.nlm.nih.gov/pubmed/17224158*

Conlisk, N., Gray, H., Pankaj, P. and Howie, C. R. (2012), 'The influence of stem length and fixation on initial femoral component stability in revision total knee replacement', *Bone & Joint Research* **1**(11), 281–288.

Cristofolini, L., Juszczyk, M., Martelli, S., Taddei, F. and Viceconti, M. (2007), 'In vitro replication of spontaneous fractures of the proximal human femur', *Journal of Biomechanics* **40**(13), 2837–2845.

Cristofolini, L., Viceconti, M., Cappello, A. and Toni, A. (1996), 'Mechanical validation of whole bone composite femur models', *Journal of Biomechanics* **29**(4), 525–535.

Dall'Ara, E., Eastell, R., Viceconti, M., Pahr, D. and Yang, L. (2016), 'Experimental validation of DXA-based finite element models for prediction of femoral strength', *Journal of the Mechanical Behavior of Biomedical Materials* **63**, 17–25.
URL: *http://dx.doi.org/10.1016/j.jmbbm.2016.06.004*

de Bakker, P. M., Manske, S. L., Ebacher, V., Oxland, T. R., Cripton, P. A. and Guy, P. (2009), 'During sideways falls proximal femur fractures initiate in the superolateral cortex: Evidence from high-speed video of simulated fractures', *Journal of Biomechanics* **42**(12), 1917–1925.
URL: *http://dx.doi.org/10.1016/j.jbiomech.2009.05.001*

Dean, L. (2010), 'Structure of long bone and bone growth'.
URL: *https://www.slideshare.net/deanlr55/structure-of-long-bone-and-bone-growth*

Deng, Z., Cheng, H., Wang, Z., Zhu, G. and Zhong, H. (2016), 'Compressive behavior of the cellular concrete utilizing millimeter-size spherical saturated SAP under high strain-rate loading', *Construction and Building Materials* **119**, 96–106.
URL: *http://dx.doi.org/10.1016/j.conbuildmat.2016.05.018*

Donaldson, F. E., Pankaj, P., Cooper, D. M. L., Thomas, C. D. L., Clement, J. G. and Simpson, A. H. R. W. (2011), 'Relating age and micro-architecture with apparent-level elastic constants: A micro-finite element study of female cortical bone from the anterior femoral midshaft', *Proceedings of the Institution of Mechanical Engineers, Part H: Journal of Engineering in Medicine* **225**(6), 585–596.

Donaldson, F. E., Pankaj, P. and Simpson, A. H. R. (2012*a*), 'Bone properties affect loosening of half-pin external fixators at the pin-bone interface', *Injury* **43**(10), 1764–1770.
URL: *http://dx.doi.org/10.1016/j.injury.2012.07.001*

Donaldson, F. E., Pankaj, P. and Simpson, A. H. R. W. (2012*b*), 'Investigation of factors affecting loosening of ilizarov ring-wire external fixator systems at the bone-wire interface', *Journal of Orthopaedic Research* **30**(5), 726–732.

Enns-Bray, W. S., Ferguson, S. J. and Helgason, B. (2018), 'Strain rate dependency of bovine trabecular bone under impact loading at sideways fall velocity', *Journal of Biomechanics* **75**, 46–52.
URL: *https://doi.org/10.1016/j.jbiomech.2018.04.042*

Falcinelli, C., Schileo, E., Balistreri, L., Baruffaldi, F., Bordini, B., Viceconti, M., Albisinni, U., Ceccarelli, F., Milandri, L., Toni, A. and Taddei, F. (2014), 'Multiple loading conditions analysis can improve the association between finite element bone strength estimates and proximal femur fractures: A preliminary study in elderly women', *Bone* **67**, 71–80.
URL: *http://dx.doi.org/10.1016/j.bone.2014.06.038*

Fliri, L., Sermon, A., Wähnert, D., Schmoelz, W., Blauth, M. and Windolf, M. (2013), 'Limited V-shaped cement augmentation of the proximal femur to prevent secondary hip fractures', *Journal of Biomaterials Applications* **28**(1), 136–143.

Gibson, L. J. (1985), 'The mechanical behaviour of cancellous bone', *Journal of Biomechanics* **18**(5), 317–328.

Gibson, L. J. and Ashby, M. F. (1997), *Cellular solids: Structure and properties*, second edn, Cambridge University Press, Cambridge.

Gilchrist, S., Guy, P. and Cripton, P. A. (2013), 'Development of an Inertia-Driven Model of Sideways Fall for Detailed Study of Femur Fracture Mechanics', *Journal of Biomechanical Engineering* **135**(12), 121001–1–8.

Gilchrist, S., Nishiyama, K. K., de Bakker, P., Guy, P., Boyd, S. K., Oxland, T. and Cripton, P. A. (2014), 'Proximal femur elastic behaviour is the same in impact and constant displacement rate fall simulation', *Journal of Biomechanics* **47**(15), 3744–3749.
URL: *http://dx.doi.org/10.1016/j.jbiomech.2014.06.040*

Goulet, R. W., Goldstein, S. A., Ciarelli, M. J., Kuhn, J. L., Brown, M. B. and Feldkamp, L. A. (1994), 'The relationship between the structural and orthogonal compressive properties of trabecular bone', *Journal of Biomechanics* **27**(4), 375–89.
URL: *http://www.ncbi.nlm.nih.gov/pubmed/8188719*

Grassi, L., Schileo, E., Taddei, F., Zani, L., Juszczyk, M., Cristofolini, L. and Viceconti, M. (2012), 'Accuracy of finite element predictions in sideways load configurations for the proximal human femur', *Journal of Biomechanics* **45**(2), 394–399.
URL: *http://linkinghub.elsevier.com/retrieve/pii/S0021929011006531*

Hansen, U., Zioupos, P., Simpson, R., Currey, J. D. and Hynd, D. (2008), 'The Effect of Strain Rate on the Mechanical Properties of Human Cortical Bone', *Journal of Biomechanical Engineering* **130**(1), 01101–1 – 011011–8.

Hayes, W. C., Myers, E. R., Morris, J. N., Gerhart, T. N., Yett, H. S. and Lipsitz, L. A. (1993), 'Impact near the hip dominates fracture risk in elderly nursing home residents who fall', *Calcified Tissue International* **52**(3), 192–198.

Heiner, A. D. (2008), 'Structural properties of fourth-generation composite femurs and tibias', *Journal of Biomechanics* **41**(15), 3282–3284.
URL: *http://linkinghub.elsevier.com/retrieve/pii/S002192900800434X*

Heiner, A. D. and Brown, T. D. (2001), 'Structural properties of a new design of composite replicate femurs and tibias', *Journal of Biomechanics* **34**(6), 773–781.

Helgason, B., Perilli, E., Schileo, E., Taddei, F., Brynjólfsson, S. and Viceconti, M. (2008), 'Mathematical relationships between bone density and mechanical properties: A literature review', *Clinical Biomechanics* **23**(2), 135–146.

Heller, M. O., Bergmann, G., Deuretzbacher, G., Claes, L., Haas, N. P. and Duda, G. N. (2001), 'Influence of femoral anteversion on proximal femoral

loading: Measurement and simulation in four patients', *Clinical Biomechanics* **16**(8), 644–649.

Heller, M. O., Bergmann, G., Deuretzbacher, G., Dürselen, L., Pohl, M., Claes, L., Haas, N. P. and Duda, G. N. (2001), 'Musculo-skeletal loading conditions at the hip during walking and stair climbing', *Journal of Biomechanics* **34**(7), 883–893.

Hosseini, H. S., Horak, M., Zysset, P. K. and Jirasek, M. (2015), 'An over-nonlocal implicit gradient-enhanced damage-plastic model for trabecular bone under large compressive strains', *International Journal for Numerical Methods in Biomedical Engineering* **31**(11).

Hosseini, H. S., Pahr, D. H. and Zysset, P. K. (2012), 'Modeling and experimental validation of trabecular bone damage, softening and densification under large compressive strains', *Journal of the Mechanical Behavior of Biomedical Materials* **15**, 93–102.
URL: *http://dx.doi.org/10.1016/j.jmbbm.2012.06.005*

Huiskes, R., Chao, E. Y. and Crippen, T. E. (1985), 'Parametric analyses of pinbone stresses in external fracture fixation devices', *Journal of Orthopaedic Research* **3**(3), 341–349.

Jensen, O., Spaak, E. and Zumer, J. M. (2014), Human Brain Oscillations: From Physiological Mechanisms to Analysis and Cognition, *in* S. Supek and C. J. Aine, eds, 'Magnetoencephalography: From Signals to Dynamic Cortical Networks', number November, Springer-Verlag, Heilderberg, pp. 359–404.

Johanson, N. A., Charlson, M. E., Cutignola, L., Neves, M., DiCarlo, E. F. and Bullough, P. G. (1993), 'Femoral neck bone density. Direct measurement and histomorphometric validation', *The Journal of Arthroplasty* **8**(6), 641–652.

Kaneko, T. S., Bell, J. S., Pejcic, M. R., Tehranzadeh, J. and Keyak, J. H. (2004), 'Mechanical properties, density and quantitative CT scan data of trabecular bone with and without metastases', *Journal of Biomechanics* **37**(4), 523–530.

Kanis, J. A. and Pitt, F. A. (1992), 'Epidemiology of osteoporosis', *Bone* **13**, S7–S15.
URL: *http://dx.doi.org/10.1016/S8756-3282(09)80004-5*

Kannus, P., Leiponen, P., Parkkari, J., Palvanen, M. and Järvinen, M. (2006), 'A sideways fall and hip fracture', *Bone* **39**(2), 383–384.

Keaveny, T. M., Borchers, R. E., Gibson, L. J. and Hayes, W. C. (1993), 'TRABECULAR BONE MODULUS AND STRENGTH CAN DEPEND ON SPECIMEN GEOMETRY', *Journal of Biomechanics* **26**(8), 991–1000.

Keller, T. S. (1994), 'Predicting the compressive mechanical behavior of bone', *Journal of Biomechanics* **27**(9), 1159–1168.

Keyak, J. H. (2001), 'Improved prediction of proximal femoral fracture load using nonlinear finite element models', *Medical Engineering and Physics* **23**(3), 165–173.

Keyak, J. H., Lee, I. Y. and Skinner, H. B. (1994), 'Correlations between orthogonal mechanical properties and density of trabecular bone: Use of different densitometric measures', *Journal of Biomedical Materials Research* **28**(11), 1329–1336.

Keyak, J. H., Rossi, S. A., Jones, K. A. and Skinner, H. B. (1998), 'Prediction of femoral fracture load using automated finite element modelling', *Journal of Biomechanics* **31**(2), 125–133.
URL: *http://www.sciencedirect.com/science/article/pii/S0021929097001231*

Koivumäki, J. E. M., Thevenot, J., Pulkkinen, P., Kuhn, V., Link, T. M., Eckstein, F. and Jämsä, T. (2012), 'Cortical bone finite element models in the estimation of experimentally measured failure loads in the proximal femur', *Bone* **51**(4), 737–740.
URL: *http://dx.doi.org/10.1016/j.bone.2012.01.012*

Kopperdahl, D. L. and Keaveny, T. M. (1998), 'Yield strain behavior of trabecular bone', *Journal of Biomechanics* **31**(7), 601–608.

Laing, A. C. and Robinovitch, S. N. (2010), 'Characterizing the effective stiffness of the pelvis during sideways falls on the hip', *Journal of Biomechanics* **43**(10), 1898–1904.

Lakes, R. (2001), Viscoelastic Properties of Cortical Bone, *in* S. C. Cowin, ed., 'Bone Mechanics Handbook', second edn, CRC Press, Boca Raton, Florida, chapter 11.

Lakes, R. S., Katz, J. L. and Sternstein, S. S. (1979), 'Viscoelastic properties of wet cortical bone-I. Torsional and biaxial studies', *Journal of Biomechanics* **12**(9), 657–678.

Levrero-Florencio, F., Manda, K., Margetts, L. and Pankaj, P. (2017*a*), 'Effect of including damage at the tissue level in the nonlinear homogenisation of trabecular bone', *Biomechanics and Modeling in Mechanobiology* **16**(5), 1681–1695.

Levrero-Florencio, F., Manda, K., Margetts, L. and Pankaj, P. (2017*b*), 'Nonlinear homogenisation of trabecular bone: Effect of solid phase constitutive model', *Proceedings of the Institution of Mechanical Engineers, Part H: Journal of Engineering in Medicine* **231**(5), 405–414.

Levrero-Florencio, F., Margetts, L., Sales, E., Xie, S., Manda, K. and Pankaj, P. (2016), 'Evaluating the macroscopic yield behaviour of trabecular bone using a nonlinear homogenisation approach', *Journal of the Mechanical Behavior of Biomedical Materials* **61**, 384–396.
URL: *http://dx.doi.org/10.1016/j.jmbbm.2016.04.008*

Levrero-Florencio, F. and Pankaj, P. (2018), 'Using non-linear homogenization to improve the performance of macroscopic damage models of trabecular bone', *Frontiers in Physiology* **9**(MAY), 1–15.

Li, B. and Aspden, R. M. (1997), 'Composition and mechanical properties of cancellous bone from the femoral head of patients with osteoporosis or osteoarthritis', *Journal of Bone Mineral Research* **12**(4), 450–456.

Linde, F., Hvid, I. and Madsen, F. (1992), 'The effect of specimen geometry on the mechanical behaviour of trabecular bone specimens', *Journal of Biomechanics* **25**(4), 359–368.

Linde, F., Nørgaard, P., Hvid, I., Odgaard, A. and Søballe, K. (1991), 'Mechanical properties of trabecular bone. Dependency on strain rate', *Journal of Biomechanics* **24**(9), 803–809.

Livermore Software Technology Corporation (2017*a*), LS-DYNA® Keyword User's Manual Volume I, Technical report, Livermore Software Technology Corporation, Livermore, California.

Livermore Software Technology Corporation (2017*b*), LS-DYNA® Theory Manual, Technical report, Livermore Software Technology Corporation (LSTC), Livermore, California.

Lotz, J. C., Gerhart, T. N. and Hayes, W. C. (1990), 'Mechanical properties of trabecular bone from the proximal femur: A quantitative CT study', *Journal of Computer Assisted Tomography* **14**(1), 107–114.

MacLeod, A. R., Pankaj, P. and Simpson, A. H. R. (2012), 'Does screw-bone interface modelling matter in finite element analyses?', *Journal of Biomechanics* **45**(9), 1712–1716.
URL: *http://dx.doi.org/10.1016/j.jbiomech.2012.04.008*

Majumder, S., Roychowdhury, A. and Pal, S. (2008), 'Effects of trochanteric soft tissue thickness and hip impact velocity on hip fracture in sideways fall through 3D finite element simulations', *Journal of Biomechanics* **41**(13), 2834–2842.

Manda, K., Wallace, R. J., Xie, S., Levrero-Florencio, F. and Pankaj, P. (2017), 'Nonlinear viscoelastic characterization of bovine trabecular bone', *Biomechanics and Modeling in Mechanobiology* **16**(1), 173–189.

Manda, K., Xie, S., Wallace, R. J., Levrero-Florencio, F. and Pankaj, P. (2016), 'Linear viscoelasticity - bone volume fraction relationships of bovine trabecular bone', *Biomechanics and Modeling in Mechanobiology* **15**(6), 1631–1640.

Mayhew, P. M., Thomas, C. D., Clement, J. G., Loveridge, N., Beck, T. J., Bonfield, W., Burgoyne, C. J. and Reeve, J. (2005), 'Relation between age, femoral neck cortical stability, and hip fracture risk', *The Lancet* **366**(9480), 129–135.

Metz, R. (2007), 'Impact and drop testing with ICP® force sensors', *Sound and Vibration* **February**(Instrumentation Reference), 18–20.
URL: *http://www.sandv.com/downloads/0702metz.pdf*

Meyers, M. A. (1994), *Dynamic Behavior of Materials*, John Wiley & Sons, Inc., New York.

Morgan, E. F., Bayraktar, H. H. and Keaveny, T. M. (2003), 'Trabecular bone modulus-density relationships depend on anatomic site', *Journal of Biomechanics* **36**(7), 897–904.
URL: *http://www.ncbi.nlm.nih.gov/pubmed/12757797*

Morgan, E. F. and Keaveny, T. M. (2001), 'Dependence of yield strain of human trabecular bone on anatomic site', *Journal of Biomechanics* **34**, 569–577.

National Osteoporosis Society (2018), Strong, Steady and Straight: An expert consensus statement on physical activity and exercise for osteoporosis, Technical report, National Osteoporosis Society.

Nishiyama, K. K., Gilchrist, S., Guy, P., Cripton, P. and Boyd, S. K. (2013), 'Proximal femur bone strength estimated by a computationally fast finite element analysis in a sideways fall configuration', *Journal of Biomechanics* **46**(7), 1231–1236.
URL: *http://linkinghub.elsevier.com/retrieve/pii/S002192901300105X*

Ouyang, J., Yang, G. T., Wu, W. Z., Zhu, Q. A. and Zhong, S. Z. (1997), 'Biomechanical characteristics of human trabecular bone', *Clinical Biomechanics* **12**(7/8), 522–524.

Park, H. C. and Lakes, R. S. (1986), 'Cosserat micromechanics of human bone: Strain redistribution by a hydration sensitive constituent', *Journal of Biomechanics* **19**(5), 385–397.

Park, S. W. and Schapery, R. A. (1999), 'Methods of interconversion between linear viscoelastic material functions. Part I–a numerical method based on Prony series', *International Journal of Solids and Structures* **36**(11), 1653–1675.
URL: *http://www.sciencedirect.com/science/article/pii/S0020768398000559*

Parkinson, I. H., Badiei, A., Stauber, M., Codrington, J., Müller, R. and Fazzalari, N. L. (2012), 'Vertebral body bone strength: The contribution of individual trabecular element morphology', *Osteoporosis International* **23**(7), 1957–1965.

PCB Piezotronics (n.d.*a*), Guide to Dynamic Force Sensors. White Paper, Technical report, PCB Piezotronics, New York.

PCB Piezotronics (n.d.*b*), Model 208C05 ICP® Force Sensor Installation and Operating Manual, Technical report, PCB Piezotronics, New York.

Qasim, M., Farinella, G., Zhang, J., Li, X., Yang, L., Eastell, R. and Viceconti, M. (2016), 'Patient-specific finite element estimated femur strength as a predictor of the risk of hip fracture: the effect of methodological determinants', *Osteoporosis International* **27**(9), 2815–2822.

Rydell, N. W. (1966), 'Forces Acting on the Femoral Head-Prosthesis: A Study on Strain Gauge Supplied Prostheses in Living Persons', *Acta Orthopaedica Scandinavica* **37**(sup88), 1–132.
URL: *https://doi.org/10.3109/ort.1966.37.suppl-88.01*

Sambrook, P. and Cooper, C. (2006), 'Osteoporosis', *The Lancet* **367**, 2010–18.

Schileo, E., Taddei, F., Cristofolini, L. and Viceconti, M. (2008), 'Subject-specific finite element models implementing a maximum principal strain criterion are able to estimate failure risk and fracture location on human femurs tested in vitro', *Journal of Biomechanics* **41**(2), 356–367.
URL: *http://linkinghub.elsevier.com/retrieve/pii/S0021929007003752*

Schileo, E., Taddei, F., Malandrino, A., Cristofolini, L. and Viceconti, M. (2007), 'Subject-specific finite element models can accurately predict strain levels in long bones', *Journal of Biomechanics* **40**(13), 2982–2989.
URL: *http://linkinghub.elsevier.com/retrieve/pii/S0021929007000711*

Schwiedrzik, J., Gross, T., Bina, M., Pretterklieber, M., Zysset, P. and Pahr, D. (2015), 'Experimental validation of a nonlinear μFE model based on cohesive-frictional plasticity for trabecular bone', *International Journal for Numerical Methods in Biomedical Engineering* **32**(4).
URL: *http://onlinelibrary.wiley.com/doi/10.1002/cnm.1494/full*

Shim, V., Yang, L., Liu, J. and Lee, V. (2005), 'Characterisation of the dynamic compressive mechanical properties of cancellous bone from the human cervical spine', *International Journal of Impact Engineering* **32**(1-4), 525–540.
URL: *http://linkinghub.elsevier.com/retrieve/pii/S0734743X05000606*

Solomon, L., Warwick, D. and Nayagam, S. (2010), *Apley's System of Orthopaedics and Fractures*, 9th edn, Hodder Arnold.

Taddei, F., Cristofolini, L., Martelli, S., Gill, H. and Viceconti, M. (2006), 'Subject-specific finite element models of long bones: An in vitro evaluation of the overall accuracy', *Journal of Biomechanics* **39**(13), 2457–2467.
URL: *http://linkinghub.elsevier.com/retrieve/pii/S0021929005003568*

Timoshenko, S. and Goodier, J. N. (1951), *Theory of Elasticity*, 2nd edn, McGraw-Hill Book Company, Inc., New York.

Trabelsi, N., Yosibash, Z., Wutte, C., Augat, P. and Eberle, S. (2011), 'Patient-specific finite element analysis of the human femurA double-blinded biomechanical validation', *Journal of Biomechanics* **44**(9), 1666–1672.
URL: *http://linkinghub.elsevier.com/retrieve/pii/S0021929011002776*

Turner, C. H. and Burr, D. B. (2001), Experimental Techniques for Bone Mechanics, *in* S. C. Cowin, ed., 'Bone Mechanics Handbook', second edn, CRC Press, Boca Raton, Florida, chapter 7.

Turner, C. H., Rho, J., Takano, Y., Tsui, T. Y. and Pharr, G. M. (1999), 'The elastic properties of trabecular and cortical bone tissues are similar: Results from two microscopic measurement techniques', *Journal of Biomechanics* **32**(4), 437–441.

Ulrich, D., van Rietbergen, B., Weinans, H. and Rüegsegger, P. (1998), 'Finite element analysis of trabecular bone structure: a comparison of image-based meshing techniques', *Journal of Biomechanics* **31**(12), 1187–1192.

van den Munckhof, S. and Zadpoor, A. A. (2014), 'How accurately can we predict the fracture load of the proximal femur using finite element models?', *Clinical Biomechanics* **29**(4), 373–380.
URL: *http://dx.doi.org/10.1016/j.clinbiomech.2013.12.018*

van Rietbergen, B., Weinans, H., Huiskes, R. and Odgaard, A. (1995), 'A new method to determine trabecular bone elastic properties and loading using micromechanical finite-element models', *Journal of Biomechanics* **28**(1), 69–81.
URL: *http://www.scopus.com/inward/record.url?eid=2-s2.0-0028936206&partnerID=tZOtx3y1*

Wang, S., Zhang, M.-H. and Quek, S. T. (2012), 'Mechanical behavior of fiber-reinforced high-strength concrete subjected to high strain-rate compressive loading', *Construction and Building Materials* **31**, 1–11.
URL: *http://dx.doi.org/10.1016/j.conbuildmat.2011.12.083*

World Health Organization (2003), Prevention and management of osteoporosis, Technical report, World Health Organization, Geneva.

Xie, S. (2018), Characterisation of time-dependent mechanical behaviour of trabecular bone and its constituents, PhD thesis, The University of Edinburgh.

Xie, S., Manda, K., Wallace, R. J., Levrero-Florencio, F., Simpson, A. H. R. and Pankaj, P. (2017), 'Time Dependent Behaviour of Trabecular Bone at Multiple Load Levels', *Annals of Biomedical Engineering* **45**(5), 1219–1226.

Xie, S., Wallace, R. J., Callanan, A. and Pankaj, P. (2018), 'From Tension to Compression: Asymmetric Mechanical Behaviour of Trabecular Bone's Organic Phase', *Annals of Biomedical Engineering* **46**(6), 801–809.

Xie, S., Wallace, R. and Pankaj, P. (2018), 'Characterisation of time-dependent mechanical behaviour of trabecular bone samples, [dataset]', *The University of Edinburgh. School of Engineering. Institute for Bioengineering* .
URL: *https://doi.org/10.7488/ds/2340*

Zani, L., Erani, P., Grassi, L., Taddei, F. and Cristofolini, L. (2015), 'Strain distribution in the proximal Human femur during in vitro simulated sideways fall', *Journal of Biomechanics* **48**(10), 2130–2143.
URL: *http://dx.doi.org/10.1016/j.jbiomech.2015.02.022*

Zysset, P. K., Goulet, R. W. and Hollister, S. J. (1998), 'A Global Relationship Between Trabecular Bone Morphology and Homogenized Elastic Properties', *Journal of Biomechanical Engineering* **120**(5), 640–646.